Analysis and Synthesis of Slow Wave Structures for Millimetre wave TWTs

Robert Michael Alan Waring
BSc

A Thesis Submitted for the degree of Doctor of Philosophy

June 2020

Engineering Department Lancaster University, UK

Abstract

Traveling wave tubes (TWTs) and backward wave oscillators (BWOs) are the only solution for high power amplification and RF generation at millimetre waves and THz frequencies. With advances in microfabrication technology, it is now possible to realise these devices with dimensions to support those frequency regimes. Promising applications of millimetre wave TWTs are as high-power amplifiers for wireless communications systems, imaging and satellite communications. BWOs would enable new plasma diagnostic in nuclear fusion capabilities and high-resolution imaging. TWTs are usually constructed using a helical waveguide as slow wave structure (SWS) by which wave energy can propagate. However, fabrication of a helix small enough to support mm-wave is not feasible. Novel SWSs are required suitable to be fabricated with the available processes.

The challenge of the simulation of TWTs or BWOs utilising a new SWS is the lack of fast code and the need to rely on powerful, yet slow, 3D electromagnetic software, which are computationally intensive. Both helices and the coupled cavity TWT can be simulated by fast simulation codes using Lagrangian methods. One of the aims of this thesis is to create a fast code for simulating arbitrary three-dimensional SWS, in particular the double corrugated waveguide. The code was validated by comparison with data of a Ka-band TWT available in literature.

The second aim is the design of circuits based on double corrugated waveguide SWSs for TWTs and BWO at different frequency to enable different

applications. New topologies of couplers were investigated. Extensive 3-dimensional simulations were performed to define dimensions and performance at different frequency bands.

Table of Contents

I. List of Figures

II. List of Tables

III. List of Symbols

u_B	Beam velocity [m/s]
η	Charge/Mass of electron ($1.76x10^{11}$ Ckg^{-1})
v_p	Phase velocity [m/s]
ω	Angular frequency [Radians/s]
k_z	z-component of wave number [1/m]
f	Frequency [1/s]
L_z	Period of helix [m]
r_h	Radius of hlix [m]
β_{nm}	Propagation constant of mode TE_{mn} in square waveguide [1/m]
k_{mn}	Wavenumber of mode TE_{mn} of square waveguide [1/m]
k_{mn_c}	Wavenumber corresponding to cut-off frequency of mode TE_{mn} of square waveguide [1/m]
m, n	Mode numbers
a, b	Dimensions of square waveguide [m]
ϕ	Phase difference in spatial harmonic [Radians]
Z	Interaction impedance [Ohms]
$\vec{E}$	Electric field strength [V/m]
P_a	Average power flow through period of waveguide [Watts]
B_b	Brillouin field [Tesla]
I_b	Beam current [Ampere]
ϵ_0	Permittivity of free space [F/m]
b	Beam radius [m]
V	Beam voltage [Volts]

h	Height of pillars in DCW [m]
w	Width of pillars in DCW [m]
t_p	Distance between pillars in DCW [m]
δ	Difference in pillar height and beam axis height [m]
P	Period [m]
dz	Integration step [m]
L_t	Length of structure [m]
N	Number of integration steps
ν_0	Characteristic phase velocity [m/s]
C	Pierce gain parameter
d_l	Loss factor
ρ	Charge density [C/m]
θ_y	Phase difference between wave and hypothetical wave travelling at initial electron beam velocity
y	Normalised distance along tube
Φ	Phase of charge group relative to wave
Φ_0	Initial phase of charge group relative to wave
$\vec{v}$	Electron velocity vector [m/s]
$\vec{B}$	Magnetic Flux density [Webers/m]
t	Time [s]
A(y)	Normalised amplitude of wave
u_t	Transverse velocity [m/s]
u	Normalised Velocity
ω_p	Plasma frequency [Radians/s]
σ	Space charge charge density [C/m]

e	Electron charge (-1.6×10^{-19} C)
E_z	z-component of electric field
δz	Small perturbation [m]
m	Electron rest mass (9.11×10^{-31}kg)
Φ_E	Scalar potential of electric field [V]
$\vec{A}$	Magnetic vector potential [Tm]
$\vec{H}$	Magnetic Field Strength [A/m]
I_D	DC Current [A]
τ	Beam propagation constant [Radian/m]
c	Speed of Light (2.998×10^8 m/s)
θ_{DCW}	Angle about the beam axis in DCW
α_θ	Angle vertical from the beam axis to the corner of the DCW
β_θ	Angle from corner of the DCW to the top corner of the pillar in the DCW
γ_θ	Angle from corner of pillar to horizontal through beam axis
ϵ_θ	Angle from horizontal to base of pillar
ζ_θ	Angle from base of pillar to negative vertical
$r_1, r_2, .., r_i$	Radii of concentric rings of subdivide charge group
N_c	Number of sectors in subdivision
N_R	Number of concentric rings subdivision
θ_s	Angle of sectors
F_z	Axial filling factor
λ'	Wavelength in waveguide
Φ_P	Periodic phase
N_j	Total number of charge groups with same initial phase

γ_r	Relativistic Lorentz Factor
P_w	Power of the wave [Watts]

IV. List of Acronyms

SWS	Slow wave structure
TWT	Traveling wave tube
BWO	Backward wave oscillator
mm-wave	Millimetre wavelength
THz	Terahertz
TWTA	Traveling wave tube amplifier
CW	Continuous wave
LO	Local oscillator
DCW	Double corrugated waveguide
PPM	Periodic permanent magnet
PIC	Particle in cell
CNC	Computer numerical control
LIGA	Lithographie, Galvanoformung, Abformung (Lithography, Electroplating, and Molding)
FWG	Folded waveguide

Chapter 1 Introduction and Background

This thesis comprises two parts. One on the realization of fast simulation tools for arbitrary slow wave structures (SWSs) for travelling wave tubes (TWTs) and backward wave oscillators (BWOs). Provided will be a background regarding helical TWTs and their common uses. The requirements of TWTs in the millimetre wave (mm-wave) and terahertz (THz) frequency regime, as well as already existing simulation methodologies will be discussed.

The second part is on the simulation of different double corrugated waveg`uide slow wave structures for different frequency band both for TWTs and BWOs up to 0.346 THz.

High efficiency, wide bandwidth, low cost TWT Amplifiers (TWTAs) for mm-wave and THz frequency range will be an integral part of many applications, including medical imaging, wireless communications, security and defence [1] [2].

TWTs are vacuum electronic device used for amplifying electromagnetic signals. Traditionally used at microwave frequency, the first TWTs used a conducting wire wound into a helical shape as the SWS by which an RF signal would propagate [3]. A source of DC energy in the form of an electron beam is provided by an electron gun. The signal interacts with the DC beam, and through the process of velocity and current modulation, the electrons would transfer energy to the AC RF signal. The spent DC electron beam is then picked up by a collector. The waves which interact with the DC beam are called ‘slow’ because the structure reduces the phase velocity of the wave.

1.1 Applications

TWTs have applications in many technological areas where high power over a wide frequency band is required. Similarly, backward wave oscillators are promising sources for THz and sub-THz radiation, albeit intrinsically narrowband at single beam voltage.

1.1.1 High data rate communications

With the world's data transfer growing, with a predicted sevenfold increase in monthly data usage resulting in a total of 49 exabytes by 2021 [4], systems able to cope with this demand must be designed. An important challenge to overcome for wireless communications is the limited bandwidth at microwave frequencies. Higher frequencies in the mm-wave regime can open the door to wider bandwidths available for data transfer, increasing the data rate [5] [6]. Due to the high attenuation of the atmosphere at mm-waves, especially in high humidity and rainy conditions, high transmission power of 10s of Watts [7] is required for long distance communication. Solid-state technology cannot provide this level of power. The link budget requires tens of Watt of power. TWTs at mm-wave are a solution to the increased need for large data transfers and demand for super-fast internet. At millimetre waves, architectures are being designed to distribute internet by Point to multipoint systems, at the mm-wave frequency bands of 90 GHz and 140 GHz. Although it has been shown that data-rates up 40 Gbps can be achieved with point to point above 100GHz, the range of such transfer is limited.

TWTs are so far the only devices capable of permitting tens of Watts power for wireless communication at the millimetre wave to exploit frequency bands

above 90 GHz [8]. Affordable TWTs for this purpose are currently in development, namely in the H2020 TWEETHER [9] project, and more recently, in the H2020 ULTRAWAVE project [10] [11].

1.1.2 Space millimetre wave TWTs

TWTs continue to be the main high-power amplifier for general communications spacecraft applications [12]. Terrestrial networks cannot cover all the areas for future wireless communications with data growth this extreme. As such, new architectures and solutions are necessary. High-data-rate satellite communications are considered complementary in solving this issue, along with terrestrial networks. Satellites are a convenient solution for the coverage for communities and projects in remote areas, where it may not be feasible to connect to an optical fibre backbone. Areas include remote deserts, and the sea, as well as areas struck by natural disaster such as tsunamis and earthquakes. Thus, Ku-band (12-18 GHz) and Ka-band (26.5-40 GHz) satellite solution can provide data rate of up to 150 Gbps. W- band (71-76 GHz) has been allocated for multi-Gbit satellite downlink [13] [14] [15], and is a further area where at present the TWT is the only viable option.

1.1.3 THz Imaging

THz imaging is important for non-destructive analysis of certain properties of materials, components or systems. Many materials are transparent to THz radiation whilst being opaque to other RF frequencies [16] [17]. THz imaging can effectively evaluate dielectric materials in fields such as pharmaceuticals, biomedicine, security and aerospace industries, as well as use in materials

characterisation [18]. THz can be emitted for either continuous wave (CW) or pulsed source imaging. Due to the relatively low wavelength of THz signals, THz imaging offers higher resolution imaging when compared to microwave signals. THz radiation is non-ionising and does not carry a threat towards living organic tissue.

BWOs are a good candidate as CW sources in the THz regime [19]. For example, in plasma diagnostics for fusion reactors, a BWO with operating frequency 0.346 THz is designed as local oscillator (LO) for a matrix of receivers to investigate the behaviour of the plasma utilising Thomson scattering [20].

1.2 Beam-wave Theory

The principal mechanism by which a TWT and BWO function is through beam-wave interaction. SWSs make this possible by synchronising the phase velocity of the relevant harmonic of the RF signal with that of electrons in an electron beam of given accelerating voltage, whilst also confining the wave in such a way for strong coupling to exist between the wave and electrons to maximise power transfer. The electrons are confined using specific magnetic field configurations. The synchronising of the wave with the electron beam is controlled by taking advantage of waveguide dispersion characteristics. The relevant harmonic can also be chosen through waveguide characteristic, and the coupling of the wave to the electron beam is characterised using interaction impedance.

1.2.1 Dispersion Characteristics

Dispersion is where the phase velocity of a wave is dependent on its frequency. In a waveguide, this can be achieved by periodic geometry. By carefully designing the period of the geometry, it is possible to lower the phase velocity of the wave, and make this phase velocity constant over a band of frequencies. This means the structure would have low dispersion.

Figure 1 illustrates constant phase velocity over a band of frequencies. The phase velocity is given by

$$v_p = \frac{\omega(f)}{k_z(f)} = \text{const.} \tag{1}$$

where ω is the angular frequency of the signal, and k_z is the wavenumber. There is a region in the middle of Figure 1 where the phase velocity remains constant for varying frequency. In this region, the wave can be in synchronism with a given speed of electrons, and the speed of the electrons is a function of

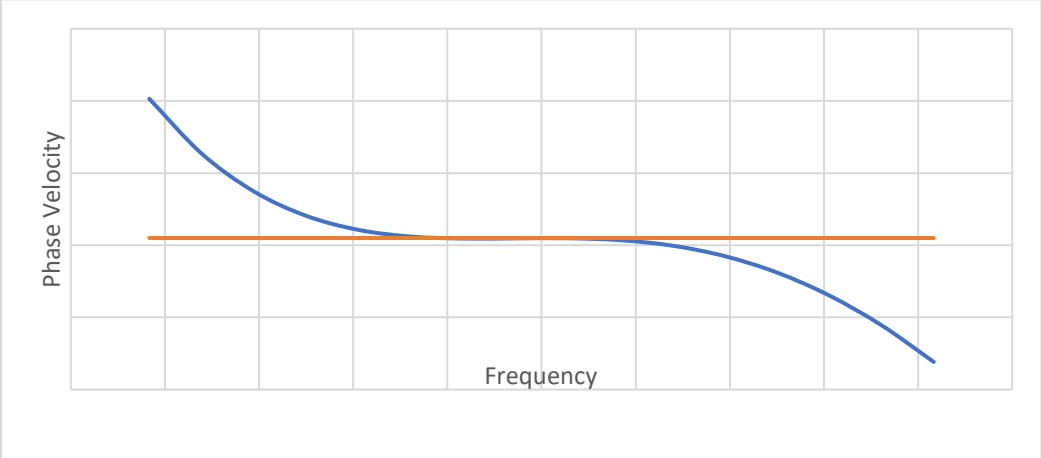

Figure *1* Example of a given SWS with a range of frequencies with constant Phase Velocity as a function of Frequency (blue) and a beam line (orange) of constant electron velocity

accelerating voltage. This can only occur for wide bandwidth if the SWS has low dispersion.

1.2.2 Dispersion of a Helical Waveguide and Rectangular Waveguide

Consider a helical waveguide, where the wire making up the coil is one-dimensional. The phase velocity is

$$\nu_{ph} = c\sin(\Psi) \tag{2}$$

where

$$\Psi = \tan^{-1}\frac{L}{2\pi r} \tag{3}$$

L is the period of the helix and r is the radius of the helix, c is the speed of light. This is simplified version of the helical waveguide has very low dispersion, meaning it supports many different frequencies with the same phase velocity.

For a rectangular waveguide, the phase velocity is

$$\nu_{p_{mn}} = \frac{\omega}{\beta_{mn}} \tag{4}$$

Where

$$\beta_{mn} = \sqrt{(k_{mn} - k_{c_{mn}})} \tag{5}$$

$k_{c_{mn}}$ is the wave number corresponding to the critical cut-off frequency of the waveguide, and k_{mn} is the free space wave number. β_{mn} is the propagation constant for the mode. The critical cut-off frequency is the lowest frequency at which an RF wave will not propagate through a waveguide. Shown in Figure 2 is a waveguide with width a and height b. In the case of this waveguide, the cut-off frequency is defined as [21], [22]

$$k_{c_{mn}} = \sqrt{\left(\frac{m\pi}{a}\right)^2 + \left(\frac{n\pi}{b}\right)^2} \tag{6}$$

In the limit of a and b tending towards infinity, $k_{c_{nm}}$ tends towards zero and the free space case dominates.

These two examples show how the wave phase velocity of a wave propagating

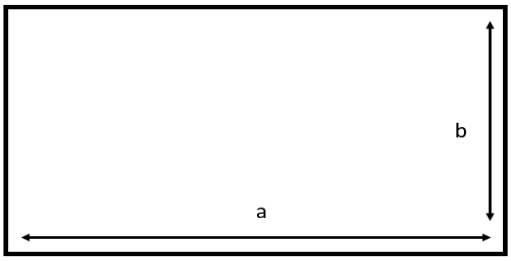

Figure *2* Definitions of *a*, the width of a rectangular waveguide, and *b*, the height

through different structures varies.

1.2.3 Harmonics

The phase velocity, as stated, should be constant within the range of continuous operational frequencies. However, it is possible choose for which frequency or spatial harmonic the phase velocity is constant.

For a helix, the fundamental forward space harmonic is used with a phase difference $0 < \phi < \pi$ radians. However, as the frequency increases and different structures are used for the SWS, it is necessary to use the first forward wave harmonic instead of the fundamental, that is, the region with a phase difference $2\pi < \phi < 3\pi$ radians. This is because the synchronous beam voltage becomes too high for compact power supplies. Figure 3 shows an example of the space harmonics [23]. While frequency harmonics are different frequencies with the same phase difference, space harmonics refer to identical frequencies with differing phase shift. The intercepts are regions of synchronicity for the wave and the electron beam. The second frequency

harmonic is shown in the red. The beam line also intercepts this higher frequency harmonic, but as they have a lower coupling capability to the electron beam, they do not interfere with the interaction with the fundamental frequency harmonic. The fundamental mode couples much more strongly. However, in some cases, the higher frequency harmonics are utilised [24].

The x-axis of Figure 3 represents the phase difference of the signal. When the phase difference is $0 < \phi < \pi$, the signal is in the fundamental harmonic. This is where conventional TWTs operate. BWOs operate in the phase difference of

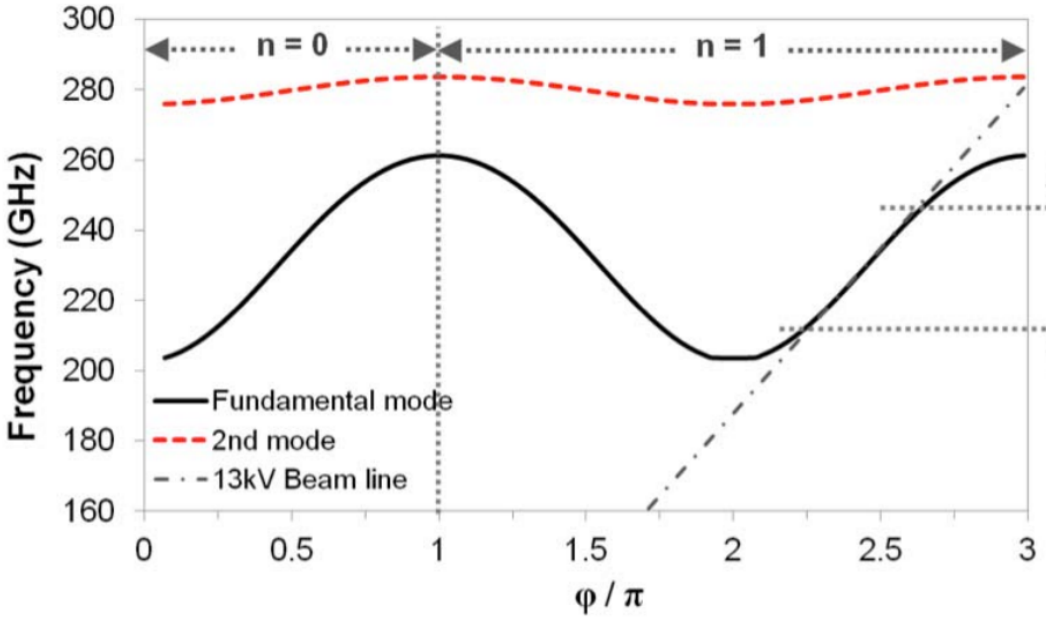

Figure *3* Example of spatial and frequency Harmonics over 3π of phase difference *[23]*

$\pi < \phi < 2\pi$. When the phase difference is $2\pi < \phi < 3\pi$, the space harmonic utilised is the 1st forward space harmonic. This is where structures such as the double corrugated waveguide (DCW) operate, due to the fundamental harmonic not being suitable, because the beam voltage required for operation would be much too high in the fundamental harmonic.

1.2.4 Interaction Impedance

Interaction impedance is the ability of the RF wave to extract energy from the electron beam. Its sole purpose is to provide a figure of merit as of the ability of the structure to confine the field in the close vicinity of the electron bunch. In the case of the helical waveguide, this can be achieved by having a low waveguide radius to beam radius ratio and is capable of provide tens of Ohms. It is defined mathematically as [25]

$$Z = \frac{\left|\vec{E}\right|^2}{2\beta^2 P_a} \tag{7}$$

where $\left|\vec{E}\right|$ is the amplitude of accelerating electric field at a given point in the SWS, and P_a is the average power flow through the period. β is the propagation constant of the electric field. The z-axis is defined as the axis along which the electron beam travels.

1.2.5 Beam-Wave Interaction: Forward Wave Amplifier Operation

Using the described physics of dispersion, harmonics, and interaction impedance, the interaction between the electron beam and wave can be described.

The coupling between the electrons and the appropriate harmonic of an RF wave causes a beam modulation effect. This means electrons in the beam 'bunch' together, resulting in regions of high current and low current. This is known as current modulation. A bunch is a region of high electron density, and an anti-bunch is a region of low electron density.

The RF wave propagates with a phase velocity ν_{ph}, and the electrons in the beam have velocity U_B, and is a function of the beam voltage, and is given by

$$U_B = \sqrt{(2\eta V)} \tag{8}$$

V is the beam voltage and η is the charge mass ratio of the electron.

If we take a section of the electron beam of equal length to the wavelength corresponding to the frequency we are interested in, with initial phase position, θ of $0 < \theta < 2\pi$ relative to the signal, and if

$$U_B = \nu_{ph} \tag{9}$$

then the electrons in the phase position $0 < \theta < \pi$ radians will be in the acceleration region of the RF wave, and will gain energy from the wave, and the electrons at $\pi < \theta < 2\pi$ radians will be in the deceleration region of the wave and lose energy to the wave. This will cause a bunching of electrons at the phase position π. The deceleration of electrons leads to an energy transfer from the electron beam to the RF field, while the acceleration of electrons leads to a transfer of the energy from the field to the electron beam. This results in a net gain of zero for the signal, in the case where losses are ignored, or a net

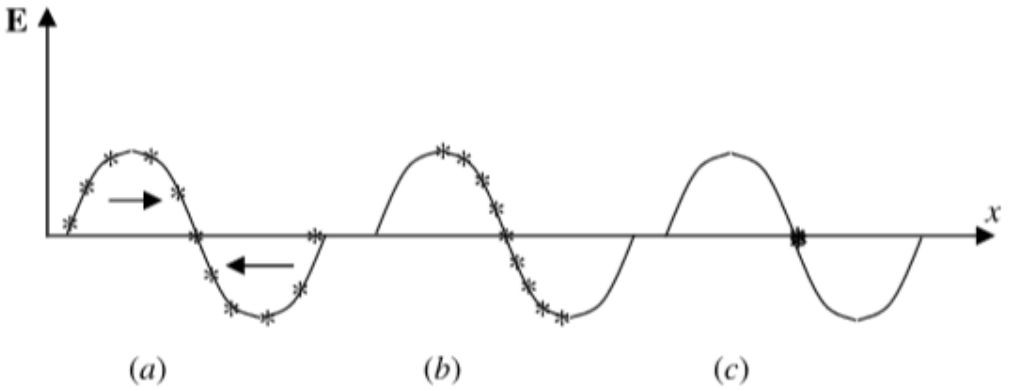

Figure *4* Electron bunching in the case of $U_B = \nu_{ph}$, where a), b) and c) are positions in time *[21]*

negative gain in the realistic case of non-zero losses. The bunching is shown in Figure 4 [21].

However, if the beam voltage is chosen to correspond to an electron velocity of slightly faster than the RF wave's phase velocity in the structure, where

$$U_B > v_p \tag{10}$$

Then bunching will occur in the deceleration region of the wave, leading to amplification of the wave. The faster electrons in acceleration region will move to the deceleration region, and the electrons in the deceleration region, will lose velocity and form a bunch of electrons in the deceleration region with the accelerated electrons. An anti-bunch occurs in the RF region of negative potential. The electrons in the deceleration region lose energy to RF wave due to being decelerated. This causes an amplification of the RF wave. The initial interaction between the wave and electron beam will result in a loss of RF energy, due to the electrons at the back of the beam leeching energy from the signal as they progress from the acceleration region to the deceleration region of the wave.

1.2.6 Beam-Wave Interaction: Backward Wave Oscillator Operation

BWOs, unlike TWTs, work by the interaction of an electron beam with the first negative space harmonic of a signal [21]. The phase velocity is in the opposite direction of the group velocity of the signal, which means energy travels in the opposite direction to the electron beam.

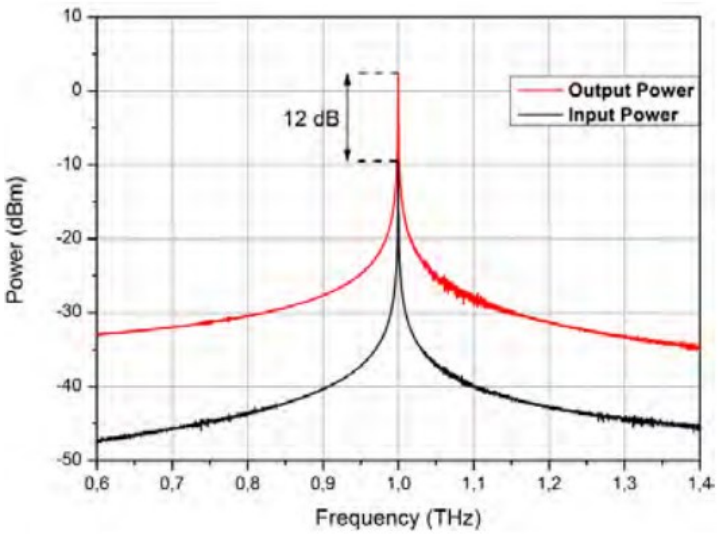

Figure *5* Output spectrum of a BWO *[26]*

If a circuit can support a negative spatial harmonic with a known phase velocity as a function of frequency, and an electron beam is injected with a beam velocity equal to that phase velocity, then a signal will be stimulated at that frequency with a group velocity in the direction opposite to that of the electron beam. This direction is towards the cathode. The electron beam is interacting with this negative harmonic and transferring energy to the signal. This energy is transported by the signal with its group velocity, in the opposite direction. Thus, the stimulated energy is carried to the cathode end of the tube. This induces velocity modulation in the electrons at the cathode end of the BWO, which in turn produces greater current modulation at the collector end of the BWO, stimulating more wave energy. This interaction in the BWO is inherently regenerative. For low beam currents, regenerative amplification is observed, and for higher beam currents, oscillation occurs. Figure 5 [26] shows the output spectrum of a typical BWO.

While single frequency, the circuit is tuneable to a degree defined by the dispersion characteristics of the structure, by varying the beam voltage. For

instance, in Figure 3 the backward harmonic is shown between π and 2π radians on the phase axis. Varying the beam voltage changes the slope of the beam line, and so changes the intersection point of the beam line and the dispersion curve, which changes the operational frequency of the circuit. BWOs can be excellent sources at millimetre wave and THz frequency, due to their simple operation [27]. BWOs also share the same setbacks as the TWTs as the size of the structure is inversely proportional to the desired operational frequencies, meaning at higher frequencies, fabrication becomes more difficult.

1.2.7 Magnetic Focussing Field

It is important to keep the electron beam in TWTs and BWOs with a given voltage and current confined. Brillouin flow is where the confining force of the magnetic field exactly opposes the repelling force of the space charge of the electrons. Correctly defining the confining field allows for accurate shaping of the electron beam. Equation (11) is the Brillouin flow equation [28].

$$B_b = \sqrt{\frac{\sqrt{2}I_b}{\epsilon_0 \pi b^2 \eta^{\frac{3}{2}} \sqrt{V}}} \tag{11}$$

B_b is the brillouin field, I_b is the beam current, ϵ_0 is the permittivity of free space, b_r is the beam radius, η is the mass-charge ratio of the electron and V is the beam voltage.

A higher beam current means the beam needs a stronger confining field to avoid collisions with the structure and to maintain the electron beams position in the field with highest interaction impedance. A common magnetic focussing system is built by periodic permanent magnets (PPM), due to the lightweight configuration which allows a quasi-constant magnetic field to confine the electron beam. PPM is shown in Figure 6.

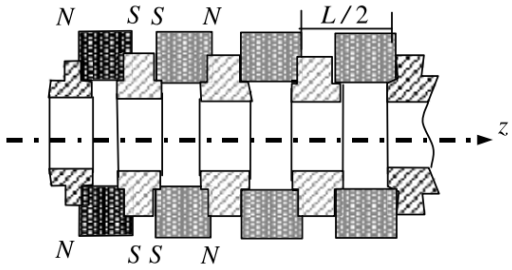

Figure *6* A typical axially symmetrical periodic permanent-magnet system (PPM) *[21]*

1.3 Construction of TWT and BWO

As shown in Figure 7, a helix TWT or BWO consists of some main components: the electron gun, the SWS, the magnetic field focussing system, the RF waveguide, and collector. Figure 8 show a more detailed schematic of the TWT [29, 21]. Electrons are emitted when a DC current heats the cathode. These

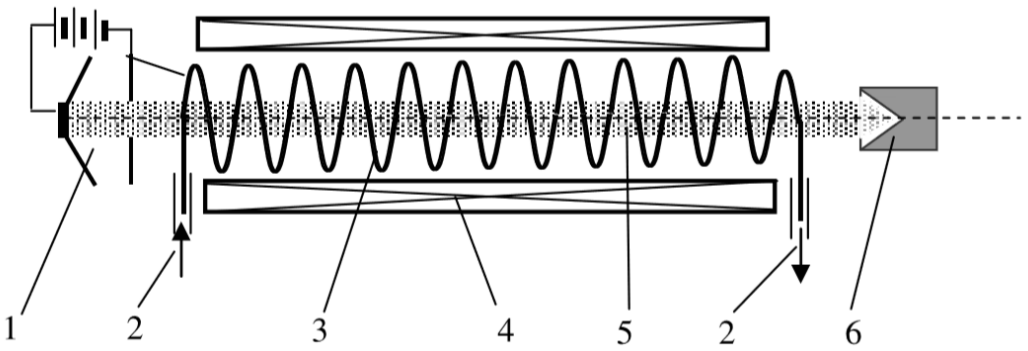

Figure *7* Traveling-wave tube. 1, Electron gun; 2, input–output; 3, helix slow-wave structure; 4, focusing magnet; 5, electron beam; 6, collector. *[21]*

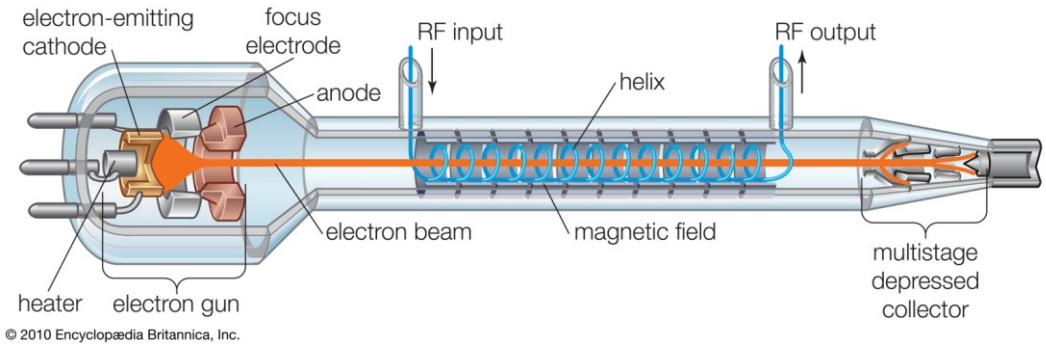

Figure *8* Detailed TWT Schematic, with the beam focussing illustrated. *[29]*

electrons are focussed into a shaped beam by electrodes and accelerated. This accelerated beam then enters the SWS, where DC energy from the beam amplifies the AC RF signal. The beam is kept focussed by magnets surrounding the SWS, which apply a magnetic field. These magnets are either a solenoid or PPM. The electron beam then enters a collector which collects the spent beam.

1.3.1 The Helix SWS

The helical SWS is wound helical metallic tape. The electron beam is provided by a thermionic electron gun. The length of the tube is carefully chosen so the beam wave interaction has maximum energy transfer from the beam to the signal. Too short and the tube will lack gain, too long and the beam will begin to leech energy from the wave. Relatively low velocity of the RF signal allows for a similarly low beam voltage for electron beam. This voltage is called the synchronous beam voltage. At the end of the SWS the electron beam is conveyed in a collector, which may reduce energy losses and increase efficiency [30]. At microwave frequency, helices are typically the SWS used in the amplification process of RF waves, because of their multi-octave bandwidth and high interaction properties. Advanced, three-dimensional electromagnetic simulation programs are used in the design process of such structures. Due to

the non-linearity of the interaction, particle-in-cell (PIC) simulations are required for predicting power output, gain, and saturation point of the structures for given input parameters. In PIC simulations, the field is discretised into a lattice of cells. Each cell has an associated electric and magnetic field which approximates to how the true field would behave. Particles in the simulation move based on how the field is distributed. The particles have now advanced in time, and so change the field. The field is now recalculated. This continues until the simulation is finished. The computational cycle is shown in Figure 9 [31].

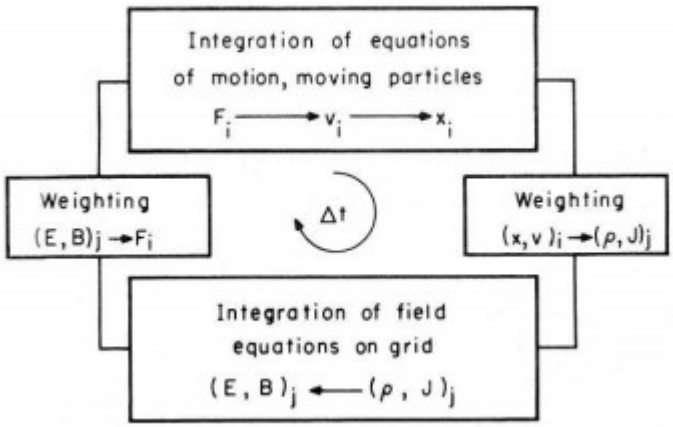

Figure *9* Computational cycle of a PIC simulation *[31]*

1.4 TWTs at the Millimetre Wavelength

TWTs are promising for amplification of mm-wave (30 - 300 GHz) frequency. Helices have multi-octave dispersion capabilities but are very difficult to manufacture when approaching mm-wave frequency regime. This is because as the operational frequency increases, the wavelength of the signal decreases. This means the SWS becomes proportionally smaller. The helix SWS at these frequencies would be at most 100-200 μm in diameter. The

fabricated helix SWS would be far too delicate for reliable performance at best, and impossible to fabricate at worst.

However, advances in microfabrication techniques such as high accuracy computer numerical controlled (CNC) milling [32] [33] and Lithographie, Galvanoformung, Abformung (LIGA) processes [34] [35] increased the potential of TWTs and BWOs to that of use in the millimetre wave and terahertz frequencies [36], through the use of structures beyond that of helical SWS. As such, novel and realisable structures can be designed and developed.

1.5 SWSs for Millimetre Wave TWTs

Novel SWSs must have suitable interaction impedance and low losses, over a wide bandwidth, and be manufacturable. The phase velocity must be reduced such that the synchronous beam voltage is low at around 10-30 kV for portability. In the following the most promising SWSs will be described.

1.5.1 Folded Waveguide Travelling Wave Tube

The folded waveguide (FWG) is a simple solution for a SWS of high power, high frequency and wide bandwidth TWTs. As shown in Figure 10, the geometry is obtained by the folding of a rectangular waveguide. The signal takes a longer path than the direct route taken by the electron beam. The electron beam voltage can be tuned such that the signal and the electron beam meet at the same time where the waveguide and the beam tunnel cross.

As the FWTWT is essentially a rectangular waveguide, the tapering of the structure only requires the widening or narrowing of the width and breadth of the waveguide. Because the TE_{10} mode of the signal in the input waveguide is

maintained in the SWS, the FWG exhibits very good S_{11} parameters [37] [38] [39] [40].

As an amplifier, the normal FWG TWT offers relatively wide bandwidth, but mediocre potential for gain due to low interaction impedance, which means the gain is low per period. The low gain per period is offset by making the full structure lengthy if high gain is a requirement. However, modifications to the basic FW design such as introducing grooves, allows for a significant increase in interaction impedance [41]. Due to its simple and robust design, it is a useful option for the mm-wave and THz regime.

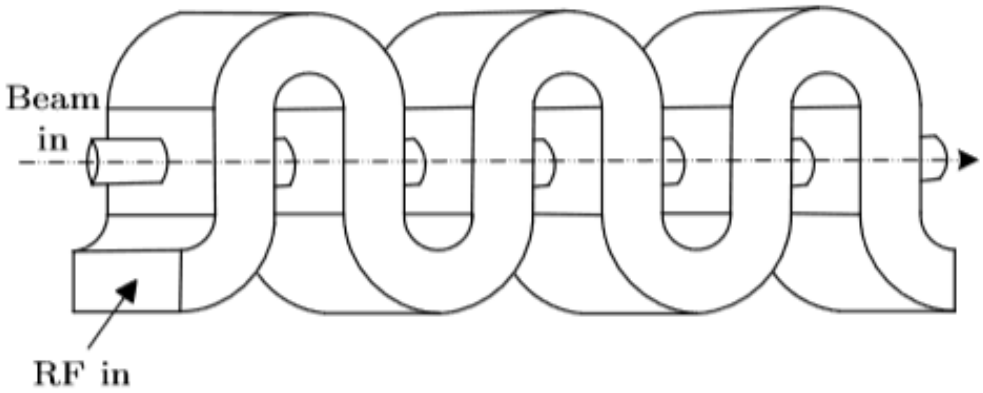

Figure *10* Three-dimensional diagram of a normal FW *[41]*

Figure 11 shows a cross section of the FW TWT. The simple structure of the FWTWT allows for manufacture even at higher frequencies, using high precision CNC milling techniques or LIGA [39]. A rendition of the FW TWT is shown in [42].

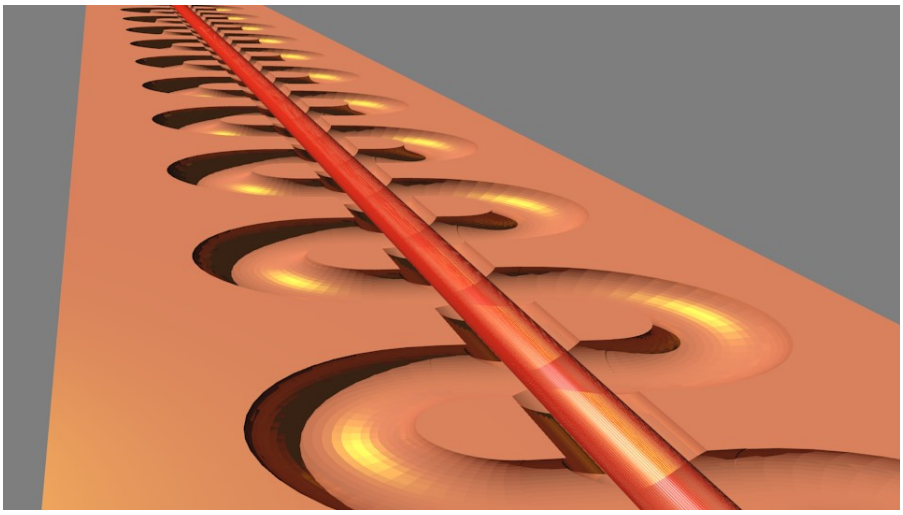

Figure *11* Rendition of the FW TWT, with electron beam *[42]*

1.5.2 Double Corrugated Waveguide

Double corrugated waveguide (DCW) is an effective solution for use in a TWT or BWO in the millimetre wave and THz regime. A rendition is shown in Figure 12 [26]. The DCW is comprised of two parts which may be aligned and then connected. This simplicity allows for easy assembly. One part is a hollow rectangular metal waveguide with two parallel rows of metal pillars.

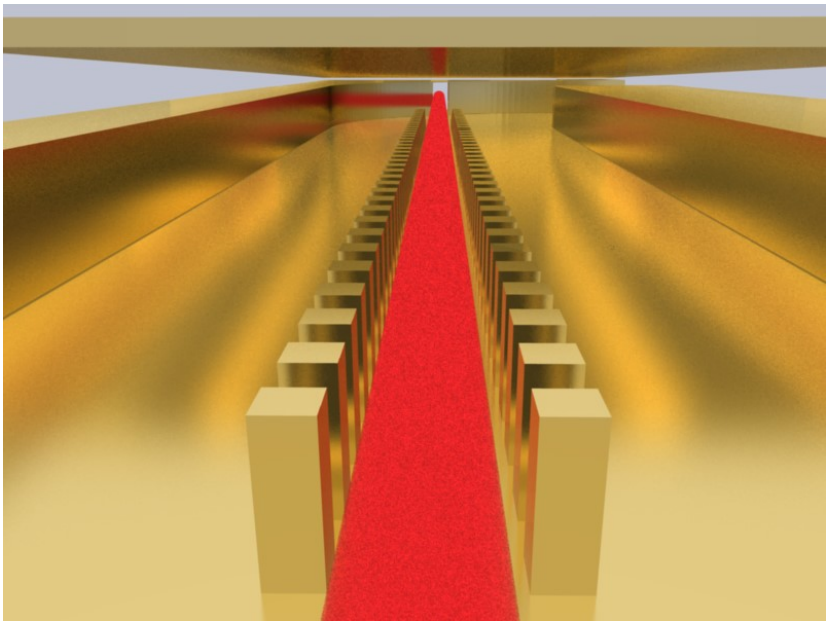

Figure *12* Rendition of the double corrugated waveguide with electron beam *[26]*

The second part is a metal plate which will close the waveguide. The pillars are separated width wise by a distance defined as the tunnel width. There are one pair of pillars per SWS period. The simple design allows for easy assembly. Fabrication can be realised by CNC milling or LIGA process.

As a SWS, the DCW supports a hybrid TE_{10} mode of operation, and as such a coupler section is required to transform the TE_{10} mode in to the hybrid mode where the signal enters the waveguide, and back again at the output, where the amplified signal leaves the device. The input and output waveguides are standard rectangular waveguide flanges [43]. Shown in Figure 13 is a method for coupling the SWS to the input and output waveguides. The width and height of the waveguide taper must be gradually increased or decreased to match that

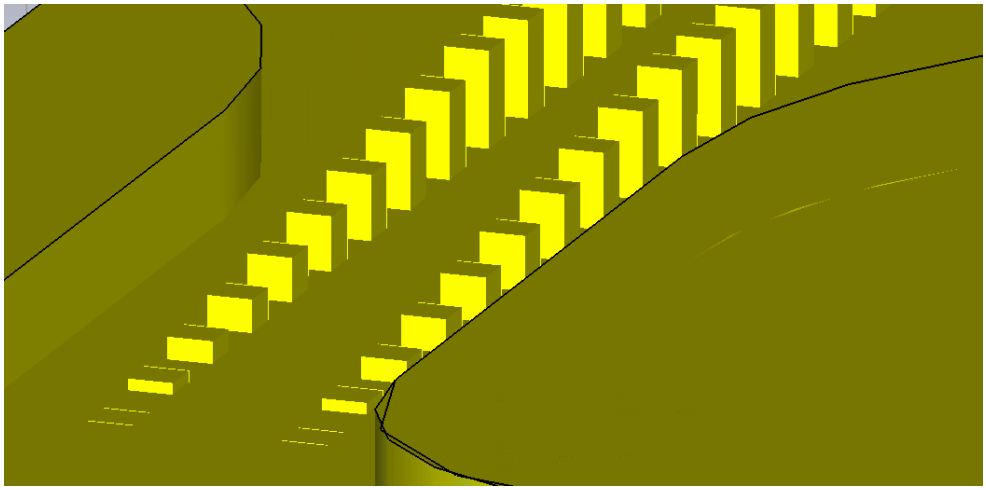

Figure *13* Introduction of pillars to the waveguide

of the SWS. Similarly, the pillars must be gradually built, to ensure the wave impedance is matched along the structure. The gradual introduction of pillars allows a reduction of reflections. The taper must be optimised so as little of the input signal is lost to reflections as possible. This is especially important in low power devices or devices whose input power is very low [44] [45] [46] [47] [23]. The DCW is suitable for wideband amplification in the millimetre wave and

terahertz regions. However, the beam line slope of the first forward spatial harmonic is the usable harmonic. This is because the synchronous beam voltage is too high when the fundamental harmonic is used. This limits the interaction impedance. Figure 14 shows the parameters considered in the

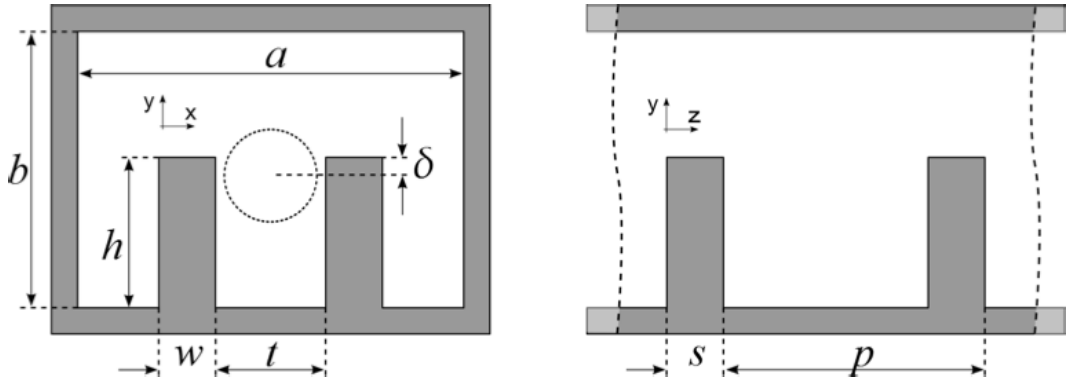

Figure *14* Design of the DCW *[23]* Left is the cross section perpendicular to the beam axis, and right is the cross section parallel to the beam axis and from the side of the DCW.

design of the geometry of the DCW.

1.6 Fabrication

SWSs are scalable into the mm-wave frequency regime. CNC machining technology allows for the micron scale tolerances and surface roughness required for the sub-THz regime [32] [33].

The LIGA process is based on the exposure of thick photoresist to a specific light source, and is used to build a relatively high aspect ratio 3D moulds, with arbitrary 2D patterns. The mould may then be used for electroplating microstructures such as mm-wave and THz regime SWS. In principle, the process allows for highly accurate structures and repeatability and can account for low tolerances of only a few microns [34].

1.7 Simulations

Full 3D particle-in-cell (PIC) electromagnetic simulators are used for the process of designing TWTs. This is to ensure the final device exhibits adequate power output and gain. Full PIC simulations can take a long time. However, in the case of tubes whose SWS is based upon the helix [48] [49] [50], the coupled cavity [51] [52] [53], the folded waveguide [54], and for devices whose SWS are modified versions of these [55], the mathematics for modelling the interaction and fast Lagrangian codes exist, which may be used to expedite the design process [56].

1.8 Lagrangian Formulation

Since the invention of the TWT, many methods have been derived to study the operation of the TWT in small signal regime. A basic postulate for the modelling of the TWT is defining the electron beam as a drifting charged fluid, with a single valued velocity and charge density functions at each displacement plane. This method is called Eularian formulation and is best suited to small signal analysis. Another possible formulation is the Lagrangian formulation. This is achieved by sub-dividing the electron beam into charge groups, or charge groups, and following these charge groups through the interaction. This formulation is well suited for non-linear interactions, such as the large signal analysis [50]. The Lagrangian formulation is shown illustratively in Figure 15, for the initial state of the electron beam with respect to the phase of the RF signal.

The Lagrangian formulation is utilised because nonlinear effects caused by the Lorentz force equation and the charge continuity equation become significant in the large signal case. The Lagrangian formulation uses well-defined charge

groups defined over a single RF wavelength of the signal supported by the SWS. This wavelength refers to the wavelength of the mode of the signal in the SWS. This method allows for the capture of the many of the nonlinear effects of the beam-wave interaction. Each of these charge group can move independently, and can slow down, reverse, and swap phase positions, which captures much of the non-linear behaviours of the system.

The transmission line model is a convenient way of modelling the beam wave interaction between the structure and electron beam, due to its inherent simplicity [50]. An example is shown in Figure 16 .

The beam wave interaction is a continuous process, and as such, the effect of the beam wave coupling must be evaluated at each integration step of the simulation. The integration step dz is defined as

$$\mathrm{dz} = \frac{\mathrm{L}}{\mathrm{N}} \tag{12}$$

Where L is the length of the structure and N is the number of integration steps.

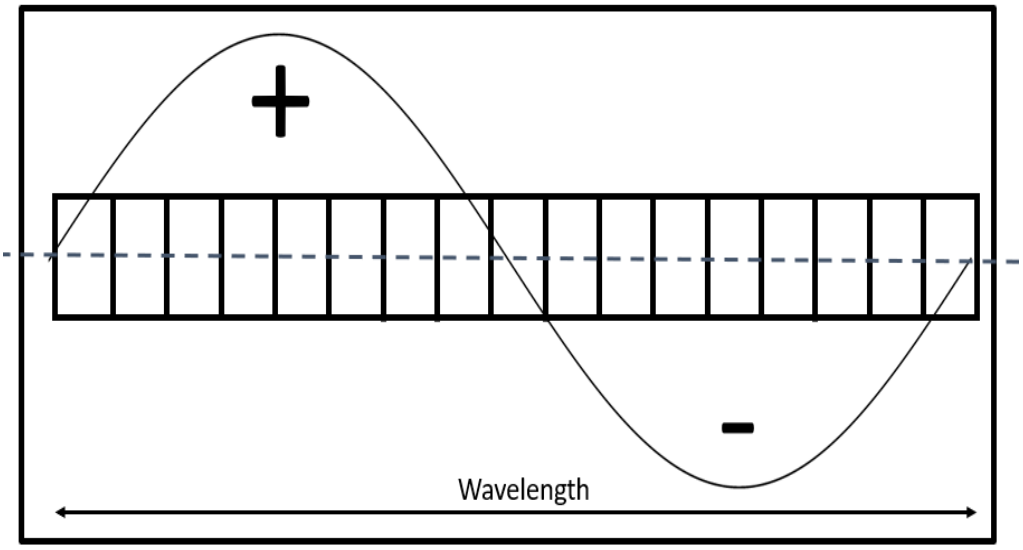

Figure *15* Lagrangian formulation of beam wave interaction. It depicts one wavelength of wave, and a section of electron beam the same length. The section of electron beam is divided in charge groups called charge groups. The + and – indicate the potential of the wave.

Initial velocity and phase positions are assigned to each charge group and each group has a fixed radius and a fixed charge and mass defined by the current density of the electron beam and the radius and number of charge groups [50]. Each charge group is free to move independently of the other charge groups, with exception to influence of space charge waves. In this case, the charge groups may slow down, pass through each other and reverse, and will feel a repulsive force relative to the other charge groups.

The relative position of each charge group with respect to the other charge groups produces much of the space charge forces acting upon the system. The space charge potential of the beam is produced by calculating the electric field potential of each charge group and integrating over the length of the beam wavelength to give the electric potential of the beam and averaged to over the volume of the charge group to give the space charge potential between two identical charge groups.

1.8.1 Derivation of the General Amplifier Equations

The derivation for the general amplifier equations in one dimension is presented in this section. The transmission line equation for a one-dimensional line is [50]

$$\partial_z^2 V - \frac{1}{v_p^2}\partial_t^2 V - \frac{2\omega C d_l}{v_p^2}\partial_t V = -\frac{Z_0}{v_p}\left\{\partial_t^2 \rho + 2\omega C d_l\, \partial_t\ \rho\right\} \tag{13}$$

where ρ and V, the charge density and signal amplitude, are functions of z and t. v_p is the characteristic phase velocity of the one-dimensional line, Z_0 is the characteristic interaction impedance. C is the Pierce Gain Parameter, where I_b is the electron beam current and V_0 is the electron beam voltage at the cathode and the attenuation per undisturbed wavelength of the circuit is d_l, defined as

$$d_l = \frac{R}{2\omega LC} \tag{14}$$

C is defined as

$$C^3 = \frac{Z_0 I_b}{4V_0} \tag{15}$$

To derive equation (13), the transmission line equation, consider the equivalent circuit for a TWT as shown in Figure 16 [50].

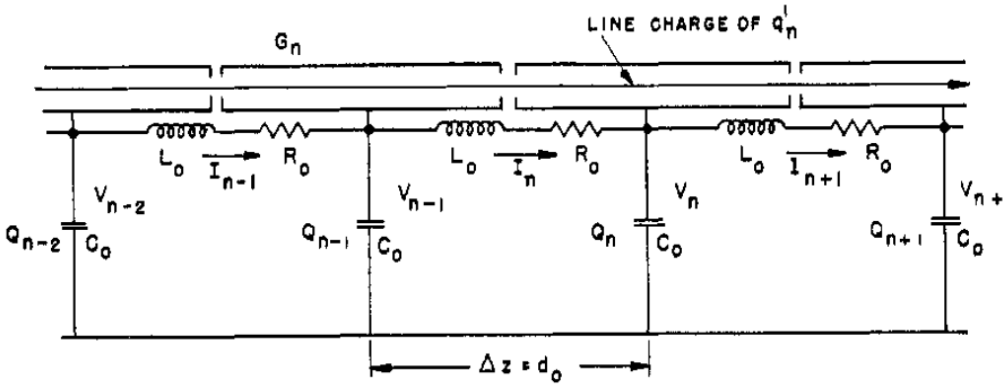

Figure *16* Equivalent circuit for the one dimensional transmission line *[50]*

$$\theta_y(y) = \frac{y}{C} - \omega t - \Phi(y, \Phi_{0,j}) \tag{16}$$

(16) defines the phase lag of the RF signal. It is defined as the phase difference between the RF signal and a hypothetical wave travelling at U_B, which is the initial velocity of the electrons in the electron beam and is a function of the beam voltage V_0. Assuming the phase velocity of the signal and the initial electron velocity are the same, thus satisfying equation (9), the lag exists because of beam loading effects, where the field of the electron beam alters the field of the propagating wave. This means the electric field of the electron beam changes the field of the RF waves such that the phase velocity of the wave changes.

The Lorentz equation (17) is the starting point for which the RF signal's effects upon the electrons is derived.

$$\frac{d\vec{v}}{dt} = -|\eta|\left[\vec{E} + \vec{v} \times \vec{B}\right] \tag{17}$$

The electric field is comprised of the field provided by the signal, the circuit field, and the field electron beam, the space charge field. Splitting these fields gives equation (18).

$$\vec{E} = \vec{E}_c + \vec{E}_{sc} = \vec{\nabla}(V_c + V_{sc}) \tag{18}$$

As we are only interested in the z-component of the fields, when the divergence theorem is applied we obtain equation (19)

$$E(z,t) = \frac{\partial V_c(z,t)}{\partial z} + \frac{\partial V_{sc}(z,t)}{\partial z} \tag{19}$$

And the left-hand side of equation (17) reduces to

$$\frac{dv_z}{dt} = \frac{d^2z}{dt^2} \tag{20}$$

This produces equation (21)

$$\frac{d^2z}{dt^2} = |\eta|\left\{\left[\frac{\partial V_c(z,t)}{\partial z} + \frac{\partial V_{sc}(z,t)}{\partial z}\right]\right\} \tag{21}$$

The last physical phenomena to define is the charge continuity equation, or charge conservation. Consider a small amount of charge entering the field at an input plane [50]. This charge must appear at some other plane sometime later. This is shown mathematically as

$$\rho(z,t)dz = \rho(z,t)dz|_{z=0,t=0} \tag{22}$$

The initial charge density can be described as follows with the initial beam current and the initial electron velocity.

$$\rho(z = 0, t = 0) = \frac{I_0}{u_B} \tag{23}$$

Combining equations (22) and (23) gives the continuity equation of state for the system.

$$\rho(z, t) = \frac{I_0}{u_0}\left|\frac{dz_0}{dz}\right| \tag{24}$$

This set of equations is all that is required to derive the set of generalised amplifier equations when combined with the definitions for the normalised Lagrangian variables.

1.8.2 Normalised Lagrangian Variables

Normalised equations are used to simplify the problem [50]. They are derived using normalised Lagrangian variables. The variables axial position, z, and time, t, are transformed into normalized variables y and $\Phi_{0,j}$ by

$$y = \frac{C\omega z}{u_0} \tag{25}$$

where C is the gain parameter, ω is the angular velocity of the RF signal, z is the unnormalized position along the tube and U_0 is the initial electron velocity, and

$$\Phi_{0,j} = \omega t_{0,j} \tag{26}$$

where $t_{0,j}$ and Φ_0, j are the entry time and phase, relative to the RF signal, respectively. Using the normalised variables described, a normalised expression for the potential of the circuit is defined as [50]

$$V(y, \Phi) = \mathrm{Re}\left[\frac{Z_0 I_0}{C} A(y) e^{-j\Phi}\right] \tag{27}$$

where $A(y)$ is the normalised voltage amplitude of the RF signal at normalised position y.

The normalised velocity is found by visualising the particle velocity in terms of y and $\Phi_{0,j}$, and is expressed in the form

$$u_t(y, \Phi_0) = u_0(1 + 2Cu(y, \Phi_{0,j})) \tag{28}$$

$$\nu_0(y = 0) = \frac{u_0}{1 + C\frac{d\theta}{dy}|_{y=0}} \tag{29}$$

where

$$\frac{d\theta}{dy}|_{y=0} = -b \tag{30}$$

The combination of these equations and the normalised variables lead to the normalised amplifier equations. The transmission line equation is transformed into the circuit equation of the system and is given by

$$\begin{aligned} -C\left(\frac{\omega}{1+Cb}\right) Z_0 I_0 \Bigg[& \frac{d^2A(y)}{dy^2} \\ & - A(y)\left[\left(\frac{1}{C} - \frac{d\theta}{dy}\right)^2 - \left(\frac{1+Cb}{C}\right)^2\right]\Bigg] \cos(\Phi(y, \Phi_0)) \\ + \Bigg[\left(\frac{1}{C} - \frac{d\theta}{dy}\right)\left(-2\frac{dA(y)}{dy}\right) + A(y)\frac{d^2\theta}{dy^2} & \\ & - \frac{2d}{C}(1+Cb)^2 A(y)\Bigg] \sin(\Phi(y, \Phi_0)) \\ = \nu_0 Z_0 \left[\frac{\partial^2 \rho_1}{\partial t^2} + 2\omega d_l \frac{\partial \rho_1}{\partial t}\right] & \end{aligned} \tag{31}$$

The Force equation is given by the combination of the normalised parameters and the Lorentz equation of the form shown in equation (32).

$$\frac{d^2y}{dt^2} = -|\eta|\left\{\frac{Z_0 I_0 \omega}{u_0}\left[\frac{dA(y)}{dy}\cos\left(\Phi(y,\Phi_0)\right) - A(y)\sin(\Phi(y,\Phi_0))\left[\frac{1}{C} - \frac{d\theta}{dy}\right]\right] - E_{sc-z}(y,\Phi)\right\} \quad (32)$$

Lastly, the continuity equation is found by considering the rate of change of z and z_0 with respect to t, time, and is found to be

$$\rho(y,\Phi) = \frac{I_0}{u_0}\left|\frac{d\Phi_0}{d\Phi}\right|\frac{1}{1+2Cu(y,\Phi_0)} \quad (33)$$

1.8.3 Generalised Amplifier Equations

Using the above results, the generalised amplifier equations for a TWT may be found. This set of equations can be used to analyse any helical TWT in the one-dimensional approximation.

To start, the harmonics of the linear charge density must be considered. The linear charge density has many harmonics, but only ρ_1, the fundamental, is considered here. This is because it is assumed that ρ_1 only excites the circuit since Z_{0_1}, the interaction impedance of fundamental frequency dominates. This means that Z_{0_1} is much greater than the interaction impedances of the higher harmonics, or $Z_{0_1} \gg Z_{0_1}, Z_{0_1}, Z_{0_1}$ ….,

While it is possible to consider $\rho_n \forall\, n$, doing so requires knowledge of $Z_{0,n} \forall\, n$, and the additional phase relationships between circuit voltage elements. The Fourier expansion of the beam charge density is analysed at the first frequency harmonic n = 1.

The full Fourier expansion of equation (33) is

$$\rho(z,t) = \sum_{n=1}^{\infty} [A_n \sin(-n\Phi) + B_n \cos(-n\Phi)] \tag{34}$$

Where

$$(-n\Phi) = n\omega t - \int_0^z n\beta(z)dz \tag{35}$$

The Fourier coefficients are

$$A_n = \frac{1}{\pi}\int_0^{2\pi} \rho_n(z,\Phi)\sin(-n\Phi)d\Phi \tag{36}$$

$$B_n = \frac{1}{\pi}\int_0^{2\pi} \rho_n(z,\Phi)\cos(-n\Phi)d\Phi \tag{37}$$

The Lagrangian variable continuity equation (33) is used to write equation (34) as

$$\rho(y,\Phi) = \mathrm{Re}\left[\frac{I_0}{u_0\pi}\sum_{n=1}^{\infty} e^{-jn\Phi}\left\{\int_0^{2\pi}\frac{\cos(\Phi(y,\Phi_0{}'))\,d\Phi_0{}'}{1+2Cu(y,\Phi_0{}')} + j\int_0^{2\pi}\frac{\sin(\Phi(y,\Phi_0{}'))\,d\Phi_0{}'}{1+2Cu(y,\Phi_0{}')}\right\}\right] \tag{38}$$

As we are only interested in n = 1, we use the first term in the series to find the derivatives found in the right-hand side of equation (31), the circuit equation.

$$\rho_1 = \cos\Phi\,\rho_{1c} + \sin\Phi\rho_{1s}\frac{\partial\rho_1}{\partial t} \tag{39}$$

$$\frac{\partial\rho_1}{\partial t} = \frac{\partial\rho_1}{\partial\Phi}\frac{\partial\Phi}{\partial t} \tag{40}$$

$$\frac{\partial^2\rho_1}{\partial t^2} = \frac{\partial\rho_1}{\partial\Phi}\frac{\partial^2\Phi}{\partial t^2} + \left(\frac{\partial\Phi}{\partial t}\right)^2\frac{\partial^2\rho_1}{\partial\Phi^2} \tag{41}$$

Where ρ_{1c} and ρ_{1s} are the integrals from equation (31) for n=1.

From this, we can obtain the general form of the circuit equations describing the beam driven circuit. Since the coefficients on each side of the equation are not functions of Φ and that cos(Φ) and sin(Φ) are orthogonal, all that remains is to equate the coefficients and produce the following two equations.

$$\begin{aligned}&\frac{d^2A(y)}{dy^2} - A(y)\left[\left(\frac{1}{C} - \frac{d\theta(y)}{dy}\right) - \left(\frac{1+Cb}{C}\right)^2\right]\\ &= -\left(\frac{1+Cb}{\pi C}\right)\left[\int_0^{2\pi}\frac{\cos(\Phi(y,\Phi_0{}'))\,d\Phi_0{}'}{1+2Cu(y,\Phi_0{}')}\right.\\ &\left.+\,2Cd_l\int_0^{2\pi}\frac{\sin(\Phi(y,\Phi_0{}'))\,d\Phi_0{}'}{1+2Cu(y,\Phi_0{}')}\right]\end{aligned} \tag{42}$$

$$\begin{aligned}&A(y)\left[\frac{d^2\theta(y)}{dy^2} - \frac{2d_l}{C}(1+Cb)^2\right] + 2\frac{dA(y)}{dy}\left(\frac{d\theta(y)}{dy} - \frac{1}{C}\right)\\ &= -\left(\frac{1+Cb}{\pi C}\right)\left[\int_0^{2\pi}\frac{\sin(\Phi(y,\Phi_0{}'))\,d\Phi_0{}'}{1+2Cu(y,\Phi_0{}')}\right.\\ &\left.-\,2Cd_l\int_0^{2\pi}\frac{\cos(\Phi(y,\Phi_0{}'))\,d\Phi_0{}'}{1+2Cu(y,\Phi_0{}')}\right]\end{aligned} \tag{43}$$

Equations (42) and (43) describe the driving of the circuit fields. The left-hand side of the equations are homogeneous, and the right-hand side of the equations are inhomogeneous because the circuit wave is being driven by the electron beam.

The acceleration of the electron beam is due to the RF field and the internal space charge of the electron beam. The space charge integral is found from the analysis of the harmonics of the linear charge density. It is not enough to calculate the space charge from only the first or first few harmonics: all the harmonics must be considered. This will be discussed in more detail later. The equation for the force experienced by the electron beam is found as [50]

$$\left[1 + 2\mathrm{Cu}(\mathrm{y}, \Phi_0)\frac{\partial \mathrm{u}(\mathrm{y}, \Phi_0)}{\partial \mathrm{y}}\right] = -\mathrm{A}(\mathrm{y})\left[1 - \mathrm{C}\frac{\mathrm{d}\theta(\mathrm{y})}{\mathrm{dy}}\right]\sin\left(\Phi(\mathrm{y}, \Phi_0)\right) + \mathrm{C}\frac{\mathrm{dA}(\mathrm{y})}{\mathrm{dy}}\cos\left(\Phi(\mathrm{y}, \Phi_0)\right) + \mathrm{S.C.} \tag{44}$$

S.C. stands for space charge force. The space charge force is the force felt by an electron from each of the other electrons, and will be considered in the next section.

The final equation of the generalised amplifier equations is the Velocity-Phase equation. This equation relates the change in charge group phase relative to the RF field, the phase lag θ(y) between a hypothetical wave travelling at initial beam velocity u_0 and the RF wave travelling at v_0, and the charge group's normalised velocity, and is given by

$$\frac{\partial \Phi(\mathrm{y}, \Phi_0)}{\partial \mathrm{y}} + \frac{\mathrm{d}\theta(\mathrm{y})}{\mathrm{dy}} = \frac{1}{\mathrm{C}}\left[1 - \frac{1}{1 + 2\mathrm{Cu}(\mathrm{y}, \Phi_0)}\right] \tag{45}$$

The generalised amplifier equations can be used for any configuration of helical of TWTA, for any beam radius, helix radius etc. The method of solving them is to treat the problem as an initial value problem, and to solve the equations at predetermined calculation planes, where the output values at these planes are used as the new initial values, until saturation is reached and the output power of the TWTA is calculated [50] [21].

1.8.4 Space Charge Force

The space charge forces due to the repulsive forces between the electrons in the beam are one of the main parameters needed for correctly modelling the beam wave interaction. This is because energy flow from the DC beam to RF signal relies on how well the device can manipulate the electronic charge group bunching capabilities of the supported RF mode when it interacts with the electron beam, and is greatly affected by space charge.

Space charge causes oscillations, called Langmuir waves. In free space these have an associated frequency known as the plasma oscillation frequency, which arises whenever there is a perturbation. It is like a pressure-density wave. The disturbance may be in the form of an electromagnetic wave, from an external source or from the movement of neighbouring electrons. The plasma oscillation frequency affects the strength of the axial space charge forces, or more precisely, may damp the forces. In metallic confinement, such as in a waveguide, the plasma frequency is reduced due to interactions with the conducting walls of the waveguide and is a function of distance between the boundary and the electron beam. This reduction is modelled by introducing a

value called the plasma frequency reduction factor. For a waveguide with cylindrical symmetry, the plasma frequency reduction factor is constant for all angles perpendicular to the axis of motion and acts to lessen the oscillation frequency of the space charge oscillations, and as such reduce the effect of space charge forces [50] [21].

In the one-dimensional case, the axial component of the electronic space charge force is considered. This describes how the electron bunches repel each other axially along the circuit and is responsible for some of the bunching effects modelled in the simulations. For the proposed code, a simple version of the axial space charge force was considered, which gives the space charge integral the form [50]

$$\frac{1}{(1+\mathrm{Cb})}\left(\frac{\omega_p}{\omega}\right)^2 \int_0^{2\pi} \frac{e^{|\Phi-\Phi_0'|}\,\mathrm{sgn}(\Phi-\Phi_0')\mathrm{d}\Phi_0'}{1+2\mathrm{Cu}(y,\Phi_0')} = F_{1-z}(\Phi-\Phi_0') = e^{\frac{u_0|\Phi-\Phi_0'|}{\omega b'}}\,\mathrm{sgn}(\Phi-\Phi_0') \tag{46}$$

This expression sums over the force felt by a reference electron group caused by each other electron group. This gives an approximate value for the space charge force. This is convenient as the explicit solution would require the calculation of many Bessel's functions per iteration of the code.

1.8.5 Space Charge waves

If one considers an infinite one-dimensional slab of electric charge, perturbed in some way by a small factor in the z-direction, δz, an oscillation is produced. The charge density of this can be described as

$$\sigma = en\delta z \tag{47}$$

where e is the electronic charge and n is the number of electronic charges on this leading face.

An equal and opposite charge density will be produced due to this perturbation, and will produce an electric field of the form

$$E_z = -\frac{\sigma}{\epsilon_0} = -en\delta z/\epsilon_0 \tag{48}$$

Applying Newton's law to this equation we obtain

$$m\frac{d^2\delta z}{dt^2} = eE_x = -m\omega_p^2\delta z \tag{49}$$

which when combined with equation (48) produces

$$-m\omega_p^2\delta z = -ne^2\delta z/\epsilon_0 \tag{50}$$

Simplifying to

$$\omega_p^2 = \frac{ne^2}{\epsilon_0 m} \tag{51}$$

where m is the mass of an electron. This equation can be rewritten as

$$\omega_p^2 = \frac{eI_D}{m\epsilon_0 u_0} \tag{52}$$

Where I_D is the dc current density and u_0 is the dc beam velocity, defined as

$$U_B = \sqrt{(\frac{2Ve}{m})} \tag{53}$$

In any finite electron beam, fringing effects reduce the longitudinal electric field, and in the case of an electron beam confined by conducting surfaces, fringing is further increased. This is due to the geometry of the tube, and the shape of the electric field between the beam and the wall. Due to this fringing effect, the plasma oscillation frequency is reduced.

To derive the plasma frequency reduction factor, first, we must derive the propagation constant of the space charge waves relating to the reduced frequency.

First, we consider Maxwell's equations.

$$\vec{\mathrm{E}} = -\Delta\Phi_{\mathrm{E}} - \frac{1}{\mathrm{c}}\frac{\partial\overrightarrow{\mathrm{A_H}}}{\partial \mathrm{t}} \tag{54}$$

$$\vec{\mathrm{H}} = \nabla \times \overrightarrow{\mathrm{A_H}} \tag{55}$$

Where E is the electric field vector, H is the magnetic field vector, Φ_{E} is the scalar potential of the electric field, and $\mathrm{A_H}$ is the magnetic potential vector. These reduce in the wave equations

$$\left[\nabla^2 - \frac{1}{\mathrm{c}^2}\frac{\partial^2}{\partial \mathrm{t}^2}\right]\Phi_{\mathrm{E}} = \rho \tag{56}$$

$$\left[\nabla^2 - \frac{1}{\mathrm{c}^2}\frac{\partial^2}{\partial \mathrm{t}^2}\right]\overrightarrow{\mathrm{A_H}} = \frac{-\rho\vec{\mathrm{v}}}{\mathrm{c}} \tag{57}$$

$$\nabla \cdot \overrightarrow{\mathrm{A_H}} = -\frac{1}{\mathrm{c}}\frac{\partial\Phi_{\mathrm{E}}}{\partial \mathrm{t}} \tag{58}$$

Only the wave solution is desired, so it is useful to denote the scalar electric potential, charge density, and velocity respectively, as

$$\Phi_{\mathrm{E}} = \Phi_1 \mathrm{e}^{\mathrm{i}(\omega \mathrm{t} - \gamma \mathrm{z})} \qquad \rho = \rho_1 \mathrm{e}^{\mathrm{i}(\omega \mathrm{t} - \gamma \mathrm{z})} \qquad \mathrm{v} = \mathrm{v_z} \mathrm{e}^{\mathrm{i}(\omega \mathrm{t} - \gamma \mathrm{z})}$$

Equations (56) and (57) can be written in terms of cylindrical coordinates to give

$$\frac{\partial^2\Phi_1}{\partial \mathrm{r}^2} + \frac{1}{\mathrm{r}}\frac{\partial\Phi_1}{\partial \mathrm{r}} + \frac{1}{\mathrm{r}^2}\frac{\partial^2\Phi_1}{\partial \theta} + (\mathrm{k}^2 - \gamma^2)\Phi_1 = \rho_1 \tag{59}$$

ρ_1 may be written in terms as Φ_{E_1} as

$$\rho_1 = \frac{e\rho_0}{m}\frac{\gamma^2 - k^2}{(\omega - \gamma v_0)}\Phi_{E_1} \tag{60}$$

Which gives

$$\frac{\partial^2\Phi_{E_1}}{\partial r^2} + \frac{1}{r}\frac{\partial\Phi_{E_1}}{\partial r} + \frac{1}{r^2}\frac{\partial^2\Phi_{E_1}}{\partial\theta} + (k^2 - \gamma^2)\left[1 - \frac{e\rho_0}{m(\omega - \gamma v_0)^2}\right]\Phi_{E_1} = 0 \tag{61}$$

with a solution is given in the form

$$\Phi_{E_1} = B_n J_n(Tr)e^{in\theta} \tag{62}$$

where B_n is a constant, J_n is the n^{th} Bessel's function of the first kind, and T is

$$T = \left\{(k^2 - \gamma^2)\left[1 - \frac{e\rho_0}{m(\omega - \gamma v_0)^2}\right]\right\}^{1/2} \tag{63}$$

In the space between the electron plasma and the conducting walls of the tube, the solution is known as

$$\Phi_{E_2} = C_n(I_n(\tau r) + D_n K_n(\tau r)) \tag{64}$$

Where C_n and D_n are constants to be determined, I_n, and K_n are modified Bessel functions. τ is defined as

$$\tau = (\gamma^2 - k^2)^{1/2} = \omega/u_0 \tag{65}$$

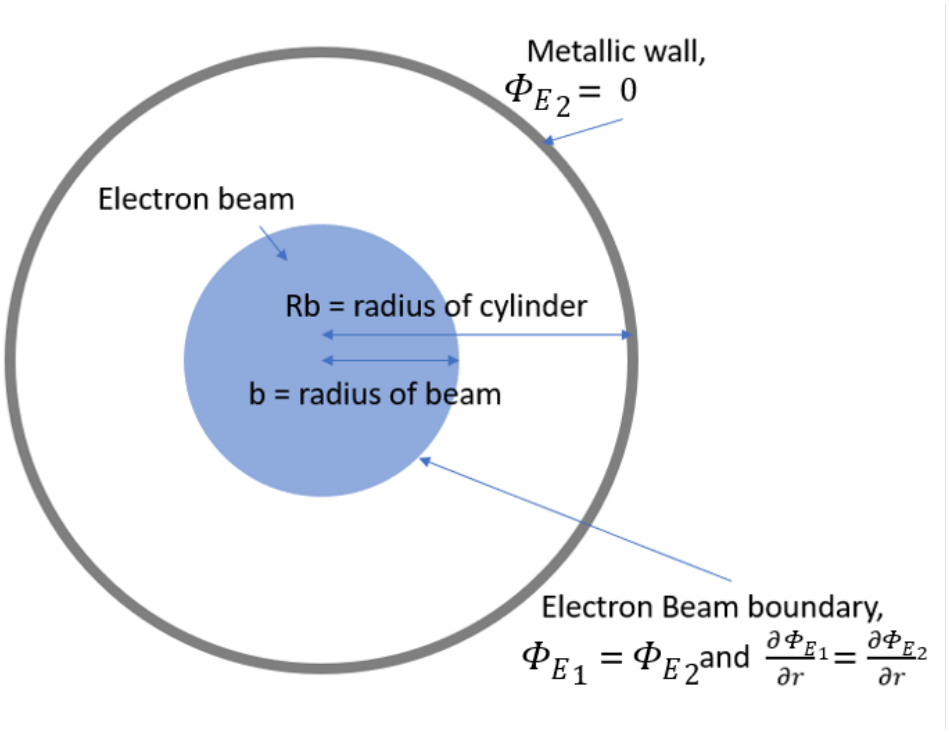

Figure 17 Diagram of the boundary conditions used to solve equation (62) and (64)

Figure 17 shows the boundary conditions for the solution. The constant D_n is determined by considering the tangential electric field at $r = Rb$, the conducting wall, where the tangential electric field must equal zero. That is

$$\Phi_{E_2}|_{r=Rb} = 0 \tag{66}$$

Thus, by solving equation (64) for the condition stipulated in equation (66), we obtain

$$D_n = -\frac{I_n(\tau Rb)}{K_n(\tau Rb)} \tag{67}$$

The conditions left to be satisfied are at $r = b$, the beam radius. The field must be continuous at this point, which means equation (68) and equation (69) must be satisfied. This condition will be used to determine the ratio of C_n/B_n, and to consider γ in terms of the given parameters.

$$\Phi_{E_1}|_{r=b} = \Phi_{E_2}|_{r=b} \tag{68}$$

$$\frac{\partial \Phi_{E_1}}{\partial r}|_{r=b} = \frac{\partial \Phi_{E_2}}{\partial r}|_{r=b} \tag{69}$$

Equating equation (62) and equation (64) yields equation (70)

$$\frac{C_n}{B_n} = \frac{I_n(\tau b) + D_n K_n(\tau b)}{J_n(Tb)} \tag{70}$$

And differentiating both equation (62) and equation (64) and equating the results gives

$$\frac{C_n}{B_n} = \frac{(\tau b)}{(Tb)} \frac{I_n'(\tau b) + D_n K_n'(\tau b)}{J_n'(Tb)} \tag{71}$$

Which when combined and rearranged leads to the transcendental equation

$$(Tb)\frac{J_n'(Tb)}{J_n(Tb)} = (\tau b)\frac{I_n'(\tau b) + D_n K_n'(\tau b)}{I_n(\tau b) + D_n K_n(\tau b)} \tag{72}$$

Equation (68) may be numerically solved for T, and then T substituted into equation (69) to find the plasma frequency reduction factor [57] [58].

$$\frac{\omega_q}{\omega_p} = \sqrt{\frac{1}{1 + \left(\frac{T}{\tau}\right)^2}} \tag{73}$$

1.8.6 Weighting Functions

The electromagnetic field supported in TWT or BWO is not uniform. The field changes as a function of radius in the case of the helical TWT. This can be modelled using weighting functions. The advantage of weighting functions comes from being able to maintain a single valued interaction impedance, even though different parts of the beam will experience more or less coupling to the wave than other parts.

Figure 18 shows the electric field for a helical TWT. For the cases of cylindrical symmetry such as this, the radially dependent electric field strength, equation (74) [50] may be used to calculate rotationally invariant weighting functions for different parts of the beam separated radially.

$$f(r) = \frac{I_0^2(\tau b) - I_1^2(\tau b)}{I_0^2(\tau r)} \tag{74}$$

This method requires only knowledge of the frequency, the voltage of the electron beam, the radius of the tube and radius of the electron beam, or the radius of the charge group in the electron beam for subdivided configurations. As such, equation (74) is not a function of angular position of the electronic charge group, as would be expected for a cylindrically symmetric system.

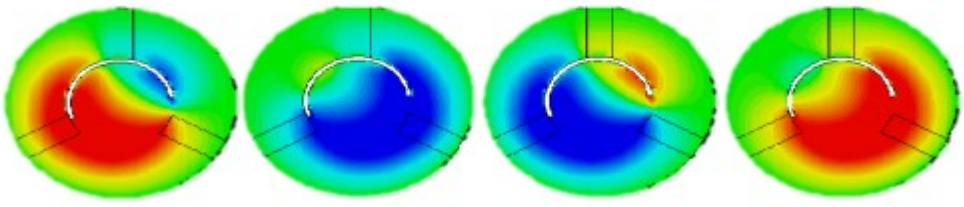

Figure 18 The electric field in a helix based TWT. On average the field is asymmetric, and only relies upon radial position.

1.8.7 Eigenmode and Finite Difference Time Domain Simulation

Fully three-dimensional (3D) solver, such as CST [59] and MAGIC3D use a different approach to solving electromagnetic systems. They solve Maxwell's Equations directly in either integral form or differential form using linear algebraic techniques. These are powerful tools, as many structures are not analytically solvable due to extremely irregular shapes. In terms of TWT design, two solvers are used; eigenmode simulations and finite difference time domain (FDTD).

Eigenmode simulations calculate the cold parameter of a SWS. The cold parameters refer to the structure in the presence of a RF wave but no electron beam. The eigenmode of a given closed-region possess a discrete spectrum of frequencies. The simulation considers a closed region in the form of a single period of the SWS being designed. The frequencies of the dispersion curve correspond to allowed values of the propagation constant as a function of the range of phase differences being investigated [60]. The average power flow through the period is also calculated. This data is used to calculate the interaction impedance of the SWS. By the dispersion curve the synchronous beam voltage is obtained.

The eigenmode simulator uses either the Advanced Krylov Subspace method or the Jacobi-Davidson method to solve Maxwell's equations for the closed resonant structures, such as a single period of a SWS [61].

FDTD is used to calculate the S-Parameters of the full structure and the full hot-test simulation of the device. To discretize Maxwell's equations with second-order accuracy for homogeneous regions where there are no discontinuous material boundaries, FDTD methods store different field components for

different grid locations. This discretization is known as a Yee lattice. The Yee lattice in the 3D case is shown in Figure 19 [62].

For the hot simulations the PIC solver is used. Hot simulation means the interaction of the electron beam and the signal is simulated using an electron beam with an initial radius, current and voltage, and signal with a single frequency and initial power. The PIC solver is self-consistent, which means the solver takes the fields produced by the particles directly for each time step of the simulation. This makes it ideal for TWTs and BWOs, where the nonlinearity of the interaction between particles and fields is of great importance [63].

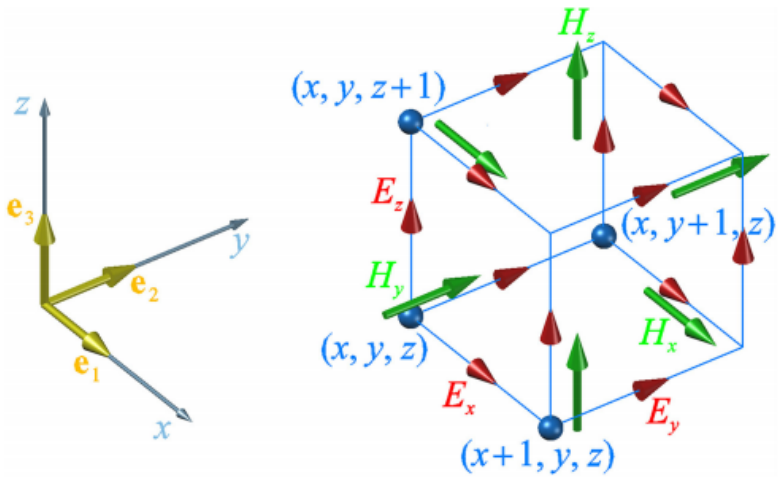

Figure *19* Yee Lattice *[62]*

1.8.8 Performance and comparison

Full 3D simulators are general purpose tools, meaning they can solve for arbitrary structures, like the DCW TWT or the FW TWT. The general amplifier equations were derived above for the TWT. However, these Lagrangian codes only work for structures with a specific symmetry in the form of cylindrical symmetry. The cost of being general purpose comes in the form of large

computational effort and time. Lagrangian codes for specific structure may take on the order of minutes [64], whilst fully 3D simulators may take of order tens hours [23].

1.9 Conclusions

The helix is a good SWS for amplifiers and oscillators up to about 60 GHz. Above that, the structure becomes too small to reliably manufacture, and are fragile. Different SWSs are required for higher frequency amplification in the mm-wave and THz frequency regime.

The DCW is a promising SWS for the mm-wave and THz frequency regime. This is because of the viable fabrication techniques CNC-milling and LIGA, as well as easy construction.

Lagrangian simulators can be fast methods of simulating many variations of a TWT or BWO in a short period of time. Lagrangian simulators exist for TWTs and BWOs with helix SWSs. However, there is no Lagrangian simulator for asymmetric structures. As such, it would be useful to have a Lagrangian simulator to expedite the design process of asymmetric SWS suitable for mm-wave and THz frequency regime.

1.10 Organisation of the Thesis

The thesis is organised in the following manner. Chapter 2 describes the novel Lagrangian method for asymmetric SWSs. The motivation for this part of the thesis is driven by the need for a fast method of simulating beam-wave interaction in TWTs and BWOs in the mm-wave frequency regime, where novel

periodic structures are required for use as the SWS of the tube, due to helices being unsuitable.

The definitions of the large signal model, including the methods for calculating the space charge forces acting upon the electron beam, and the weighting functions describing the field distribution caused by the SWS, are presented.

The novel modifications proposed are described in detail, as is the structure of the code used to validate the model. The validation is performed by comparison of the output of the code with the output of 3D electromagnetic simulations. The outputs compared are the saturation point and power output.

Chapter 3 describes the design of DCWs at novel frequencies, for mm-wave TWTs, and uses CST-MWS as the simulation software. The motivation comes from advances in micro-fabrication technology allowing for the realisation of structures small enough to be useful in new high frequency regimes such as mm-waves and THz frequencies. The comparison of two tapering configurations for coupling the SWS to input and output waveguides are described. These two configurations are the lateral tapering of the pillars, and the height tapering of the pillars of the DCW. The S_{11} and S_{21} S-parameters are presented, as well as the field distribution at the transition from TE_{10} supported by the input waveguide to the hybrid TE_{10} mode supported by the DCW. A 346 GHz BWO is used for the purpose.

A DCW for use in a BWO operating at 100 GHz is described, as well as a TWT operating with a central frequency of 270 GHz. The dispersion relation of the periodic structures is analysed for the phase velocity of the relevant spatial harmonic, to calculate the synchronous beam voltage, and the interaction impedances as a function of frequency is presented.

The tapering configuration for these two DCWs, utilising the lateral tapering configuration, is also described, with the S_{11} and S_{21} parameters being presented with the TE_{10} to hybrid TE_{10} mode transition.

A W-band DCW is also described with an operating frequency band of 92-95 GHz for use in wireless applications. Two configurations for the DCW SWS are discussed; the square pillared DCW and the triangular pillared DCW. A bend taper is described in which the pillars near where the electron beam enters the tube must be altered in shape to allow room for the electron beam to propagate. The $S_{11}$and S_{21} parameters for the bend taper with no alterations and the bend taper with alterations are presented and compared.

General conclusions are then discussed, as well as limitations of the work and added insights with opportunities for future work.

Chapter 2 Novel approach to Large Signal Lagrangian for Asymmetric SWSs

Full 3D simulators are general purpose. They may simulate a large range of different electromagnetic systems. This makes them powerful but slow when using conventional computers. Specialist simulators, written for a single device, such as Lagrangian simulator can be very fast. Lagrangian simulators exist for helical and coupled cavity SWS TWT and BWO but are not accurate for TWTs utilising the asymmetrical structures as the DCW. This has been explained in detail in Chapter 1.

The problem to be solved here is to modify the helical waveguide solution for accurate simulations of the DCW, taking into account the lack of rotational symmetry exhibited by this waveguide configuration.

A novel approach to the large signal model based on the modified Lagrangian theory for helical waveguide circuit will be described. The approach changes how space charge forces are modelled. Weighting functions corresponding to not only radial position, but also axial positions are utilised, and factors which affect space charge forces are considered in a novel way. The Lagrangian equations derived previously will model the interaction between the beam and the RF signal and will do so in terms of the circuit field amplitude, and normalised electronic charge group velocity and phase. The 3D simulator CST will be utilised in the calculation of the input variables required for the calculation of the weighing functions at low computational cost. An eigenmode simulation is not computationally intensive and may take much less than 1 hour to complete. The modified Lagrangian code will be validated by comparison with

the results of a Ka-band DCW TWT [65]. This structure was originally simulated in CST-PS (particle studio) [59]. Comparisons will be made between the saturation point of the interaction and the output powers simulated via each method.

2.1 Large Signal Model

Differently from the helix, most novel SWSs designed to be used in the mm-wave and THz TWTs present non-cylindrical symmetry, but arbitrary symmetry. This means, when rotated about the beam axis, the structure does not look the same at any angle of rotation except for a few specific angles dependent on the structure. The DCW is an SWS with this property. This affects the computation of the space charge, as the plasma frequency reduction factor is not constant. It is instead a function of the space between the beam and the surrounding metal structure. A different method of calculating a plasma frequency reduction factor must be found. Space charge is discussed in detail in Chapter 1.

The model proposed is based on the one-dimensional Lagrangian equations of motion of electrons and the beam-wave interaction between the electrons and RF wave as derived by Rowe [48] [50], also presented in Chapter 1.

2.2 Modification to the Lagrangian Model

In the case of cylindrical symmetry, a single value for the plasma frequency reduction factor is enough for modelling this damping. Solving equation (72) yields the radial propagation constant of the space charge waves and using the value $\tau = \omega/u_0$, the plasma frequency reduction factor can be found for a given

tube radii and beam radii. However, if the structure is not rotationally symmetric, there is no single value for the plasma frequency reduction factor. Similarly, the electric field values in structures with no rotational symmetry cannot be solved for with a simple equation such as equation (74). Further, structures such as the DCW have a varying axial electric field, above the natural oscillations of the wave, giving rise to increased complexity.

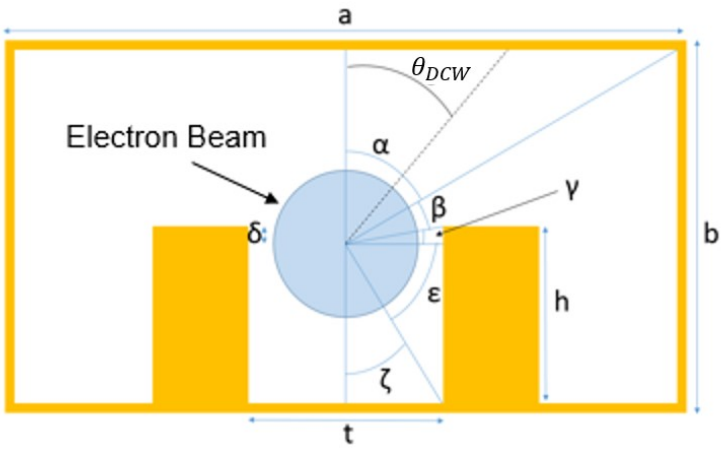

Figure *20* Cross section of the DCW TWT. The radius is not singularly valued as the helical SWS. Also shown are the definitions of angles for the calculation of effective radii

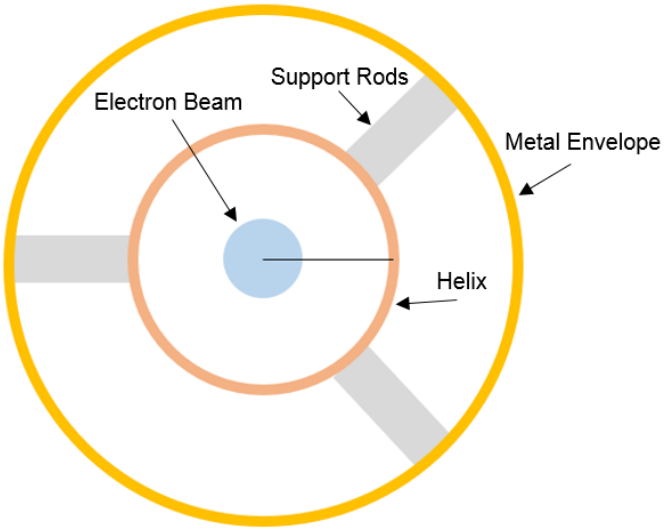

Figure *21* Cross section of the helical waveguide with the outer copper casing, the inner helical SWS, the electron beam in the centre, and the dielectric support rods. The black line shows the radius of the helix with respect to the beam centre

2.2.1 Non-cylindrically Symmetric Configurations

As shown in Figure 20 and Figure 21, the DCW has a non-rotationally symmetric geometry. Shown in Figure 22 is the effective radii for the DCW. For a given angle perpendicular to the z-axis of a DCW, different distances from the

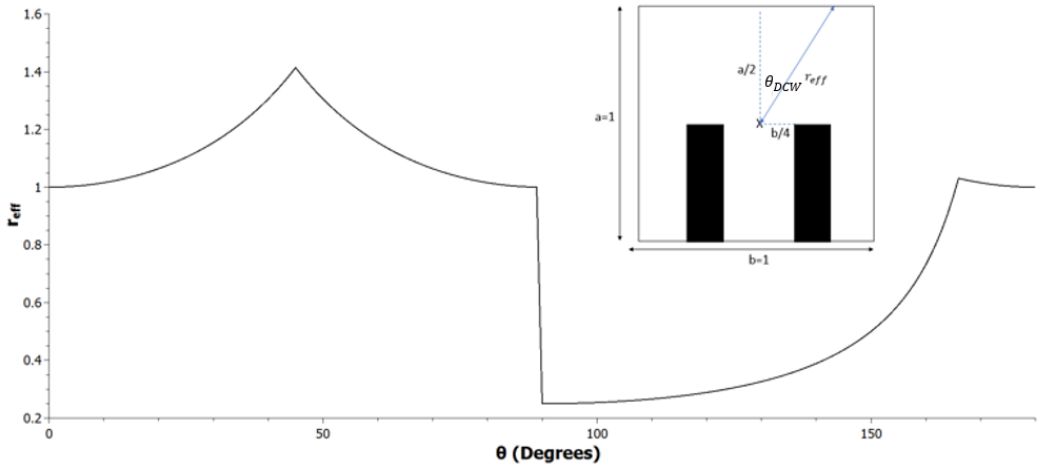

Figure *22* Effective radii for space charge calculations example. In this case, a unit DCW is used. Inset is the unit DCW

axis to the nearest edge will be observed as a function of angle. Between the pillars, a range of angle will result in observing the nearest section of the structure to be farther or closer. The space charge forces which are affected by the proximity to the conducting walls are non-rotationally symmetric due to the dependence on the radius of the waveguide, or more specifically, the plasma frequency reduction factor is a function of the radius of the tube, and the radius of the electron beam. As the DCW has no cylindrical symmetry, a piece-wise like solution, whereby each section of the electron beam with a different distance from the walls of the waveguide, or ‘effective radius’, will have its own plasma frequency reduction factor, independent of those of the other charge groups, could be of use. Each portion of the beam will experience different

space charge forces. The axial space charge forces are largely a function of frequency, beam size and tube radius, and although an exact analytically solvable solution does not exist, the plasma frequency reduction factor, which has the major effect on the gain of the tube, can be numerically solved for each section of the electron beam.

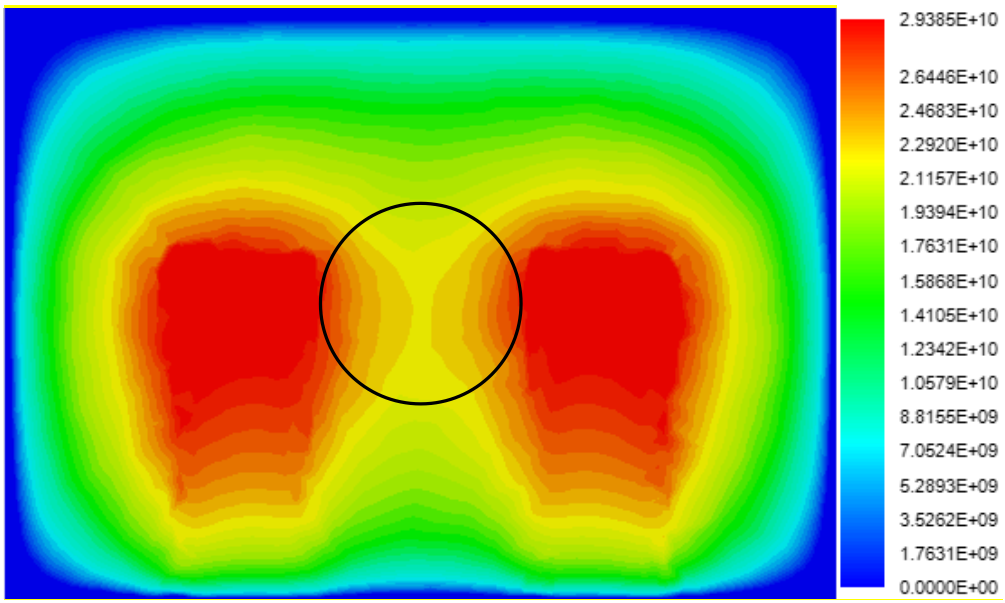

Figure 23 The field distribution of the DCW, with approximate beam position shown. Computed in CST-MWS [59] *The red is high electric field strength and the blue is low electric field strength.*

Similarly, the electric field distribution, and as such the interaction impedance seen by each sub divisions will vary with radial and angular position. Varying electric field strength inside the DCW is shown in Figure 23. Each sub division must be assigned a weighting function corresponding to its position in the field. These values can be calculated using either an electromagnetic model of the SWS or by eigenmode simulator.

The electric field values can be computed along any desired curve and used to calculate weighting functions with the aid of the interaction impedance values.

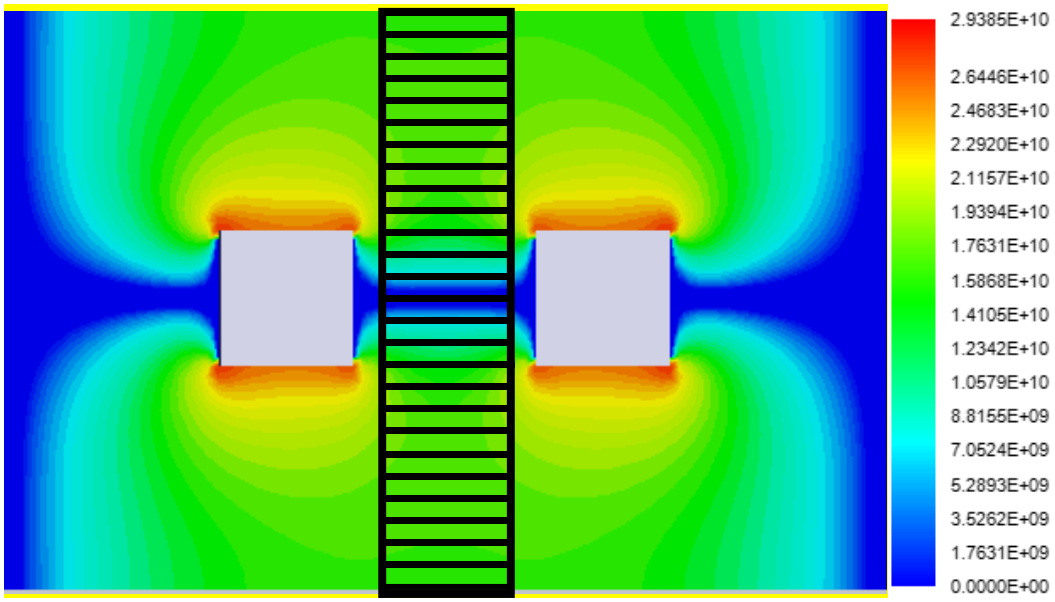

Figure *24* Axial Field variance of a DCW *[59]* The red is high electric field strength and the blue is low electric field strength

Axial variations in the field strength and so interaction impedance is also an issue to be considered. Figure 24 shows a top down view of an DCW period. The black boxes signify electronic charge groups of the electron beam.

2.2.2 Rotational Asymmetry in Space Charge

In the Lagrangian formulation, the electron beam is split into several charge groups, each occupying a given initial phase position relative to the pre-beam loaded RF signal, with the reduced wavelength of the wave with respect to the mode of the field in the SWS. These charge groups can move independently of each other, apart from the electromagnetic interactions. The charge groups are further sub-divided in terms of radial distribution and angular distribution of charge. These are called sub-charge groups.

The sub divisions are shown in Figure 25.

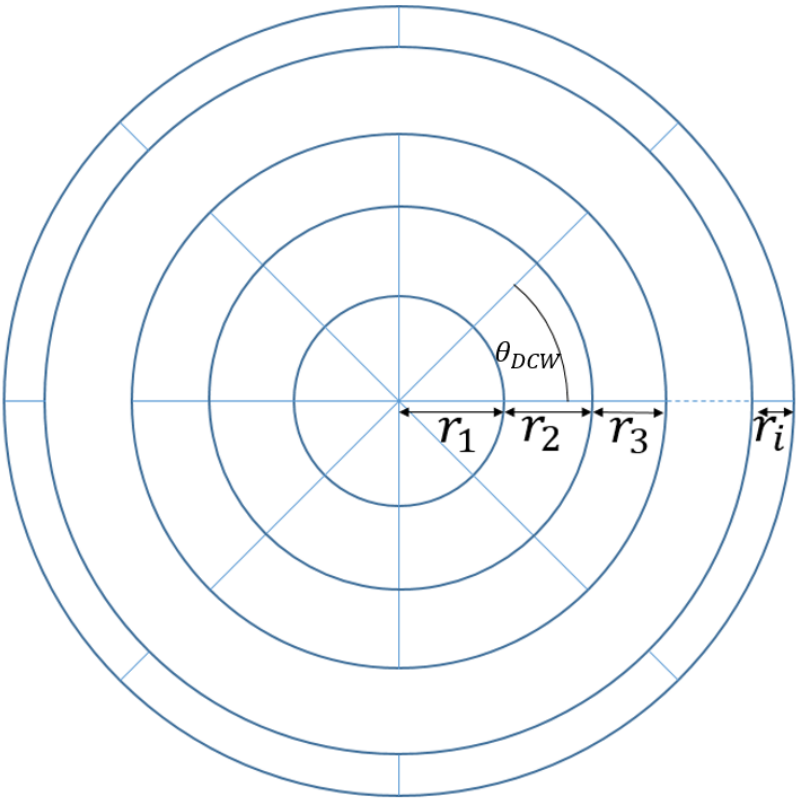

Figure *25* Sub-charge group model, where θ is defined in equation 12 and r_i is defined in equation (13)

A tube such as the DCW has no well-defined single valued radius. Equations for calculating the effective radius of such a structure have been derived. Conveniently, only the RF frequency, beam voltage, beam radius and tube radius are required to find the solution to equation (72) and (73), so to find an plasma frequency reduction factor merely requires the definition of the effective radius, given by equations (75) and (76). α and ϵ are defined in Figure 20.

$$\mathrm{r'}(\theta_{\mathrm{DCW}}) = \begin{cases} [\mathrm{b}-(\mathrm{h}-\delta)][1+\tan(\theta_{\mathrm{DCW}})]^{\frac{1}{2}} \text{ for } \theta_{\mathrm{DCW}} < \alpha \\ \left[\frac{\mathrm{a}^2}{4}+[\mathrm{b}-(\mathrm{h}-\delta)]^2\right]^{\frac{1}{2}} \text{ for } \theta_{\mathrm{DCW}} = \alpha \\ \frac{\mathrm{a}}{2}[1+\cot(\theta_{\mathrm{DCW}})]^{1/2} \text{ for } \theta_{\mathrm{DCW}} > \alpha \end{cases} \tag{75}$$

$$r'(\theta_{DCW}) = \begin{cases} \dfrac{t/2}{\cos(\theta_{DCW} - \pi/2)} & \text{for } \theta_{DCW} < \epsilon \\ \dfrac{h - \delta}{\sin(\theta_{DCW} - \frac{\pi}{2})} & \text{for } \theta_{DCW} > \epsilon \end{cases} \quad (76)$$

The effective radii and range of T from equation (72) and equation (73) being tested are used by a code written using MATLAB [66]. An array for each side of the equation is produced. An element wise division is then performed. Element wise means that the corresponding element in each array are divided. Consider two matrices with i columns and j rows, called A and B. Element $A_{i,j}$ of the array A is divided by element $B_{i,j}$ of array B. The elements after this operation that are not close to unity are discarded. The interception points, and so the roots of the transcendental equation are found.

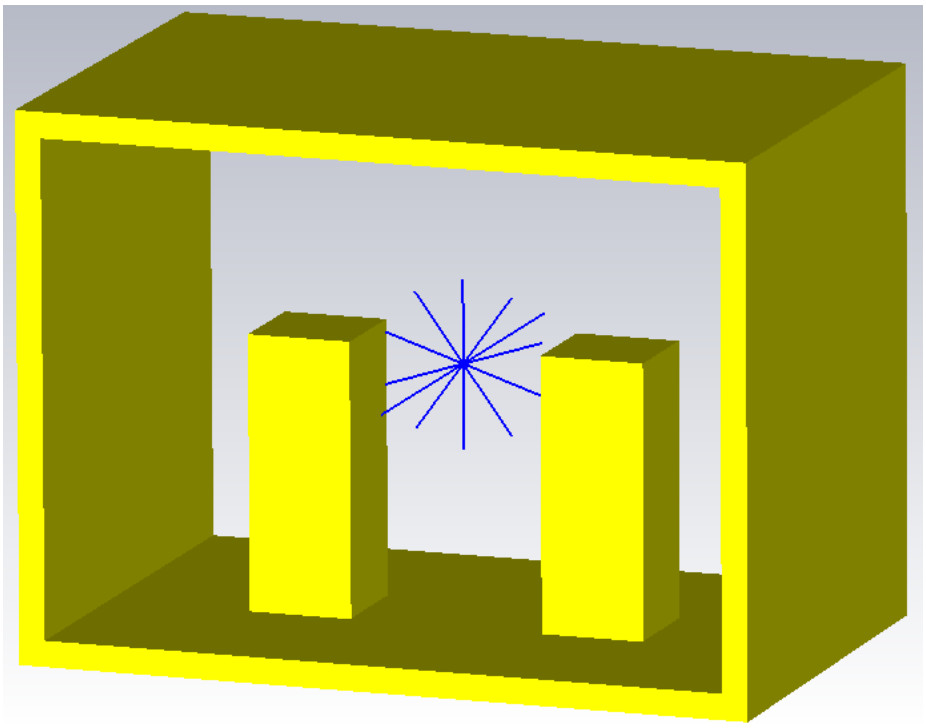

Figure *26* The field values were extracted along the lines shown above, with 10 radial lines for r=0 to r = b_r = beam radius, and one axial line one period in length. They were calculated in CST MWS Eigenmode solver

There are an infinite number of intersection points, but we limit the computation to the first order solutions. Each of these roots T is fed into equation (68), which produces a set of plasma reduction factors dependent on θ , i.e. the angular position in the waveguide, or more precisely, the beam.

2.2.3 Rotational Asymmetry in electric field

The interaction impedance, shown in equation (7), of the circuit is an important factor in the process of solving for the gain of the tube. However, as the interaction impedance is a function of the electric field, and the electric field doesn't vary in a rotationally symmetric way, a method of finding coupling factors is required. As stated, for a tube of cylindrical topology, the weighting function is solvable analytically.

Each charge group is sub-divided into concentric rings and sectors, N_r rings and N_c sections providing in total $N_r \times N_c$ sub charge groups. These sub charge

$$C = \sqrt[3]{\frac{K_z I_0}{4V_0}} \tag{77}$$

groups can be assigned independent weighting factors associated with the field variance over a 2-dimensional slice of one period of an SWS, taken at the centre of one period of the structure. The field was extracted along N_c lines constrained by the radius of the electron beam. Each of the lines were angularly separated by $360/N_c$ degrees, and radially extended from the centre of the beam to the radial edge of the beam, giving each line a length of the beam radius b_r, so the field is known at the electron beams position. The electric field values $E(\theta, r)$ along each line and the on-axis interaction impedance at the phase value corresponding the phase difference of the frequency can be

extracted from CST. The lines along which the values were extracted is shown in Figure 26. Equation (7) where K_z is the interaction impedance, and β and P_f are the propagation constant and power flow of the wave respectively, are used to calculate the electric field value associated with the on-axis interaction impedance. Then, each field value was normalised with respect to this value, resulting in an initial set of weighting functions. The angles and radii of the lines are calculated using equation (78) and equations (79) respectively [50].

$$\theta_S = \frac{360}{N_c} \tag{78}$$

$$r_i = b_r \sqrt{\frac{i}{r}} \tag{79}$$

2.2.4 Axial Variation in electric field

The axial weighting function derived for the double corrugated waveguide relies on knowing where each electronic charge group exists relative to the SWS at each iteration of the code.

We assume that the system of electrons and RF wave are moving at a constant velocity of initial electron velocity u_B, so each iteration step has a constant shift in distance, δy.

The supported mode of the signal in the DCW, a hybrid TE_{10} mode, forces the wavelength of the signal in the structure to be near the periodicity of the structure, but not exactly. As such, a factor to account for the difference in length of the period to the wavelength must be introduced. This is defined as

$$F_z = \frac{\lambda'}{P} \tag{80}$$

Where F_z is the axial filling factor, or the amount of the structure 'filled' by one wavelength of the signal per period, λ' is the wavelength in the structure as a function of frequency, a P is the period of the structure.

To find the fraction of one period at which the charge group exists, we must take the phase position of the charge group $\Phi(y = y_0, \phi_0)$, where y is the normalised position of the charge group, Φ_0 is the initial phase position of the charge group. Dividing this by 2π gives an absolute value of the position of the charge group relative to the SWS, or a periodic phase. This operation, however, assumes that the spread of the electrons initially is equal to the period of the structure; that is, $\lambda' = P$.

As such, the next step is to multiply the periodic phase by the axial filling factor, giving

$$\Phi_P(y = y_0, \phi_0) = \frac{\Phi(y = y_0, \phi_0)}{2\pi} F_z = \frac{\Phi(y = y_0, \phi_0)}{2\pi} \frac{\lambda'}{P} \tag{81}$$

This gives the periodic phase for the initial configuration of the signal, electron beam and SWS. However, the RF signal and electron beam are moving, and so this must be considered to solve for the dynamic case.

Each integration step moves the RF signal forward by an amount defined as δz, and in terms of fractions of the period, gives

$$\delta\Phi_P = \frac{n\delta z}{P} \tag{82}$$

Giving a dynamic periodic phase defined as

$$\Phi_P(y = y_0, \phi_0) = \frac{\Phi(y = y_0, \phi_0)}{2\pi} \frac{\lambda'}{P} + \frac{n\delta z}{P} \tag{83}$$

Which may be reduced to

$$\Phi_P(y = y_0, \phi_0) = \frac{\Phi(y = y_0, \phi_0)}{\beta P} + \frac{n\delta z}{P} \tag{84}$$

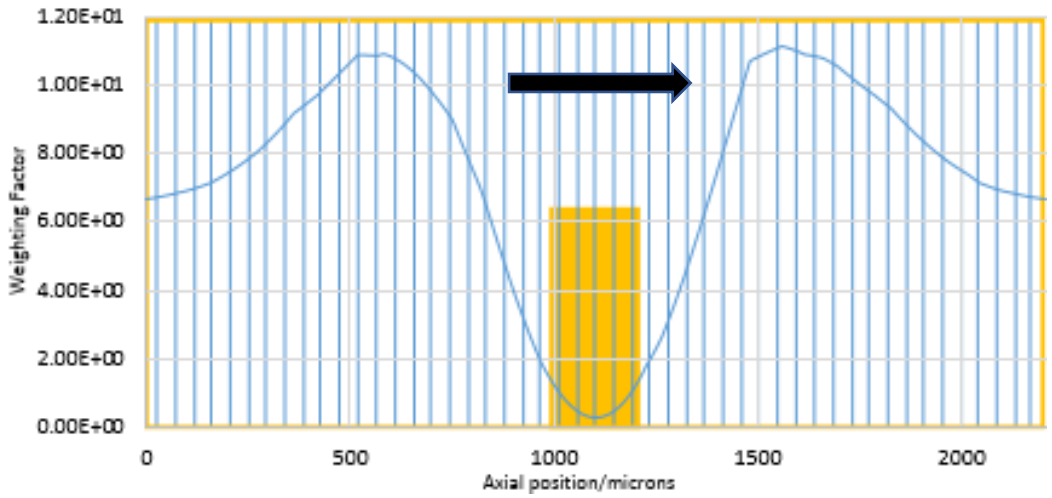

Figure 27 Example of axial variation of electric field for a DCW in the Ka-band along the z-axis. This was calculated using CST *[59]* The black arrow indicates the beam direction

Figure 27 shows the axial weighting functions of an example DCW. The periodic phase position of the electronic charge group is calculated using equation (84) and a weighting factor is applied with regards to the values in Figure 27.

2.2.5 Applying the Weighting Functions

The weighting functions are used in the circuit equations of the system. This is because the circuit equations calculate the amount of energy being transferred from the electron beam to the RF wave per integration step. The weighting function is to adjust this energy transfer from each sub-charge group dependent on its position in the field. This is done by multiplying the integration for each sub-charge group per radial and angular position weighting function. This is

then multiplied by the axial weighting factor of the average position of the electronic charge groups. This produces, from equations (42) and (43)

$$\frac{d^2A(y)}{dy^2} - A(y)\left[\left(\frac{1}{C} - \frac{d\theta(y)}{dy}\right) - \left(\frac{1+Cb}{C}\right)^2\right]$$
$$= -\frac{F_{tot}(r,\theta)}{N}\left(\frac{1+Cb}{\pi C}\right)\left[\int_0^{2\pi}\frac{\cos(\Phi(y,\Phi_0{}'))\,d\Phi_0{}'}{1+2Cu(y,\Phi_0{}')}\right. \quad (85)$$
$$\left. + 2Cd\int_0^{2\pi}\frac{\sin(\Phi(y,\Phi_0{}'))\,d\Phi_0{}'}{1+2Cu(y,\Phi_0{}')}\right]$$

$$A(y)\left[\frac{d^2\theta(y)}{dy^2} - \frac{2d}{C}(1+Cb)^2\right] + 2\frac{dA(y)}{dy}\left(\frac{d\theta(y)}{dy} - \frac{1}{C}\right)$$
$$= -\frac{F_{tot}(r,\theta)}{N}\left(\frac{1+Cb}{\pi C}\right)\left[\int_0^{2\pi}\frac{\sin(\Phi(y,\Phi_0{}'))\,d\Phi_0{}'}{1+2Cu(y,\Phi_0{}')}\right. \quad (86)$$
$$\left. - 2Cd\int_0^{2\pi}\frac{\cos(\Phi(y,\Phi_0{}'))\,d\Phi_0{}'}{1+2Cu(y,\Phi_0{}')}\right]$$

where $F_{tot}(r = r', \theta_s = \theta')$ is the total weighting factor of the charge group corresponding to θ' and r'. N_j is the total number of charge groups.

2.2.6 Structure of the Code

The code for the modified Lagrangian simulator was written using MATLAB. The code was separated into five MATLAB scripts.

Figure 28 shows the flow chart of the code.

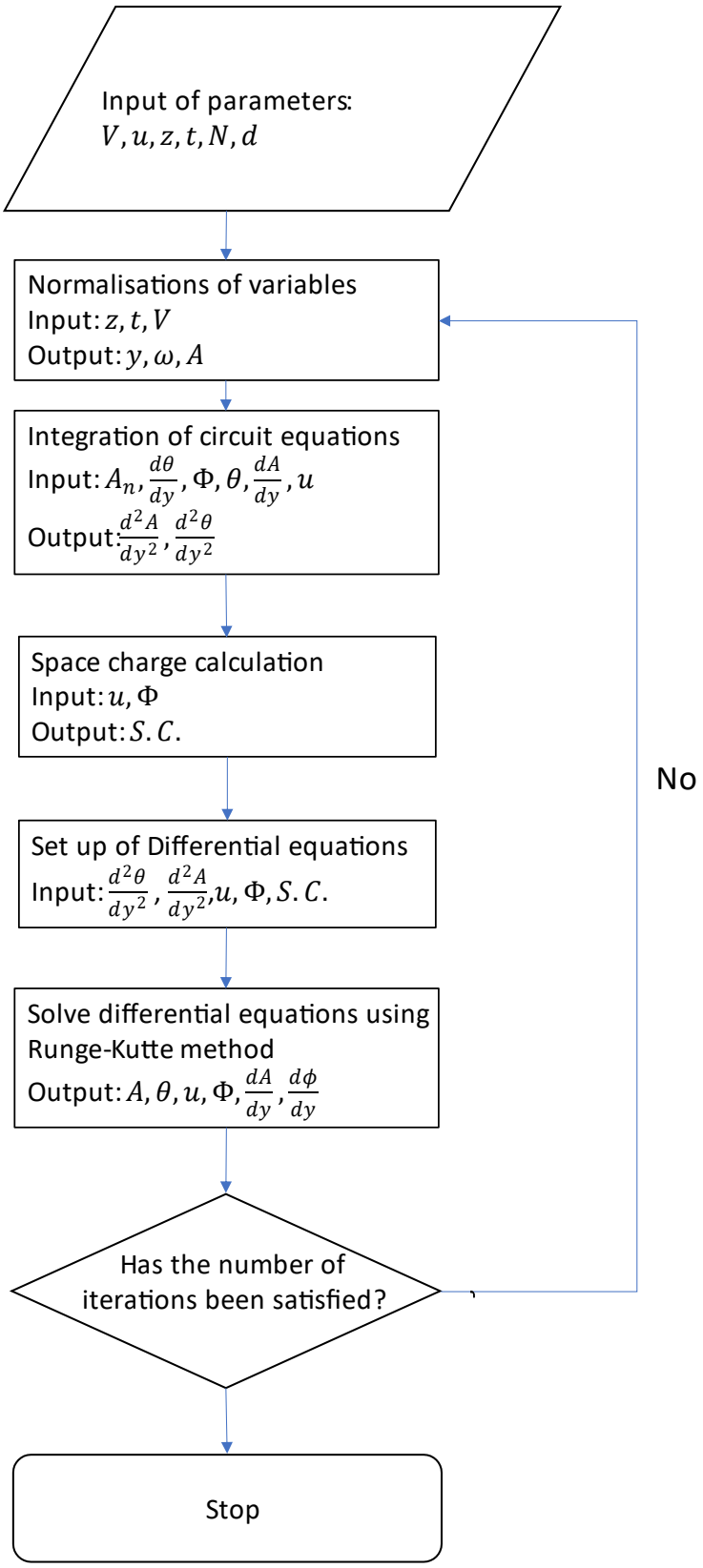

Figure *28* Flow chart of the code

V. Main

The script ‘main’ is where the initial parameters, RF wave conditions and electron beam conditions are defined. This includes the electron beam voltage and current, and the circuit interaction impedance, from which the gain parameter is calculated. The initial phase positions of the electron groups were set as equally distributed over 2π radians. As each initial phase group is split into sub-groups, we call the variable for each group j. The sub-groups are defined by calling each concentric ring n, and each sector m. n and m are chosen from an accuracy and speed of simulation perspective. m and n are chosen to have a good resolution of the varying field. For each group j, all subgroups m and n have the same initial phase, such that

$$\Phi\left(y = 0, \Phi_{0_{j,m,n}}\right) = \Phi_{0_{j,m,n}} = \frac{2\pi j}{N_j} \tag{86}$$

where j = 1,2,...,N_j, and N_j is the total number of entering charge groups. These values are placed in an array the size of the number of charge groups. The initial non-normalized velocity of the charge groups was calculated using the relativistic formula for accelerated electrons

$$u_0 = \sqrt{\frac{(\gamma_r + 1)\eta V_0}{\gamma_r^2}} \tag{87}$$

$$\gamma_r = \left(\frac{\eta V_0}{c^2}\right) + 1 \tag{88}$$

For voltages of order 10^4 V, $\gamma_r \approx 1.02$, which is a small value. This value of velocity is used in the normalisation process of the axial position, along with the gain parameter C and the RF frequency ω. The dy in all the equations is defined from the normalised value of dz, which is the value by which the number of iterations is defined. The length of the interaction period is divided by this

number to calculate the number of steps. This value is generally around 1000 iterative steps. This is because the transmission line equation is a stiff equation, and as such, requires the definition of a maximum integration step to produce a meaningful output. For mm-waves, the Pierce gain parameter is typically of order $10^{-2}\Omega$, the angular frequency of order $10^{12}\,\mathrm{radians/s}$, and the electron velocity associated with the beam voltage is of order $10^{8}\mathrm{m/s}$. These values will vary, but for the structures the code is being tested on, they are correct in terms of order of magnitude. It was found the maximum dy needed to be of order 10^{-2}. When these approximations are inserted into equation (26), we obtain

$$10^{-2} \sim \frac{10^{-2}10^{12}}{10^{8}}\mathrm{dz}$$

Giving

$$\mathrm{dz} \sim 10^{-4}\mathrm{m}$$

When it is considered that a typical mm-wave TWT interaction region, that is, the length inside the tube that the electron beam interacts with the RF wave, is of order $\mathrm{L} = 10^{-1}\mathrm{m}$, then

$$\mathrm{N} = \frac{\mathrm{L}}{\mathrm{dz}} \sim \frac{10^{-1}}{10^{-4}} = 10^{3}$$

Thus, the number of integration steps needs to be of order 10^{3} for stable output. The normalised velocities of the electron bunches defined as zero at the input plane, and as such the initial array for the electron velocities is an array of zeroes the number of charge groups in size, exactly like the initial phase positions of the charge groups.

The initial value for the normalised wave amplitude, $\mathrm{A(y)}$, is calculated using the power equation for the power at each plane.

$$P_w(y) = 2CI_0V_0A^2(y)\frac{1 - C\frac{d\theta(y)}{dy}}{1 + Cb} \tag{89}$$

where $P_w(y)$, the power of the wave, is measured in Watts.

$$\frac{d\theta}{dy}|_{y=0} = -b \tag{90}$$

and as such, the calculation for $A(0)$ becomes

$$A(0) = \sqrt{\frac{P_w(0)}{CI_0V_0}} \tag{91}$$

The initial rate of change of A(y) is

$$\frac{dA}{dy}|_{y=0} = -A(0)(1 + Cb)d \tag{92}$$

The initial value of $\theta(0) = 0$. These are all the values required for solving this set of equations using an initial value problem approach.

These values are now placed into an array consisting of $4+2N_{jt}$ elements, the first four being $A(y = 0), \frac{dA(y=0)}{dy}, \theta(y = 0)$ and $\frac{d\theta(y=0)}{dy}$,the next N_{j_T} being the initial normalised velocities, and the last N_{j_T} being the initial phases of each charge group. These values are used as the initial values for integrations. The plasma frequency reduction factors and weighting functions are also input in this script.

VI. Initialisation

The initial values are placed into an array. As before:

$$\left(\frac{\partial A}{\partial y}|_{y=0},\ \ A(0),\ \ \frac{\partial \theta}{\partial y}|_{y=0},\ \ \theta(0),\ \ u(\phi(0,\phi_1))\ \ \cdots\ \ u(\phi(0,\phi_N)),\ \ \phi(0,\phi_1)\ \ \cdots\ \ \phi(0,\phi_N)\right)$$

Additional rows are added per iteration of the solver, which allows for the study of the evolution of the interaction.

VII. Circuit Equation Integral Solver

The values of the integrals in the circuit equations (42) and (43) are calculated using the composite Simpson's Rule [67], which is

$$\int_a^b f(x)dx \approx \frac{h}{3}\left[f(x_0) + 2\sum_{j=1}^{\frac{n}{2}-1} f(x_{2j}) + 2\sum_{j=1}^{\frac{n}{2}} f(x_{2j-1}) + f(x_n)\right] \quad (93)$$

For our purposes, $a = 0$, and $b = 2\pi$, and each x value is the phase position of the n^{th} charge group. The range is $0 < \phi < 2\pi$ because in the nonlinear region of the solution, before bunching occurs, that is approximately the spread of the values of the phases of the charge groups (and is exactly that at the input plane). This solution leaves two second order differential equation to be solved. Equation (84), the equation for the position of the charge group in the signal, is also solved and implemented in this script. The solution then uses a look up table to find the appropriate axial weighting function for the charge group. This is multiplied with the appropriate radial weighing function and then with the circuit equation. This accounts for the position of the charge group in the electromagnetic wave.

VIII. Space Charge Solver

The axial force equation has a space charge component E_{sc-z}, which is solved using equation (46), using the values calculated from the plasma frequency reduction factors in Main.

IX. Differential Equation Solver

The axial force equation (47) and the Velocity Phase equation (48) are differential equations whose solutions find the next values for the normalised axial velocity and phase position, for each charge group, respectively. They are first order differential equations.

The circuit equation differential equations are second order differential equations for the normalised RF wave amplitude and phase angle between the RF wave and the hypothetical wave travelling at u_0. These and the axial force equation and the Velocity-Phase equation can be solved by implementing the Fourth-order Runga-Kutta method, which is given by

$$\begin{aligned} k_1 &= hf_1(x_n, y_n) \\ k_2 &= hf(x_n + \frac{1}{2}h, y_n + \frac{1}{2}k_1) \\ k_2 &= hf(x_n + \frac{1}{2}h, y_n + \frac{1}{2}k_2) \\ k_4 &= hf(x_n + h, y_n + k_3) \\ y_{n+1} &= y_n + \frac{1}{6}k_1 + \frac{1}{3}k_2 + \frac{1}{3}k_3 + \frac{1}{6}k_4 \end{aligned} \tag{94}$$

For the first order equations, the Velocity Phase equation and the Axial Force equation, the routine housing the method is used once per charge group per iteration, giving a new phase position and axial velocity for each charge group. For the second order differential equations, the method is run twice each. The second order equation in $A(y)$ is solved for $\frac{dA(y)}{dy}$, and this output is saved. Using this value, the method is used again to produce $A(y)$. The same process is used with the second order differential equation in $\theta(y)$.

The new values of the phase positions, charge group velocities, the rate of change of the RF voltage amplitude, the RF voltage amplitude, the rate of change of the phase angle and the phase angle are all saved at the new initial values, and the process is run again, until the defined number of steps has been reached.

X. Output Analysis

After the desired number of iterations has been reached, an array is generated with $4 + \mathrm{N_{j_T}}$ columns and N rows, where N is the number of iterations, which corresponds to the number of planes along the TWT at which calculations were made and output. This allows analysis of how the charge groups interact with the RF wave and with each other.

The more interesting features include the bunching phenomena along the structure, that is, how the charge groups interact around saturation point, and the increase in power of the RF wave.

2.3 Results

Following are the results of found from testing the code against the results of full 3D simulator CST. Discussed will be the output power and saturation point of the signal and the interaction, the energies of the electron groups and the trajectories in phase of the electron groups. The code was run on a PC with 3.50 GHz processor speed and 16.0 GB of RAM. The simulation used 31 charge groups, each with 100 sub charge groups. This amount of charge groups and sub charge groups was chosen because it found to be a good

balance between fast simulation time and accuracy at the centre of the band of frequencies considered.

2.3.1 Validation: Ka-Band DCW TWT – 34 GHz

The code was tested in its accuracy by comparing the output power, gain and saturation point against a simulation of a DCW for a Ka-Band DCW TWT in literature [65] at 34 GHz. Table 1 shows the input parameters.

Table 1 Input Parameters *[65]*

f	Frequency	32-38 GHz
$\boldsymbol{\beta}$	Propagation Constant	Varies as a function of frequency
d_l	Loss	0.01729 dB/period
P	Input Power	20 dBm
V	Voltage	10880 V
I	Current	0.2 A
$\mathbf{Z_0}$	Interaction Impedance	Varies
L	Length of Tube	35 cm
N	Integration Number	1400
$\mathbf{W_r}$	Weighting factors (radial and angular)	Varies
F	Axial Weighting Factors	Varies

The tube length is about 25 cm, however 35 cm of interaction length is simulated to explore more of the interaction.

The eigenmode simulations of this structure showed a synchronous beam voltage of 10.93 kV. The beam voltage used in the PIC simulations was about 12 kV, and the beam voltage used in the Lagrangian simulation was 10.9 kV. This is less than the synchronous beam voltage of the eigenmode simulation, and less than the beam voltage used in the CST PIC simulation. The beam voltages of the different programs are shown in Table 2. The values are different because due to differences in how the beam interacts and modifies the field in the hot simulation compared to the cold simulation.

Table *2* Operational Voltage comparison

Parameter	CST (Eigenmode)	CST(PIC)	Modified Lagrangian
Voltage/V	10930	12000	10880

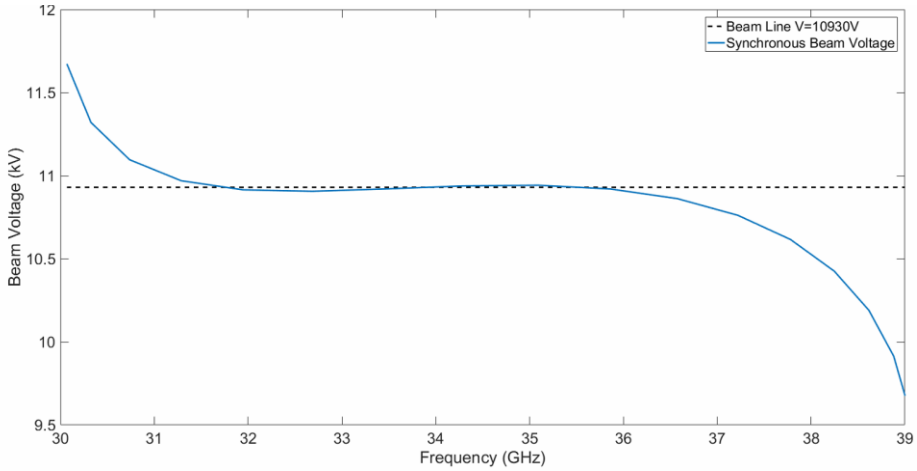

Figure 29 Ka-Band DCW dispersion curve and beam line

The synchronous beam and the interaction impedances across the band are shown in Figure 29 and Figure 30 respectively.

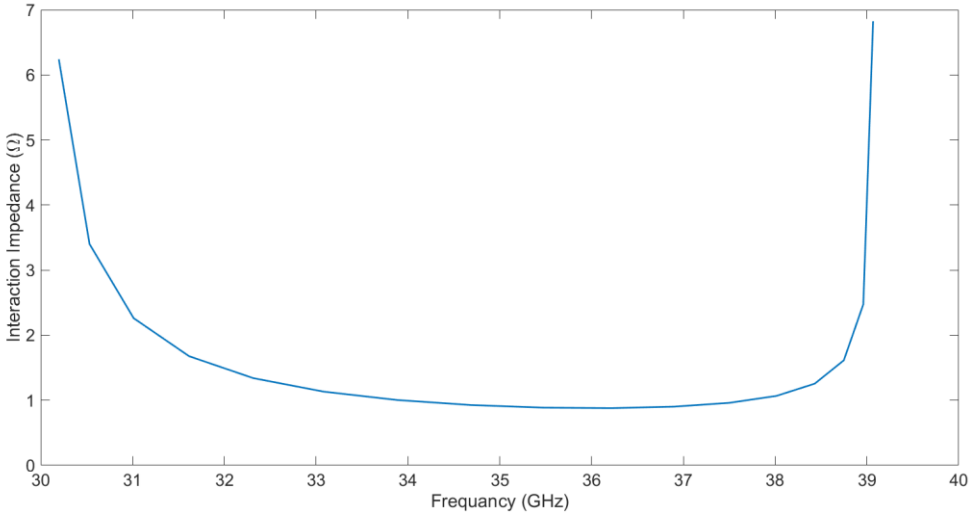

Figure *30* Ka-Band DCW Average Interaction Impedance. The interaction impedance is averaged over the volume of the electron beam in one period of the DCW. The beam is considered to be a perfect cylinder

2.3.2 Convergence

A convergence study was performed and it was found that 31 charge groups found a balance between accuracy and time. Figure 32 shows how the time of the simulation increased with the number of simulations, and Figure 31 shows

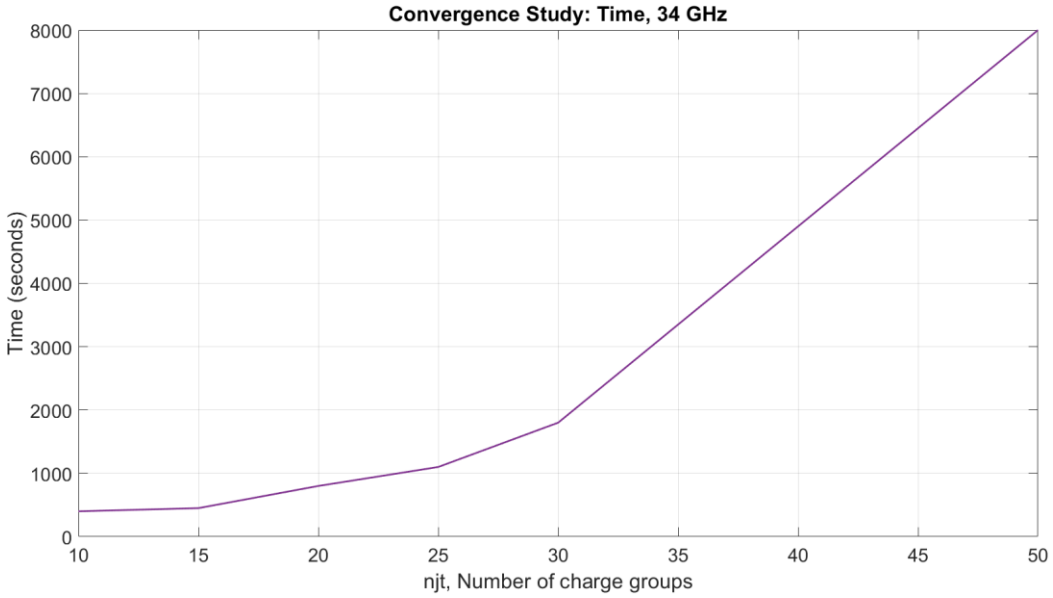

Figure 32 The time of the simulation as a function of number of charge groups, njt.

how the peak power of the wave varied with the number of charge groups. The

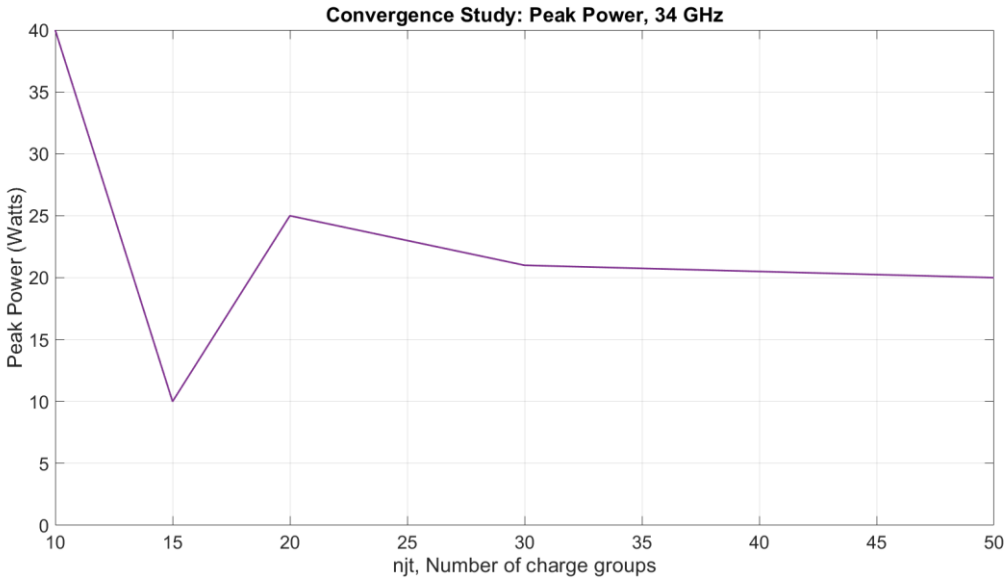

Figure 31 The peak output power, as a function of number of charge groups, njt.

frequency used for the study was the central frequency, 34 GHz. 10x10 subcharge groups were chosen to capture enough of the variance of the field radial and axially in the DCW.

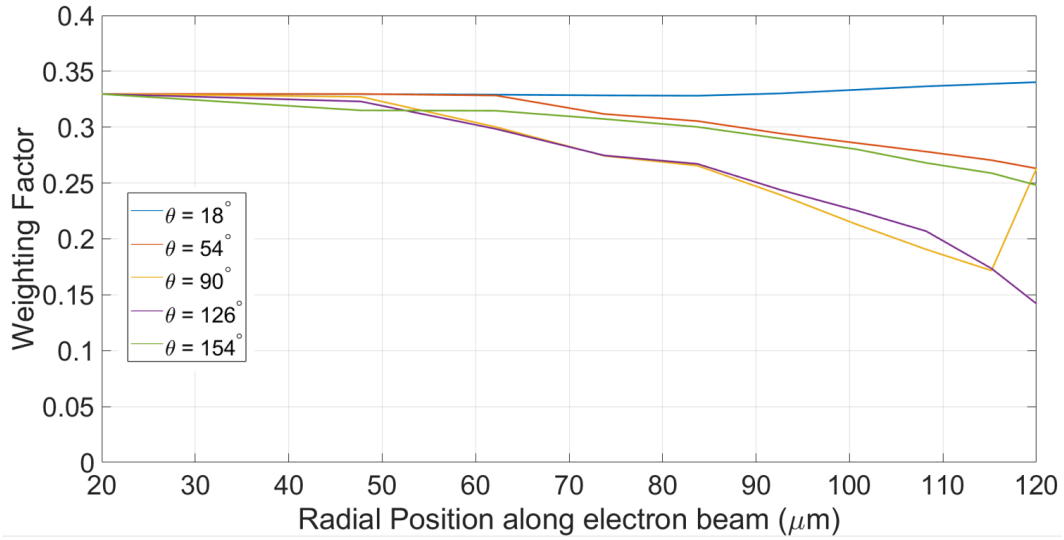

(a)

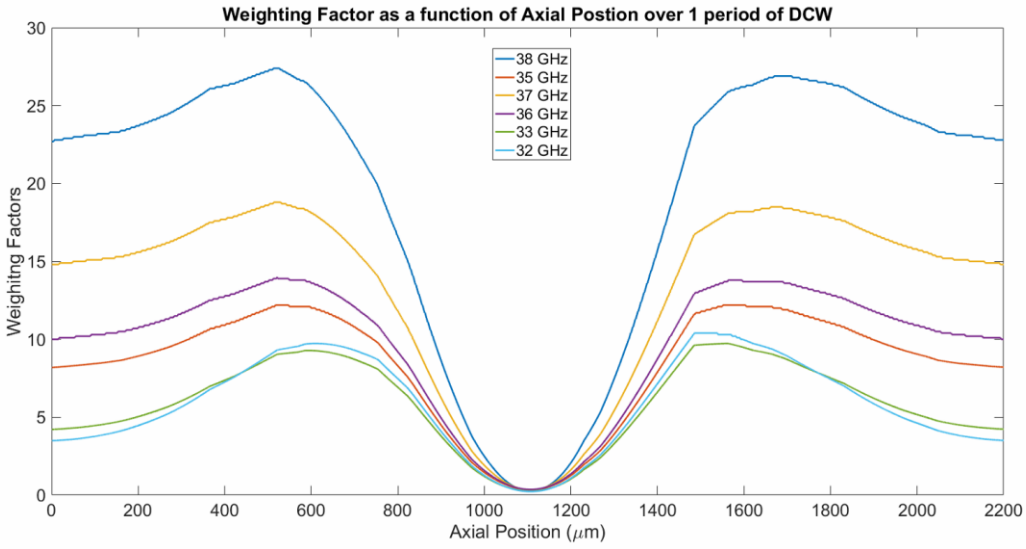

(b)

Figure *33* Radial (a) and axial (b) Weighting factors

2.3.3 Weighting Functions: Results

The radial weighting function and axial weighting functions were calculated via CST eigenmode simulator. Figure 33 (a) shows the radial weighting functions, as a function of angular position about the beam axis. Only the first five are shown as the system, is symmetric when mirrored. The position starts at $20\mu m$ because this is the centre of the first radially defined charge group. θ and the radial position are defined in Figure 20. Figure 33 (b) shows the axial weighting functions. The weighting function is very small in between the pillars. This is because the field is squeezed out of the space between the pillars. The weighting functions also vary large outside the pillars. These large differences in value are because the field varies significantly along the period.

2.3.4 Energy of each charge group

The energy of each charge group is shown in keV, as a function of axial position along the tube. At the start of the tube, the energy of each electron is the same,

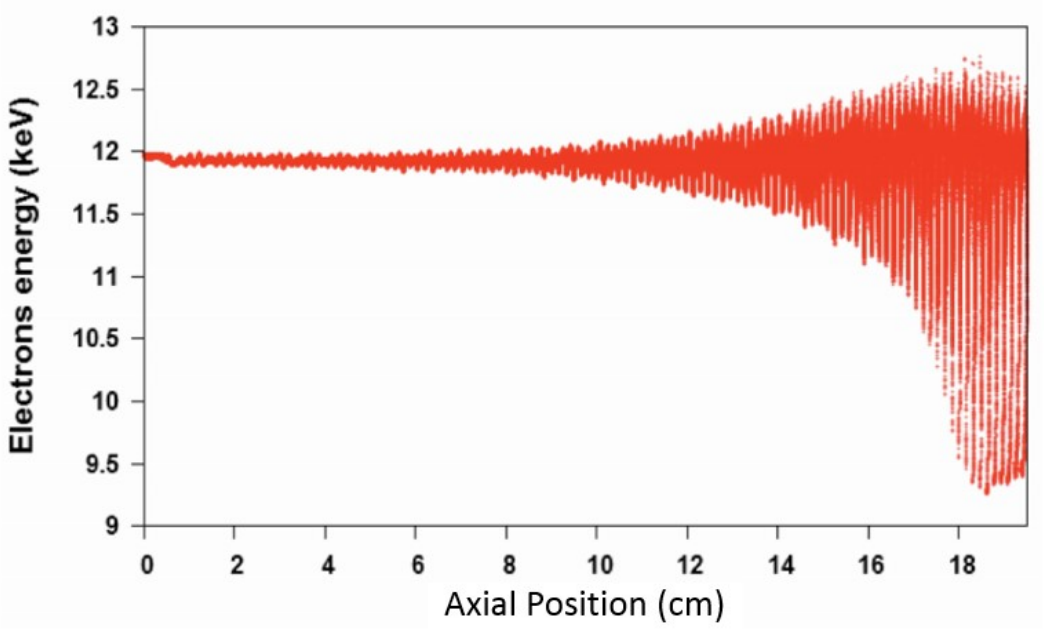

Figure *34* Electron energy from CST, in keV *[65]*

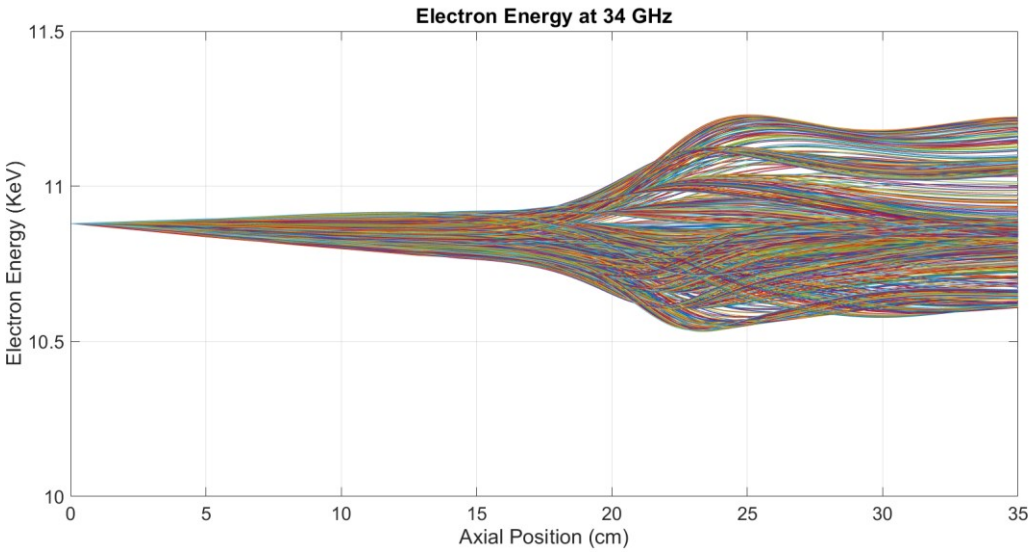

Figure *35* Charge group energies as a function of axial position

as the voltage of the cathode is constant. As the electrons interact with the RF signal and each other, they lose or gain energy.

The difference in initial electron energy is seen. Figure 34 is the electron energy as calculated by CST-PS. Figure 35 is calculated by the modified Lagrangian model. In Figure 34, each point is the energy of a charge group at that axial position. As the group moves forward along the tube, it gains or loses energy. In Figure 35, each curve is a charge group, and in the same way, it loses or gains energy as it moves along the tube. Each curve follows the change in energy of an individual charge group. The largest decrease in energy is shown at between 18cm and 20cm in the CST-PS evaluation, whereas the largest decrease in energy as calculated by the modified code is at 20cm to 25cm.

2.3.5 Electron phase positions

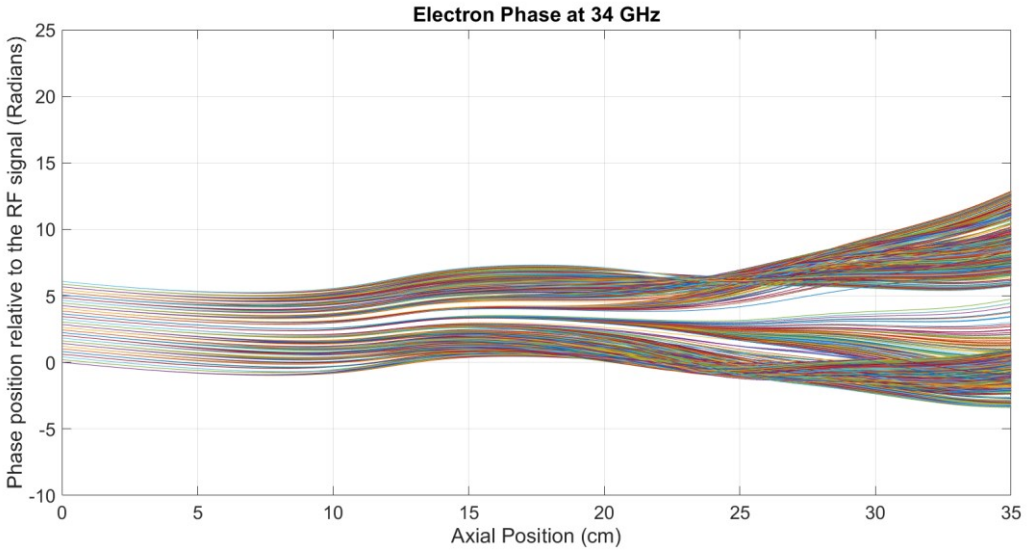

Figure *36* Charge group phases as a function of axial position

The phase positions of each charge group are shown in Figure 36. It can be seen that the sub charge groups with identical initial phase position spread out, due to the difference in plasma frequency reduction factors and strength of interaction with the field. This is because of different distances to the wall of the tube, and different field intensities felt by the beam and a function of angular position, respectively. Strong bunching is defined as where the trajectories are close. Again, the strongest bunching occurs between 20cm and 25cm. This is seen in the density of the trajectories of the charge groups.

2.3.6 Saturation Point

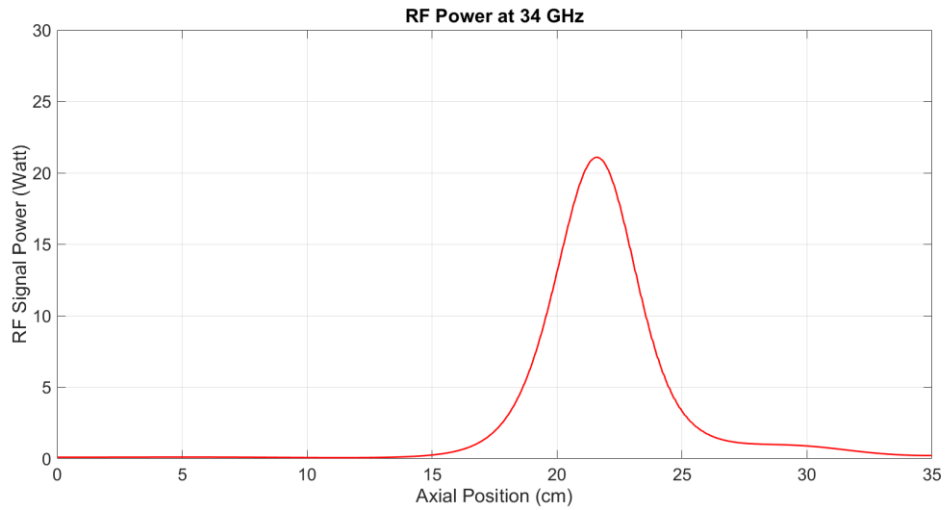

Figure *37* Power output, P_w, signal as a function of the axial postion in the interaction region

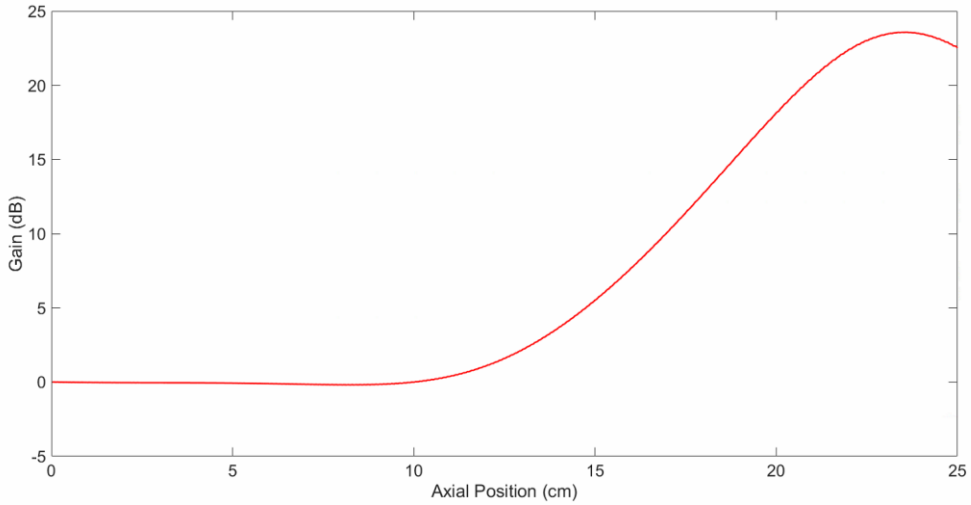

Figure *38* Gain of the signal as a function of the axial postion in the interaction region

Figure 37 and Figure 38 show the gain and the power output for the structure at 34 GHz. The max power output is around 20 cm. This corresponds to where along the tube the energy loss was greatest as shown in Figure 35 and the bunching shown in Figure 36 The output power matches very closely to that of the PIC simulations. This can be seen in Figure 34. The largest dip in energy of the electrons corresponds to the saturation point, at about 20 cm.

2.4 Results over the bandwidth

Presented below the different parameters over the bandwidth 32-38 GHz. The model accurately describes the interaction and agrees well with the 3D simulators across the middle and upper end of the bandwidth. However, the model fails to properly describe the interaction at the low end of the bandwidth, at around 32 GHz, where the gain becomes much lower than predicted by the full 3D simulator, before growing large near 30 cm of interaction length. This is because the difference in phase velocity of the RF signal and the electron velocity becomes too great. The gain will be from the interaction impedance being greater at the edge of the band. This is also true of the upper part of the band. The electron beam is much faster than the wave, and the interaction impedance is large.

In the model, the electron beam is confined to initial radii. If the electrons were allowed more degrees of freedom, the gain may be reduced in the edge regions of the band, and the saturation point more in line with the PIC simulation.

2.4.1 Weighting Factors

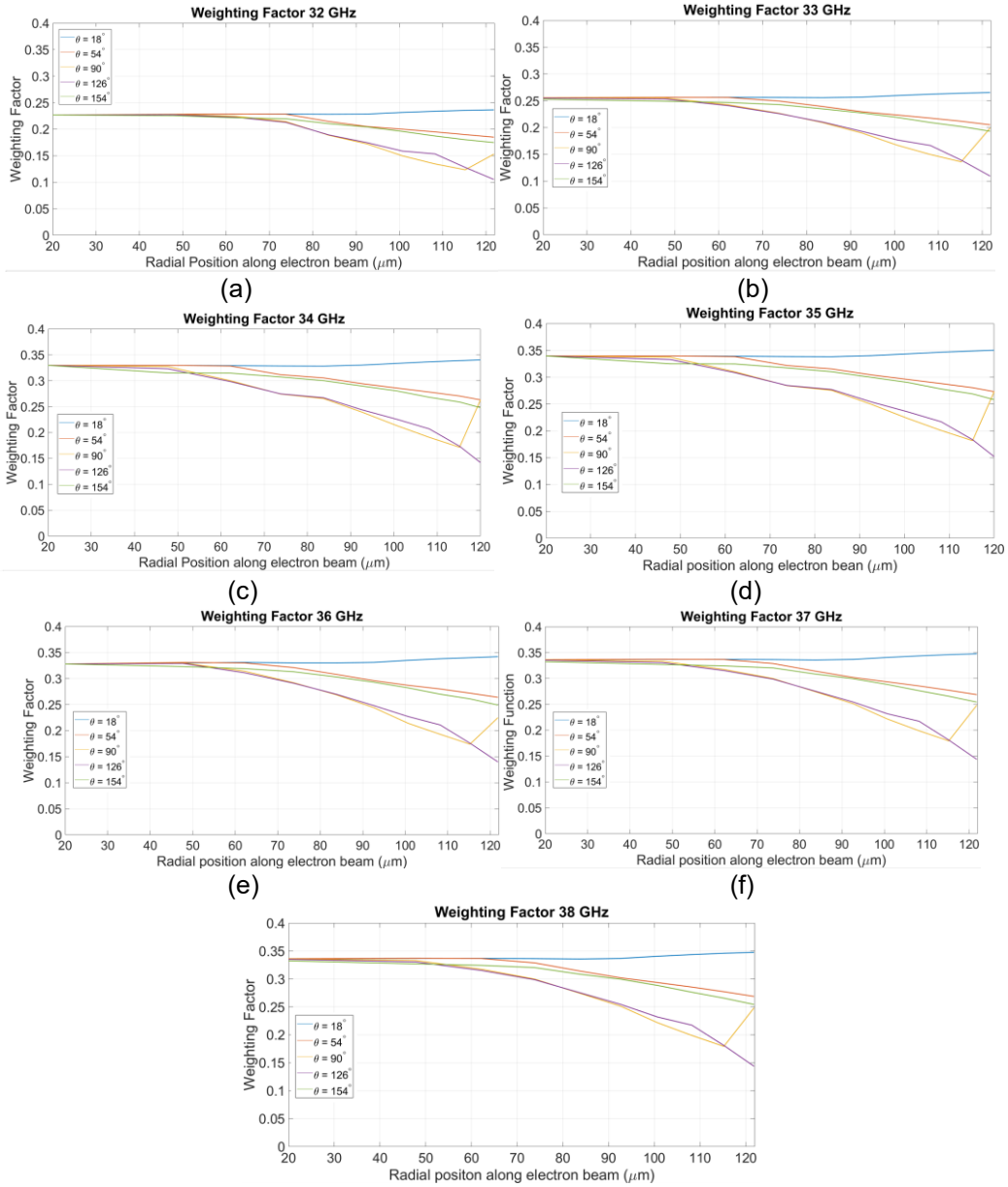

Figure *39* Radial weighting functions vs radial position per frequency

Figure 39 show the radial weighting functions and the axial weighting functions of the ka-band DCW respectively. The axial weighting functions are shown in Figure 33 (b).

The radial weighting functions as expected lose strength away from the centre of the beam. Also, as expected for a rotational asymmetric SWS, the weighting

factors decrease at different rates, as a function of the angle about the beam axis. This is because of how the field varies near the copper in the structure. The field near the pillars is lower than in the centre of the structure. The weighting factors near the edge of the lower edge of the band, Figure 39 (a) and (b) have the lowest weighting factors. The weighting factors increase with frequency, as seen in Figure 39 (c), (d), (e), (f), and (g). This is also true with the axial weighting factors. The axial weighting functions have very small values in the centre of the period, and large values outside of the pillars.

2.4.2 Electron Energy

The electron energy can be seen in Figure 40 as functions of axial position. Figure 40(a), at the edge of the band, shows little interaction until the 30 cm of interaction, where there is suddenly a lot of interaction. Figure 40 (b) shows more interaction with the signal. In the centre of the band, Figure 40 (c), (d), (e), and (f), show signficant interaction with the signal. There is a distinct drop in average electron energy at around 20 cm along the interaction, where more

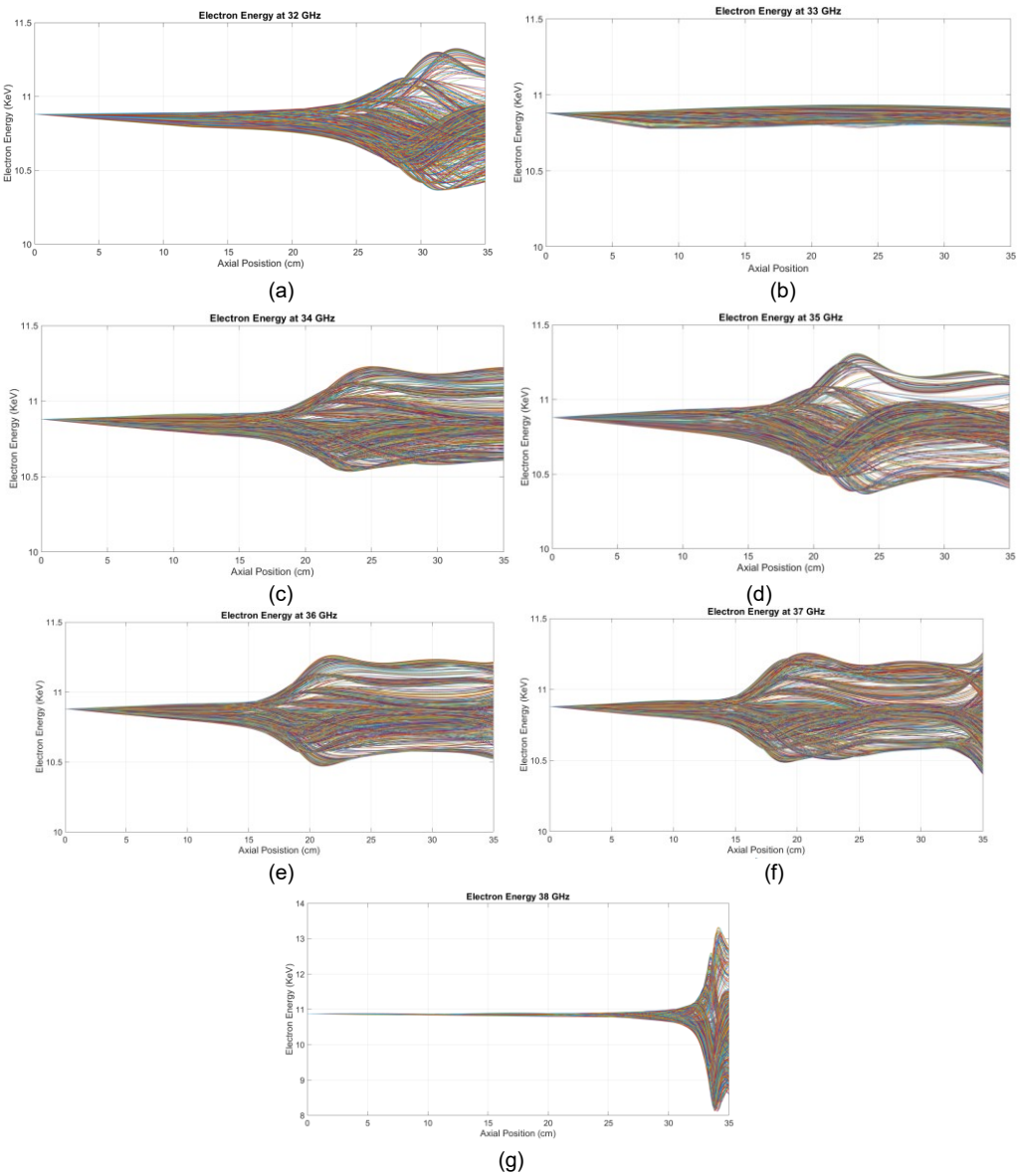

Figure *40* The electronic charge group energies as functions of axial postion for each signal frequency. The y-axis of (g) is greater beace much more energy is lost by the electrons.

electrons lose energy than gain energy. Figure 40(g) shows very little interaction until a very large drop in energy at about 30-35 cm. Figure 39 (b) shows little interaction but still achieves gain. This may be because although the dip in energy of the electrons is less, the rise in energy seen in the other interactions is also less. This means less energy is removed from the wave, and allows gain.

2.4.3 Electron Trajectories

Figure 41 shows in the centre of the band, bunching occurring, around the 20 cm distance, which again coincides with the distance at which most of the

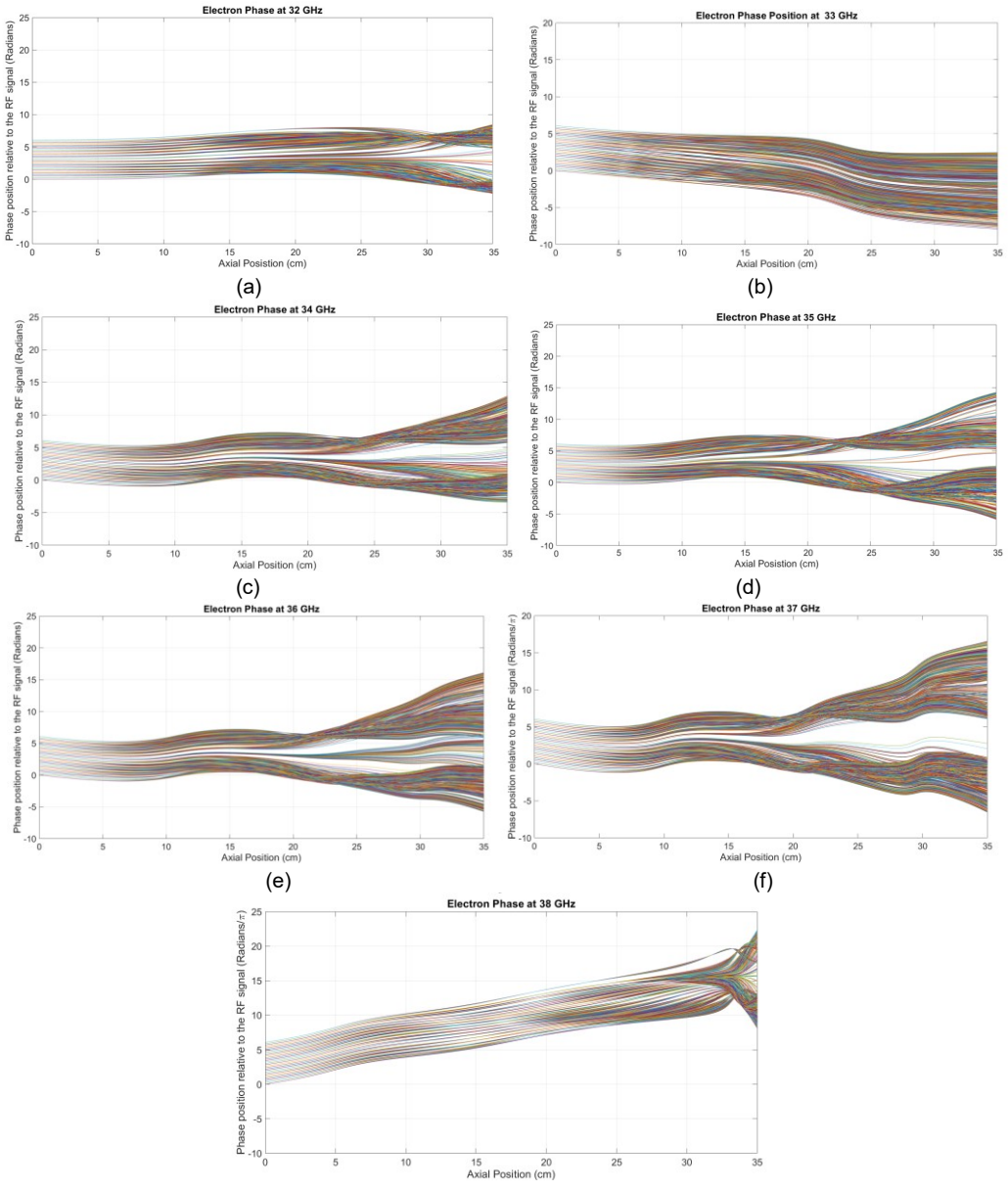

Figure *41* Trajectories of the charge groups expressed in terms of phase position relative to the RF signal

power is transferred between the signal and electron beam. After this bunching the beam spreads.

The bunching is shown by how close the trajectories of the electronic charge groups are. The closer they are in phase, shown on the y-axis, for a given value of axial position, shown on the x-axis, the more “bunched” the charge groups are at that position. Conversely, where the trajectories are far apart is where anti-bunches occur. In Figure 41(a) it is seen that there is little bunching of the electrons until around 30-35 cm. This is shown by how the electron trajectories are not seen to become significantly close together until around 30-35 cm. However, in Figure 41(b), (c), (d), (e), and (f), there is considerable crossing and closeness of the electron trajectories near the 20-25 cm region. This means there is significant bunching of the electronic charge groups, allowing for energy to be transferred from the electrons to the RF signal around the 20-25 cm region. This coincides with the large dip in average electron energy seen in the previous subsection.

2.4.4 Saturation Point

The saturation points are shown in Figure 42. Saturation is when the RF electric field power has reached its maximum, and further operation will cause a decrease in wave energy, with the energy being lost to the electron beam. This is seen in the graphs as the output power reaching a maximum and then decreasing.

In Figure 42 (a), it is seen that there is little power being transferred to the RF signal by the 20 cm axial position. However, later along the tube there is a large amount of power being transferred from the beam to the signal compared to the frequencies in the centre of the band. In Figure 42(b) power is being successfully transferred but not as much as in Figure 42 (c), (d), (e), or (f).

These graphs show that significant power is being transferred from the electrons to the RF signal. This is consistent with the electron energies and the electron trajectories shown previously in Figure 40 and Figure 41. The saturation point occurs at about 20 cm. Figure 40 (g) shows a power output two orders of magnitude greater than in the centre of the band.

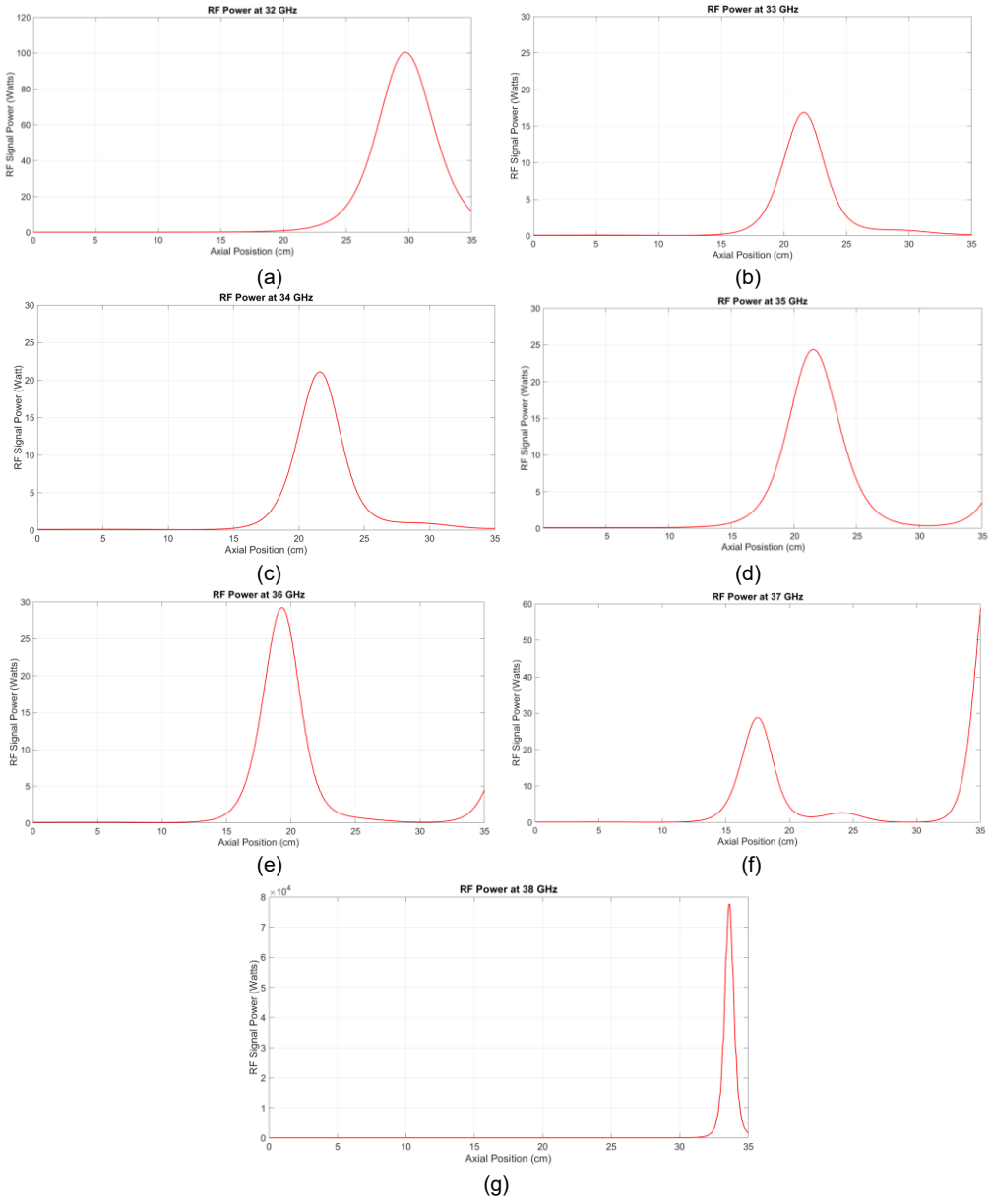

Figure *42* Power output as calculated by the modified Lagrangian code per frequency

2.4.5 Gain and Power across the Bandwidth

Figure 43 and Figure 44 show the gain and the output power as functions of frequency for the 3D electromagnetic simulator CST and the modified Lagrangian code. The choice of output power for each frequency is chosen by the interaction length equal to the maximum output power of the 34 GHz simulation, at just over 34 GHz This is to mimic the tube being optimised for 34 GHz, and then the output power of the other frequencies following that. As can be seen, there is good agreement over most of the band, except for the edges

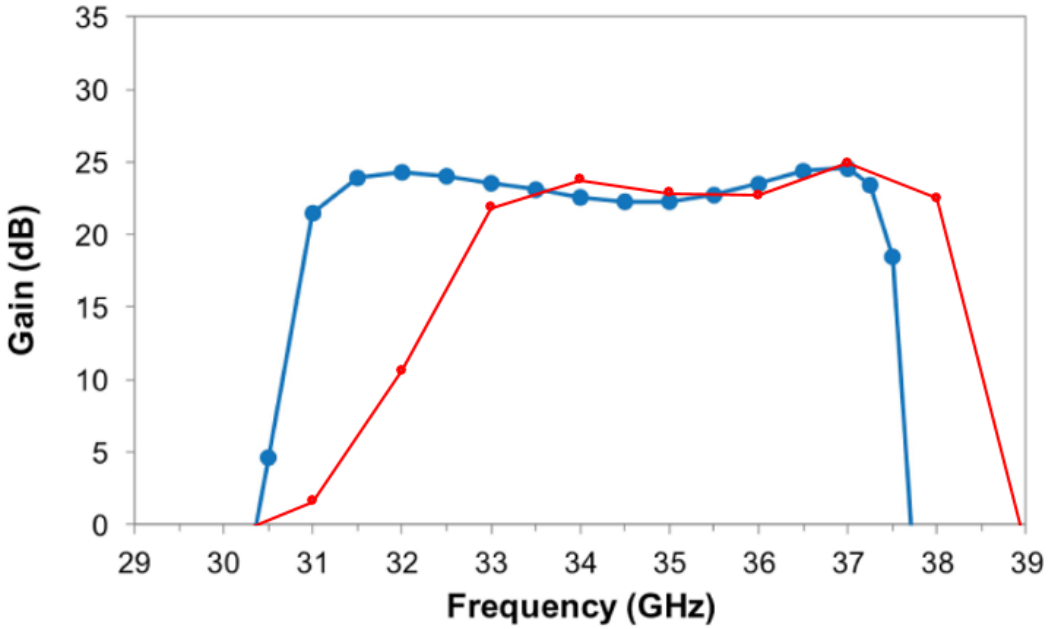

Figure *43* The gain of the tube as a function of signal frequency as calculated by CST (blue) and the modified Lagrangian code (red)

of the band, which seem to be shifted by approximately 1 GHz up in frequency. This is likely because of beam loading. When the electron beam enters the tube, so does its electric field. This field modifies the field established by the wave. This is captured by the simulation performed by CST-PS. However, it is not captured by the modified Lagrangian code.

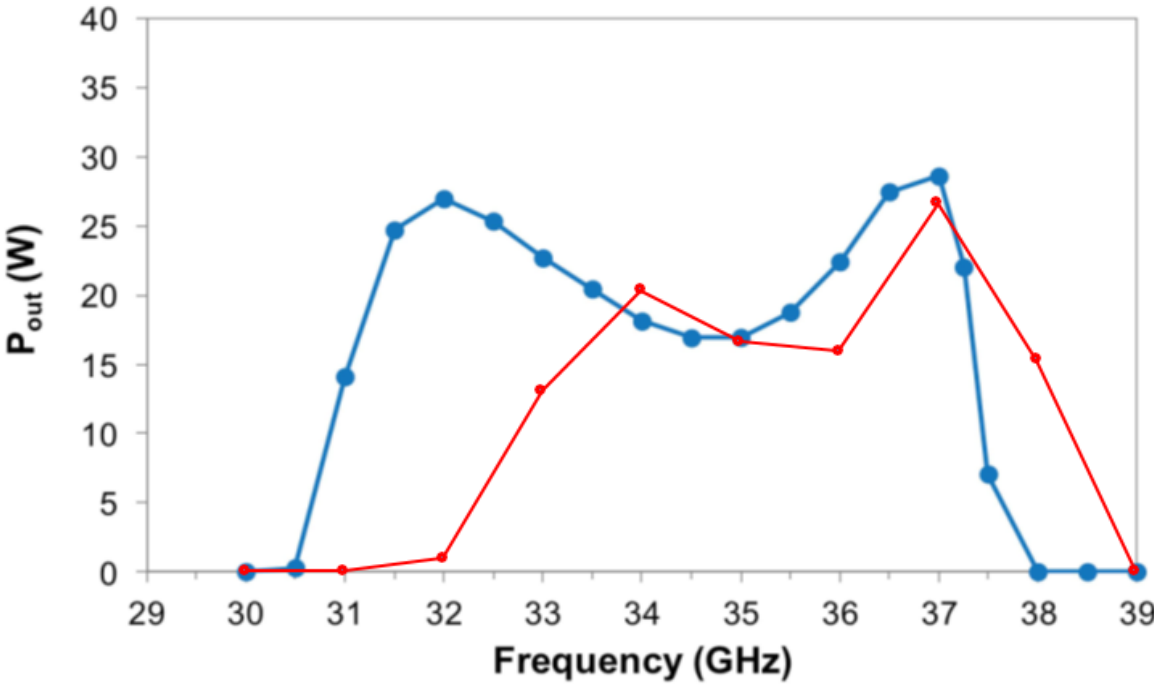

Figure *44* The power output of the tube as a function of signal frequency as calculated by CST (blue) and the modified Lagrangian code (red). The interaction length considered for the Langrangian code was 20cm

2.5 Simulation Time

Function Name	Calls	**Total Time**	Self Time*	Total Time Plot (dark band = self time)
rungekuttause1	2	1842.984 s	287.522 s	
rk4	2	1555.396 s	6.948 s	
rungekuttause1>f	8000	1548.449 s	239.127 s	
spacecharge2	24800000	1243.201 s	1243.201 s	
main	2	1212.562 s	1.556 s	
circuitegn	8000	66.120 s	42.211 s	

Figure *45* The amount of time for one run of the Lagrangian simulator, at single frequency

Figure 45 shows how long the simulation ran before completion. Approximately

1800s (half of one hour) per frequency. This is much faster than 3D simulators,

which may take many hours per simulation, but much slower than the unmodified version of the model, which takes seconds for single simulations. This is slower as with the additional space charge and weighting function calculations, along with using 3100 subcharge groups, the number of calculations per integration step has been increased. Including the time for the eigenmode simulation, and the Lagrangian simulations, the simulation time across the band was 4-5 hours.

2.6 Conclusions

In this chapter, the Lagrangian code [50] designed for the helix SWS was modified for use in the simulation of SWS with irrotational symmetry. This was done by introducing a new model for the space charge forces and a method for producing weighting functions.

The code was verified by comparing its results with the results of full 3D simulator CST [59], simulating a Ka-band DCW TWT [65]. A workstation with 3.50 GHz processor speed and 16.0 GB of RAM was used. The simulation used 31 charge groups, each with 100 sub charge groups.

A convergence study was performed and it was found that good accuracy was found at 31 charge groups, when taking in to account the simulation time, which was rapidly increasing as more charge groups were added.

Shown in Figure 40, Figure 41, and Figure 42 are the saturation points. They show that for the middle and upper range of the bandwidth, the saturation points were accurately simulated for a value of about 20 cm. Figure 40 shows where the average energies of the charge groups decreases, Figure 41 shows where the bunching is seen, and Figure 42 shows where the RF power maximises.

The max RF power is shown to be between 15-25 Watts. This agrees with the 3D simulator.

However, in the lower part of the band, the code fails to capture the expected power and saturation point. As shown in in Figure 42, however, the RF power does become very large past the 30 cm interaction length of the code. The same is true of the upper part of the band 38 GHz. Past 30 cm interaction length the output power become very large.

The lower accuracy at low frequency could be due to the difference in wave phase velocity and electron velocity, where the difference between the two in the lower half of the band becomes too great.

The extreme upper band also had little interaction in the first 30 cm of interaction length. After this, the wave is amplified by a very large amount, of the order of 10^4 Watts. This may be due to the large interaction impedance at the edge of the band, and the beam being much faster than the signal in this range.

The simulation time for the modified code is about 1800 seconds for a single frequency, shown in Figure 45. The eigenmode simulation, where the data for the weighting functions is extracted, takes a similar amount of time to run, at about 1800s. The combination of time is still much faster than the 3D simulator on the same machine, where a single frequency PIC simulation would take tens of hours. However, this time is much slower than for the unmodified code, which can take seconds per frequency. This can be attributed to the space charge calculations and the calculation of each charge groups position in the field, as well as the code using 3100 charge groups.

In conclusion, the code has been tested for the Ka-band DCW. It showed to accurately describe the beam-wave interaction for the middle and upper range

of the band but is not accurate at the lower band. The difference in the lower half of the band becomes too great. To overcome this, it may be necessary to rederive the equations in a higher dimension, to capture some of the gain which may be missing due to limitations in this model. This could include angular motion and radial motion of the sub charge groups.

Chapter 3 3D Design of DCW for millimetre wave TWTs

The second part of the thesis is the design of double corrugated waveguides and related couplers for millimetre waves TWT and BWOs. The simulations are:

- A comparison of couplers of DCW for a 346 GHz BWO. The couplers considered are lateral tapering and height tapering of the pillars of the DCW;
- A DCW for a100 GHz BWO using lateral tapering;
- A DCW for a 270 GHz TWT using lateral tapering;
- A DCW for a W-band TWT using triangular pillars;
- A DCW for a W-band TWT using square pillars with a taper using height tapering of the pillars;
- A comparison of “straight” tapering and “bend” taper configuration for the DCW using the W-band TWT.

The design process for the DCW TWT begins with the beam parameters. These are the beam voltage, beam current and beam diameter.

The beam diameter defines the minimum distance between the pillars, and the beam diameter and current, and the beam voltage, define the requirements for the confining magnetic field provided by a periodic permanent magnet (PPM). The parameters of the DCW are shown in Figure 46 and Figure 47. These must be highly optimised to meet the tube requirements. This was achieved by small variations in the parameters of the periodic structure, like modifying the period or the pillar dimensions, and comparing the eigenmode simulations to find the optimal periodic structure in terms of synchronous beam voltage and interaction impedance.

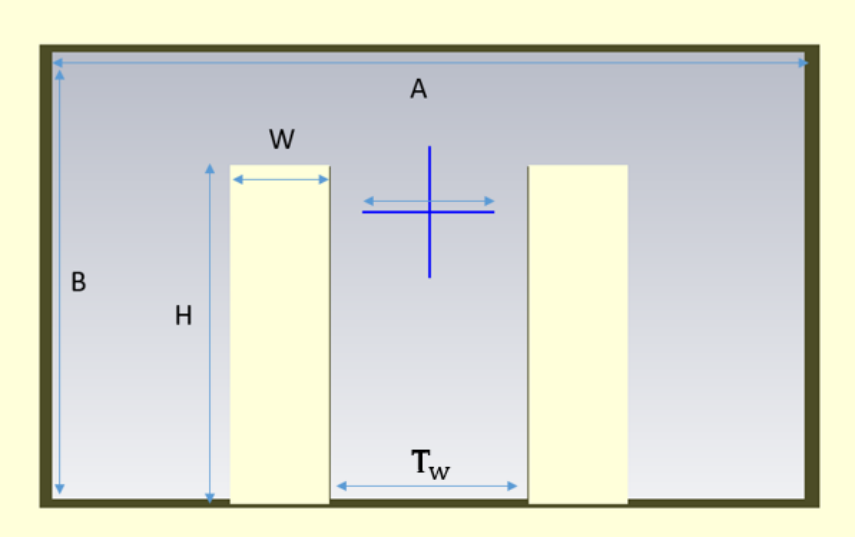

Figure *46* Front view of the period of the DCW

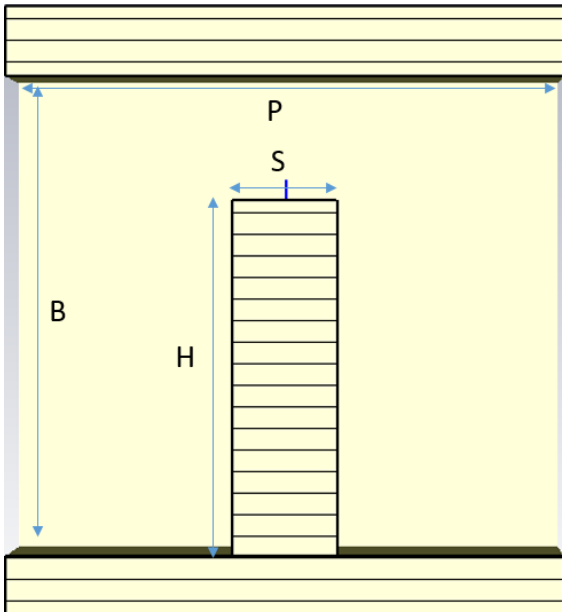

Figure *47* Side view of the period of the DCW

3.1 Eigenmode Simulations

The eigenmode simulations for the design of the SWS uses one period of the structure and produce a dispersion curve, interaction impedance and loss. The eigenmode of a given closed-region possess eigenmodes corresponding to frequency and phase difference. The simulation considers a closed region in

the form of a single period of the SWS being designed. The frequencies of the dispersion curve correspond to allowed values of the propagation constant as a function of the range of phase differences being investigated [60].

For the forward wave operation of the DCW, phases of $2\pi < \phi < 3\pi$ are utilised, and for the first negative harmonic, phase of $\pi < \phi < 2\pi$ are utilised. This is because, for the DCW, as the frequency increases, the beam-wave interaction at the fundamental harmonic becomes demanding technologically. This is because the beam voltage becomes very large in the fundamental harmonic. This is an issue if a compact power supply is required [68].

The interaction impedance, phase velocity of the RF wave, all as functions of frequency or phase difference can be found using the dispersion curve and power flow. A value of loss relating to the conductivity of the material being used may be calculated. The skin depth of the copper, the material considered as for the structure, constrains the acceptable surface roughness of the copper

Table 3 Difference in conductivity between pure copper and the modelling of copper with finite surface roughness [33]

Cu Conductivity	Cu Conductivity (Reduced with surface roughness $\approx 0.1\ \mu m$)
$5.8 \times 10^7\ S/m$	$1.8 \times 10^7\ S/m$

after machining. This can be modelled by using a reduced conductivity.

In the simulations described, the material is oxygen free high conductivity copper. Shown in Table 3 are the different conductivities. A conservative value of $1.8 \times 10^7\ \mathrm{S/m}$ was used, from an assumed surface roughness of about $0.1\ \mu\mathrm{m}$.

It often occurs that a change to the geometry of the structure, which realises a positive change in the interaction impedance, results in a negative change in the dispersion relation or the synchronous beam voltage. As shown in Figure 48, varying the waveguide width can increase the interaction impedance

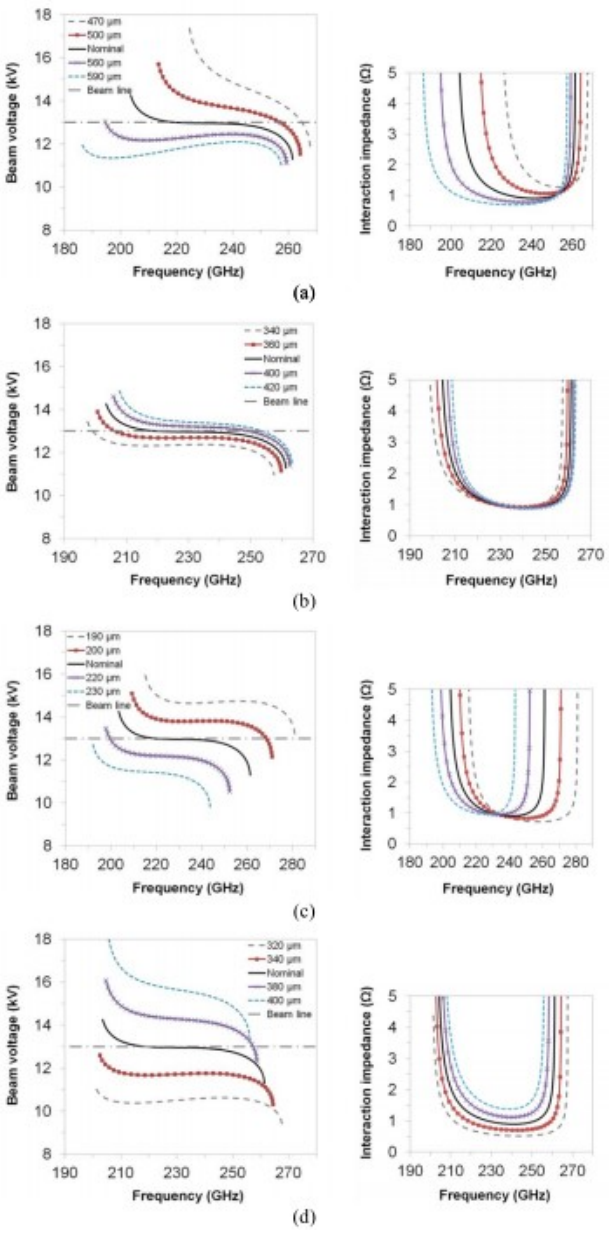

Figure *48* Study on the synchronous beam voltage and interaction impedance for variations in parameters of the DCW. (a) Waveguide width, (b) Waveguide height, (c) Pillar height, (d) Period. *[23]*

significantly, at the cost of the dispersion relation changing in such a way that the desired condition of a constant phase velocity over a wide frequency bandwidth will be lost. Similarly, increasing the height of the pillars will produce a slight increase in interaction impedance and a lower synchronous beam voltage, without much change to the slope of the dispersion curve, but will move the central frequency and the bandwidth out of the desired range. This information is used as a guide for optimisation of the DCW period, as there are many parameters which can be modified simultaneously.

The dispersion curve calculated is optimised for a wide bandwidth of synchronisation in the desired space harmonic.

In the following we will derive the equation of the synchronous beam line as a function of period, frequency, beam voltage and phase. The period of the structure for a specific frequency range is a function of the frequency. The phase difference ϕ may be defined in equation (95) as

$$\phi = k_z P \tag{95}$$

Where k_z is the phase constant, and P is the period of the DCW computed as distance between the axis of two adjacent pillars. Using equation (4) and equation (8), we can equate the phase velocity v_p with the electron velocity U_B, we can obtain

$$\sqrt{2\eta V_0} = \frac{2\pi f}{k_z} \tag{96}$$

Combining equation (95) and (96) for k_z and substituting gives

$$\sqrt{2\eta V_0} = \frac{2\pi f P}{\phi} \tag{97}$$

which rearranged gives

$$P = \frac{\phi \cdot 5.93.10^5 \sqrt{V_0}}{2\pi f} \quad (98)$$

The interaction impedance considered is that averaged over the radius of the electron beam and period of the structure, that is, the volume of the electron beam, although it can be useful to consider the on-axis interaction impedance for more precise comparisons of structures where the electron beam radius is not the same.

3.2 Fabrication

Fabrication of the designs is considered at every step. Due to the simplicity of the DCW, the main constraint is the distance between pillars and the distance between the walls.

In CNC milling, the size of the tooling is the limiting factor to the resolution. In the LIGA process, the limitation is in the inability for LIGA to produce height differences in the pillars.

THz DCW has been fabricated by both these methods [26] [20], so in terms of the realisation, where the highest frequency is 346 GHz, only internal manufacturing processes were considered as limiting factor. The limiting factor of the distance between pillars was the beam radius. It was decided to leave at least a distance of 50 μm to account for radial beam oscillations.

3.3 Design of the Coupler

An important aspect of the design of a TWT or BWO is to assure the matching from the input and output signal to the mode present in the interaction region. In the case of the DCW, we need to match the TE_{10} mode of the rectangular waveguide to the TE_{10} hybrid mode of the DCW SWS. The S_{11} must be optimised to reduce the reflection of incident signals.

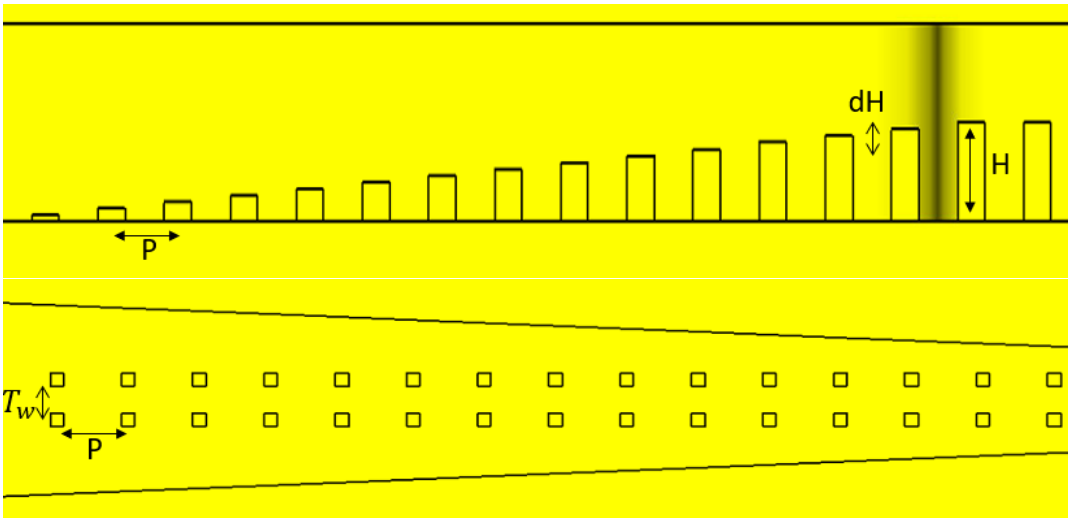

Figure *49* Height tapering of the pillars and width tapering of the waveguide. The long straight lines in the image represent the edges of the waveguide. dH is the change in pillar height per period of the tapering section

The aim is reducing S_{11} as much as possible, and to have S_{21} as close to 0 dB as possible. In practice, of course, this is impossible, as reflections due the impedance at the tapering not matching and electrical losses to the structure are finite.

Figure 49 shows how this can be achieved by tapering the height of the pillars of the SWS each period in the tapering sections, along with smoothly tapering the width of the rectangular waveguide. The change in pillar height is dH. The width tapering, and pillar height tapering are performed in the same place.

Shown in Figure 50 is an alternative to the height tapering technique named the 'lateral' tapering technique. It consists of pillars of identical height, but different spatial positions, symmetrically moving towards the wall of the waveguide. This tapering, depending on the ratio of the width tapering dimensions of the waveguide and the lateral shift in pillar position per tapering period, may result

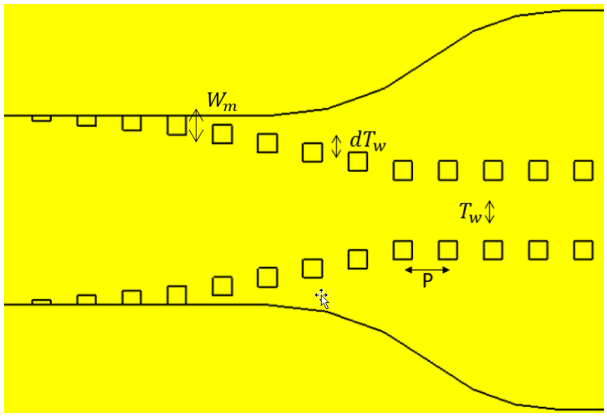

Figure *50* Width tapering of the waveguide and lateral tapering of the pillars. dT_w is the change in distance between the pillars

in a required pillar modification for pillars close to the wall of the tapering. An example of this would be if the pillar is too close to the wall to be reliably manufactured. As such, it may be necessary to extend these pillars in to the wall of the structure. The modified width of the pillar is labelled as W_m.

A good S_{11} parameter can be achieved with a long enough tapering section. However, it is often the case that this length would be limited due to design constraints. This means the other parts of the tapering must be more optimised.

Figure 51 show what is meant by height tapering of the waveguide. This is required if the standard flange is too tall or short for the waveguide. A good S_{11}

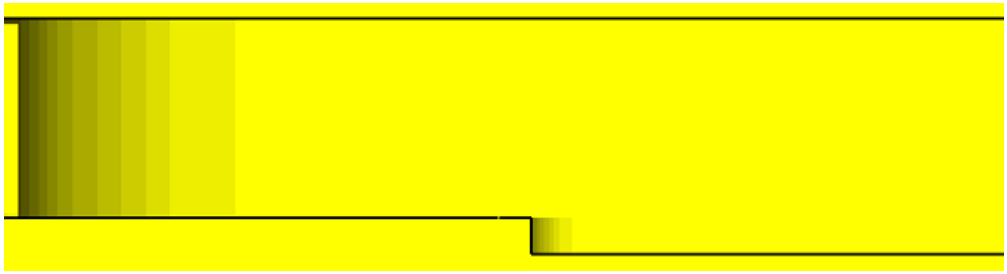

Figure *51* Height tapering of the height of the waveguide

parameter is defined here as better than -15 dB. The bandwidth is defined as the band of frequencies over which the S_{11} is less than -15 dB, or as the predefined operation frequency of the tube.

3.3.1 Bend Tapering

A bend type tapering is also considered. When the linear tapering is applied, there are long regions of weak interaction between the signal and the electron

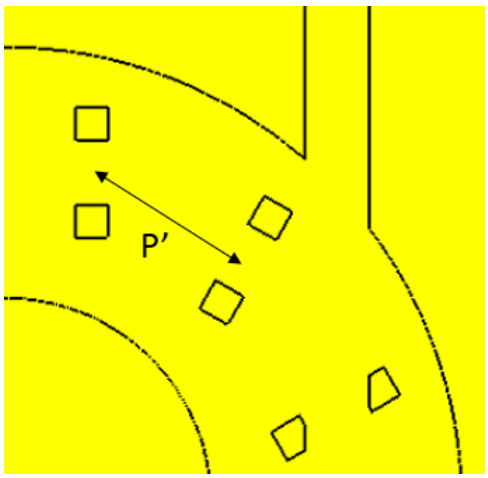

Figure *52* P', the periodicity of the pillars in the bend

beam, but where the beam still requires confining by a magnetic field. This extra length can account for a significant proportion of the tube.

By considering a 90 degree bend, such that the tapering occurs perpendicular to the direction of the interaction region, the size of the device can be reduced [65].

As shown in Figure 52, the complexity of such a geometry arises when trying to maintain the mode of the structure around the bend, where the periodicity of the SWS is not well defined, and as such may impact on the stability of the operational mode. To match the period as close as possible, it was decided to maintain the periodicity of the structure along the centre of the pillars; that is the distance between the centres of the SWS in the bend.

Another issue is where a pillar may be in the way of the electron beam. The solution is to shape or move the pillars on the trajectory of the beam. This must be done carefully to avoid potential reflections at the bend. Figure 53 shows the crossing of the corner of a pillar by the electron beam.

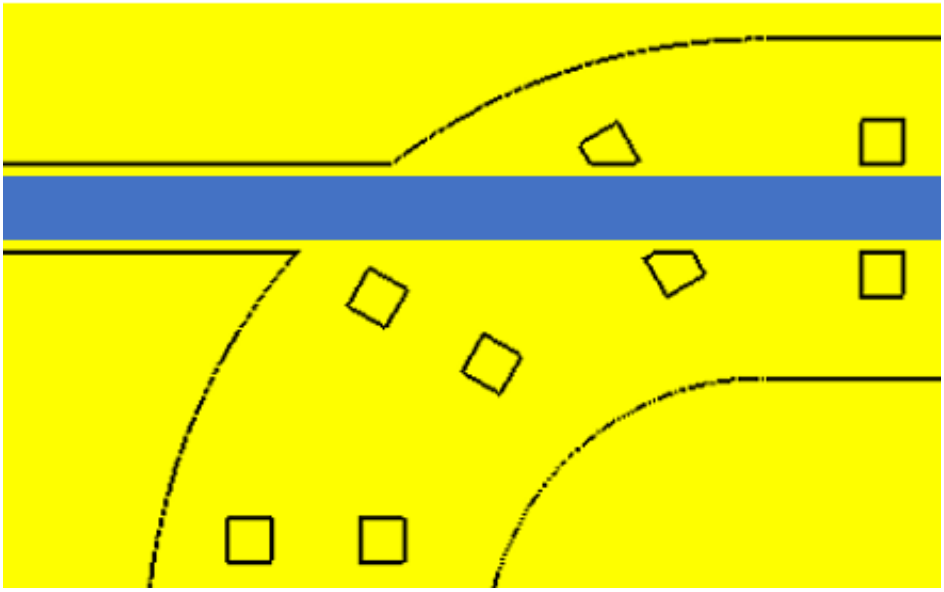

Figure *53* Illustration of the electron beam unimpeded due to shaped pillars

3.4 Coupler Comparisons for 346 GHz DCW BWO

Comparisons of the couplers for the 346 GHz is described in the following. The parameters of the DCW for the 346 GHz BWO are shown in Table 4. Figure 56 shows the height tapering of the pillars, and Table 5 shows the associated parameters. The configuration consists of 14 tapered pillars, each differing in height by $10\ \mu\mathrm{m}$. Figure 55 shows the lateral tapering of pillars. 4 of the pillars are attach to the wall of the waveguide. The parameters of the lateral shaping are presented in Table 6. Dispersion curve is shown in Figure 54.

Table 4 Parameters of the 346 GHz DCW BWO

Parameter	Value/$\boldsymbol{\mu m}$
A	1500
B	300
T	230
W	70
S	70
H	150
P	170

Table 5 Parameters of the pillar tapering in the linear height tapering configuration for 346 GHz BWO

Parameter	Value/$\boldsymbol{\mu m}$
dH	10

Table 6 Parameters of the pillar tapering in the lateral tapering configuration 346 GHz BWO

Parameter	Value/$\boldsymbol{\mu m}$
$\mathrm{dT_w}$	33
W_m	74

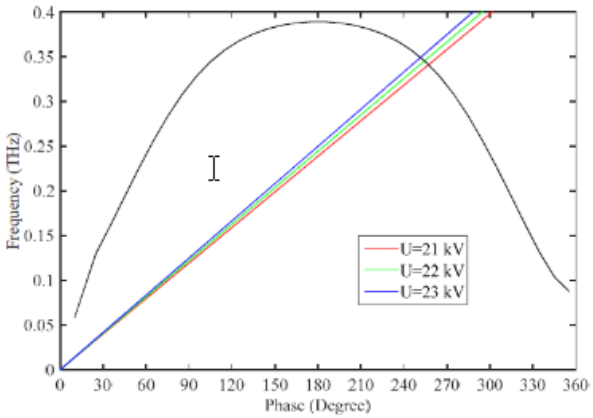

Figure 54 Dispersion curve of 346 GHz DCW BWO

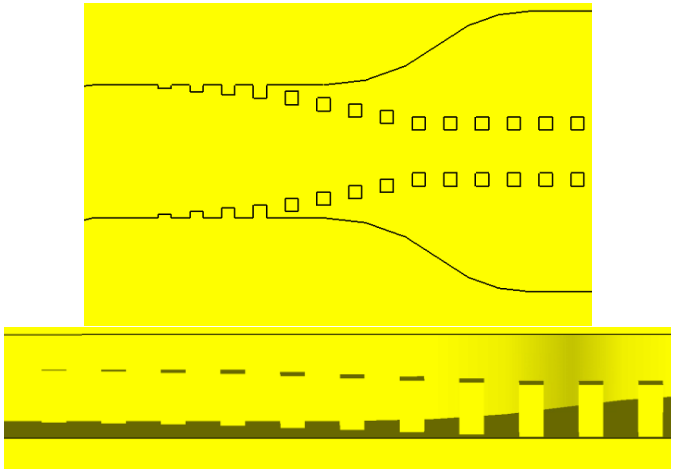

Figure *55* Top view of the lateral tapering and side view of the lateral tapering

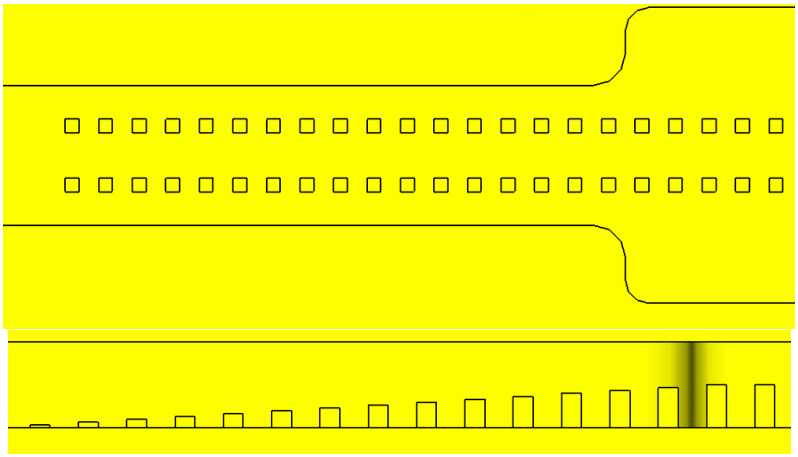

Figure *56* Configuration of the linear height tapering from the top, and from the side, showing the height tapeirng

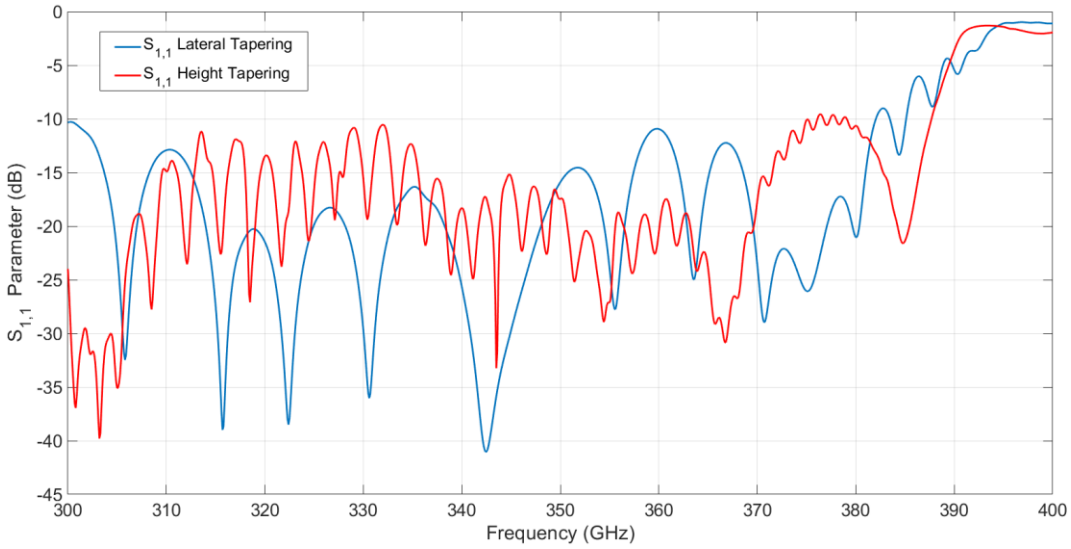

Figure *57* Simulated S_{11} of the lateral tapering and height tapering configurations

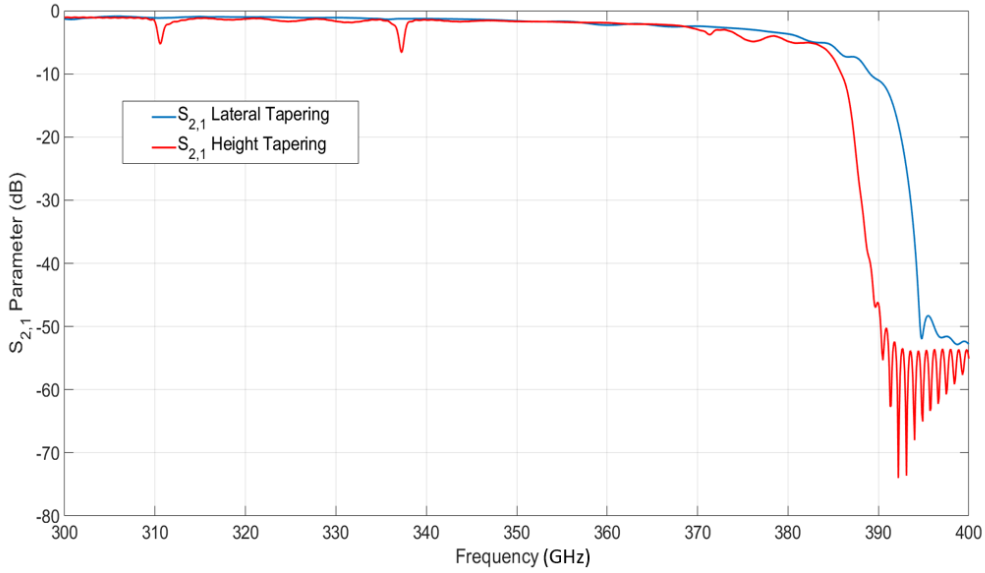

Figure *58* Simulated $S_{21}$of the lateral tapering and height tapering configurations

Figure 57 and Figure 58 show the S_{11} and S_{21} of the lateral and height tapering configurations of the couplers for the 346 DCW BWO. Both configurations for the coupler have S_{11} better than -15 dB reflection over a bandwidth of greater than 10 GHz. The S_{21} parameter is better than -2 dB across the whole band.

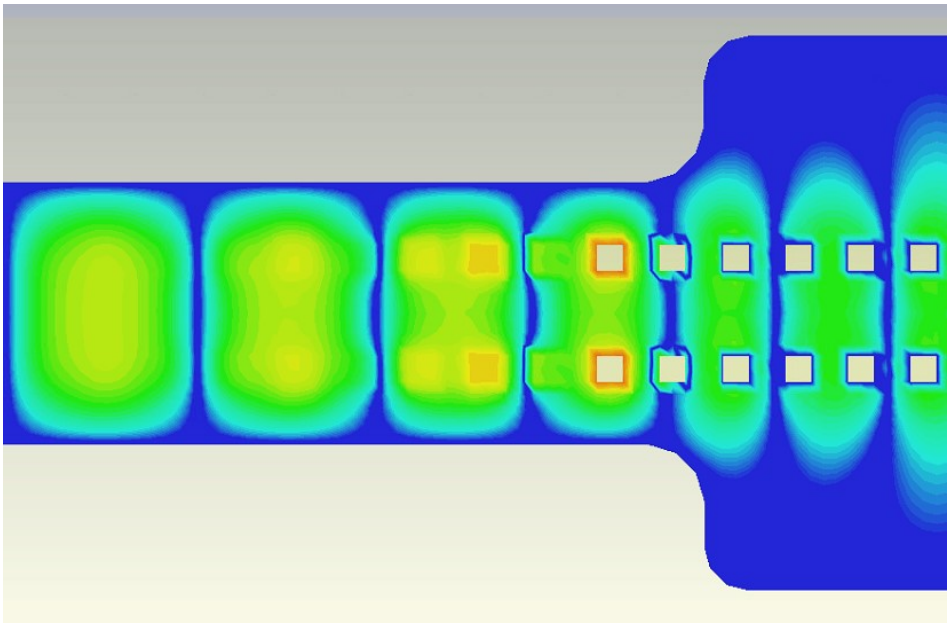

Figure *59* Top view of the y-component of the electric field in the height

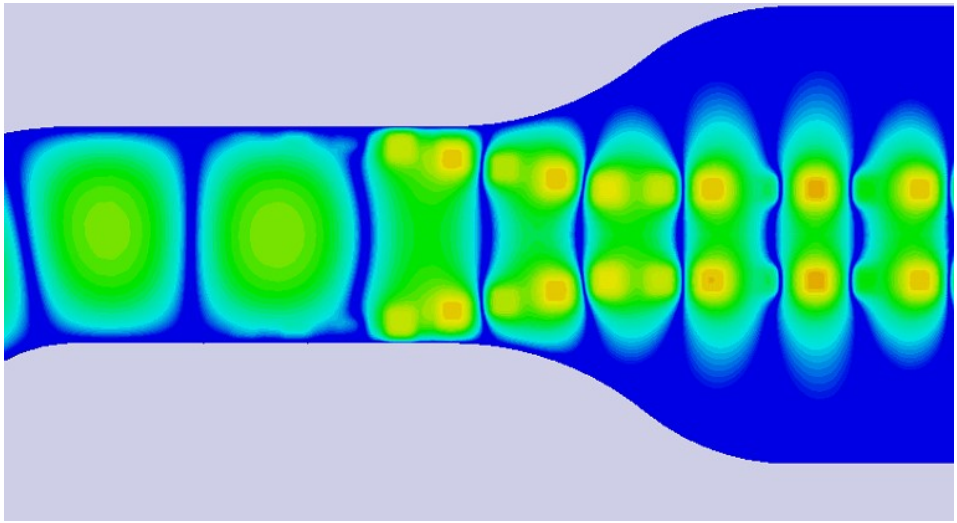

Figure *60* Top view of the y-component of the electric field in the lateral tapering at 346 GHz

Figure 59 and Figure 60 show from the top of the y-component of the electric fields as the mode of the field transforms in to a TE_{10} hybrid mode supported by the DCW for the height tapering and lateral tapering respectively.

3.4.1 Conclusion

It has been shown that both height tapering and lateral tapering of the pillars in the DCW are viable techniques for matching the DCW's hybrid TE_{10} mode with the TE_{10} mode of the flange. Both are capable of wideband acceptance of signals, with S_{11} of better than -15 dB over a bandwidth wider than 10 GHz.

3.5 100 GHz BWO

A design of a 100 GHz BWO is described. The parameters of the DCW at 100GHz are shown in Table 7. The BWO works at the first backward wave harmonic.

Table 7 Parameters of the DCW for 100 GHz BWO

Parameter	Value/$\boldsymbol{\mu m}$
A	5200
B	750
T	780
W	225
S	225
H	550
P	445

3.5.1 Cold Parameters

The cold parameter results calculated using eigenmode simulation are described. The parameters of DCW are shown in Table 7. The voltage required

was 10.85 kV. The beam radius was 340 μm. This limits the pillar distance to 780 μm.

Figure 62 is the dispersion diagram and the dotted black line shows the beam line corresponding to this beam voltage. The beam line intercepts the dispersion curve at 100 GHz.

For this 100 GHz BWO, the synchronous beam voltage is close to 10kV, with an average interaction impedance over the electron beam cross section of ~0.4 Ohm, as shown in Figure 61.

The interaction impedance and synchronous beam voltage were achieved by careful selection of the period of the SWS, which tends to be smaller for the first backwards space harmonic than for the forward wave harmonic used by

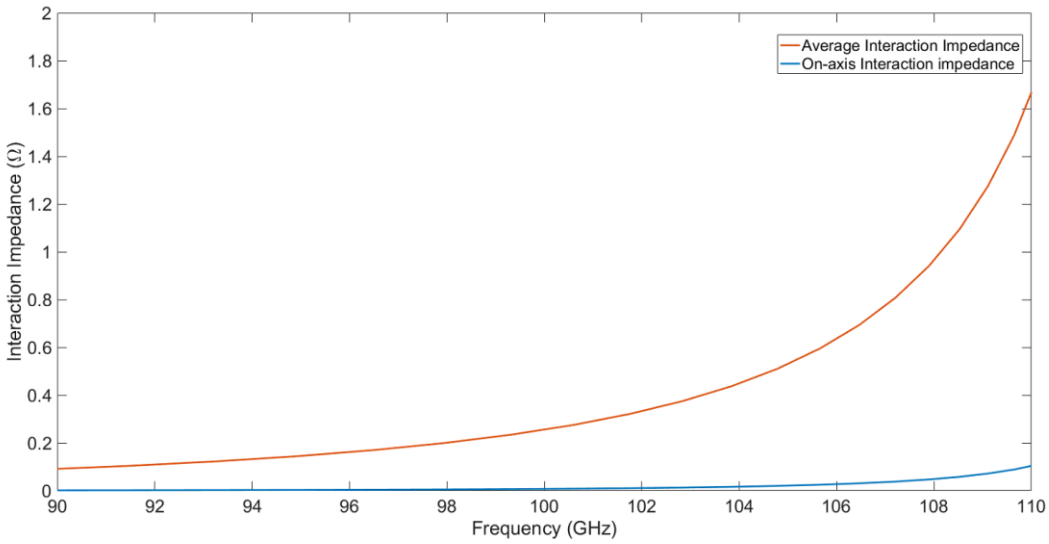

Figure *61* On-axis and average interaction impedance for the 100 GHz BWO

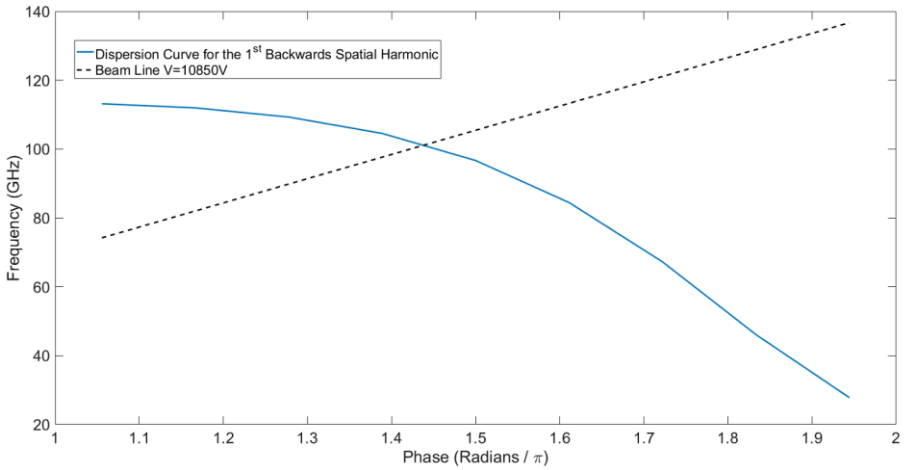

Figure *62* Dispersion curve for the 100 GHz BWO, with a beam line intersecting at 100 GHz with a beam voltage of 10850V

the DCW. This is because the period of the structure is proportional to the phase difference. Figure 63 shows the E_z field distribution taken at a cross-section perpendicular to the beam axis.

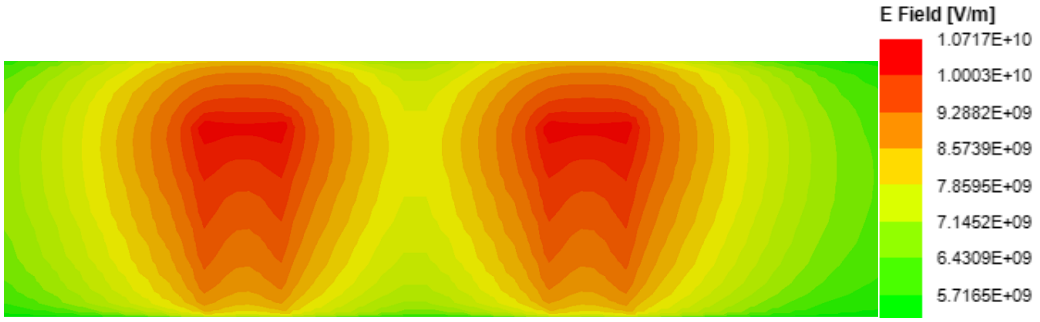

Figure *63* z-component of the electric field distribution for the 100 GHz BWO

Table 8 Parameters of the pillar tapering in the lateral tapering configuration for 100 GHz BWO

Parameter	Value/$\boldsymbol{\mu m}$
dT_w	60
W_m	202.5

For the 100 GHz BWO, the lateral tapering configuration for the pillars was utilised. Figure 64 shows the empty tapering section. The parameters are shown in Table 8.

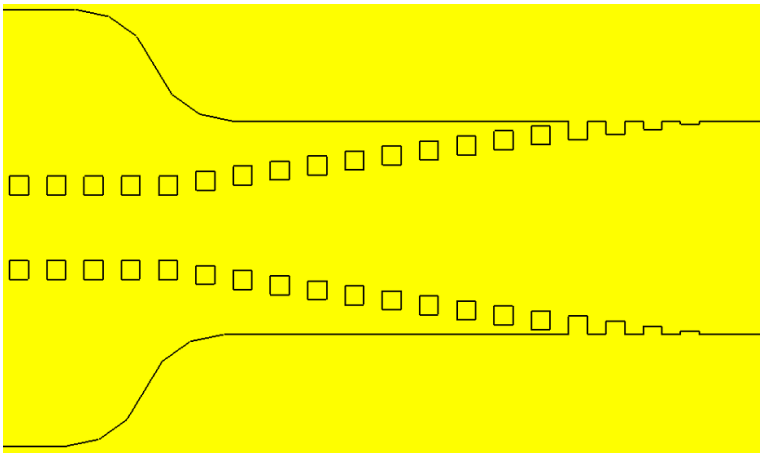

Figure *64* Tapering configuration

Figure 66 shows the S_{11} for the 100 GHz BWO from 60 GHz to 115 GHz.

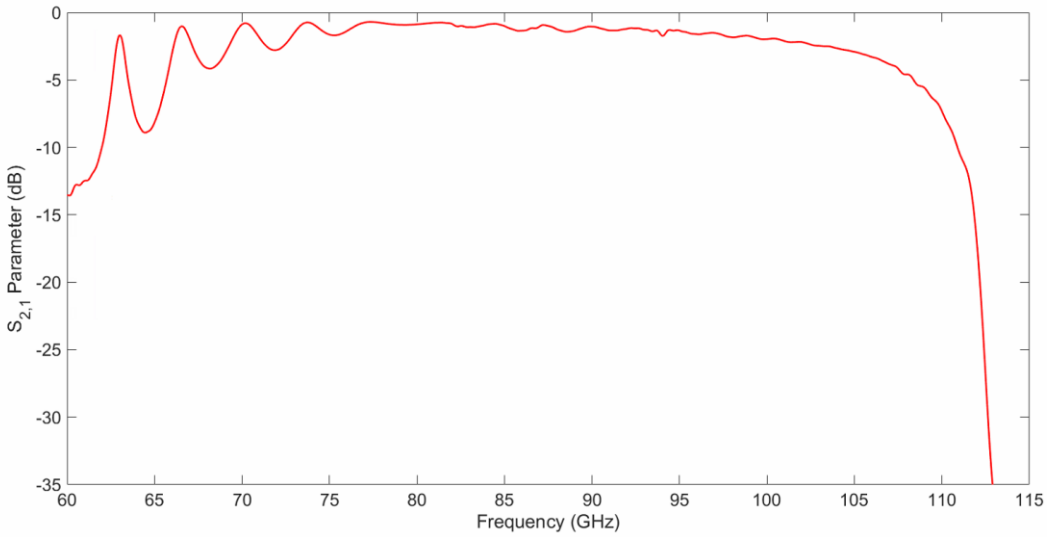

Figure *65* Simulated S_{21} for the 100 GHz BWO

Figure 65 show the S_{21} for the same frequency range. The S_{11} is better than -15 dB from 100 GHz to 107 GHz, and the S_{21} is better than -3 dB over the same range.

Figure 67 shows the y-component of the RF wave at 100 GHz as it changes from TE_{10} to the hybrid TE_{10} of the DCW. The y-component is shown as it best shows the conversion of the mode.

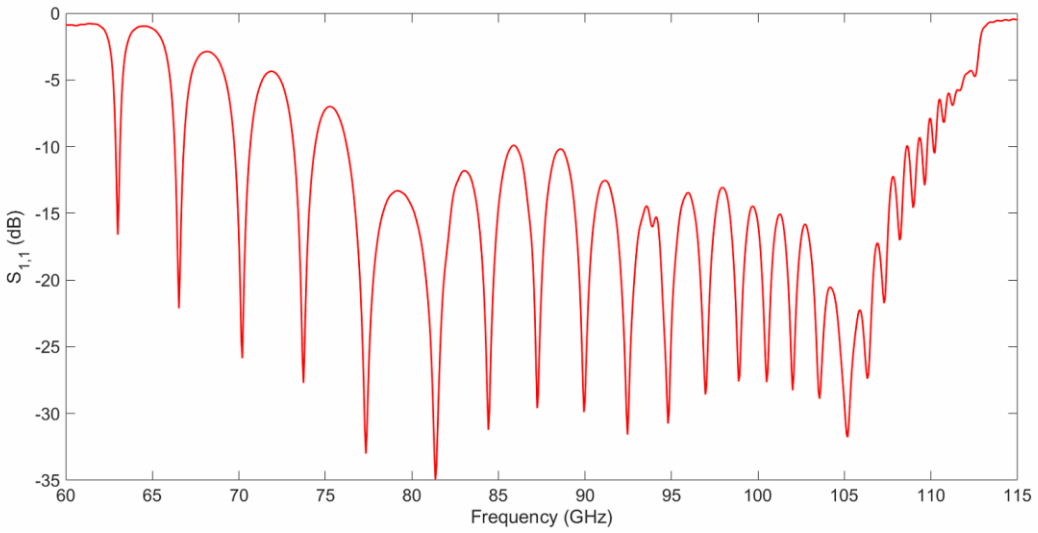

Figure *66* Simulated S_{11} for for 100 GHz BWO

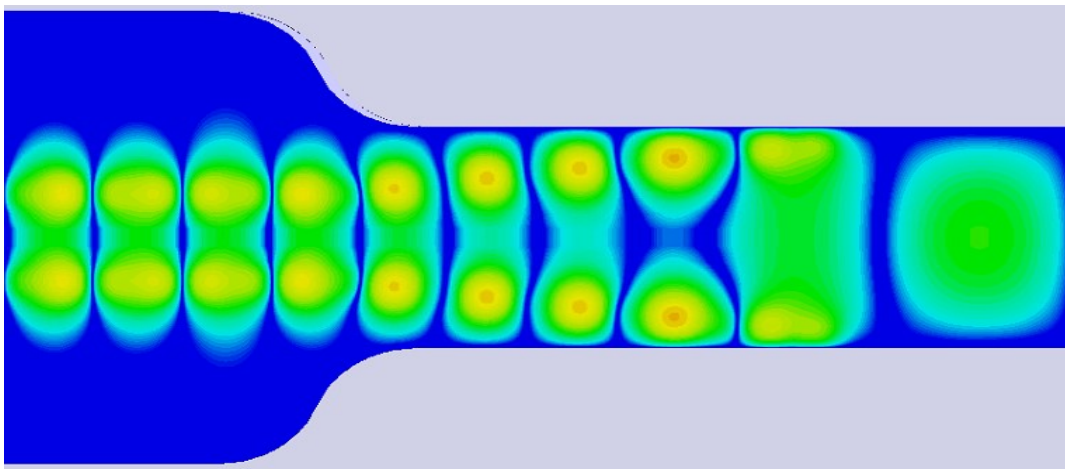

Figure *67* Y-component of the electric field in the tapering at 100 GHz

3.6 270GHz TWT

A design for a DCW for a 270 GHz TWT is described. The parameters of the DCW are shown in Table 9. The first forward wave harmonic is used.

3.6.1 Cold parameters

The beam voltage desired was at 13.7 kV. The beam radius was 100 μm. This limits the pillar distance to 300 μm.The dispersion curve is shown in Figure 68. The bandwidth of synchronism is better than 20 GHz centred at about 270 GHz. The on-axis and average interaction impedance are shown in Figure 69. The field distribution is shown in Figure 70.

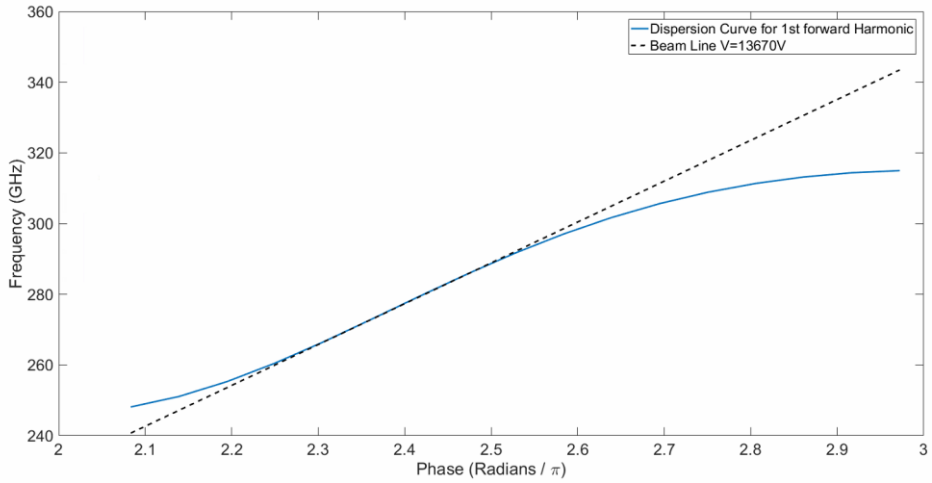

Figure *68* Dispersion curve of the 270 GHZ DCW TWT, with an intersecting beam line at 13.67 kV

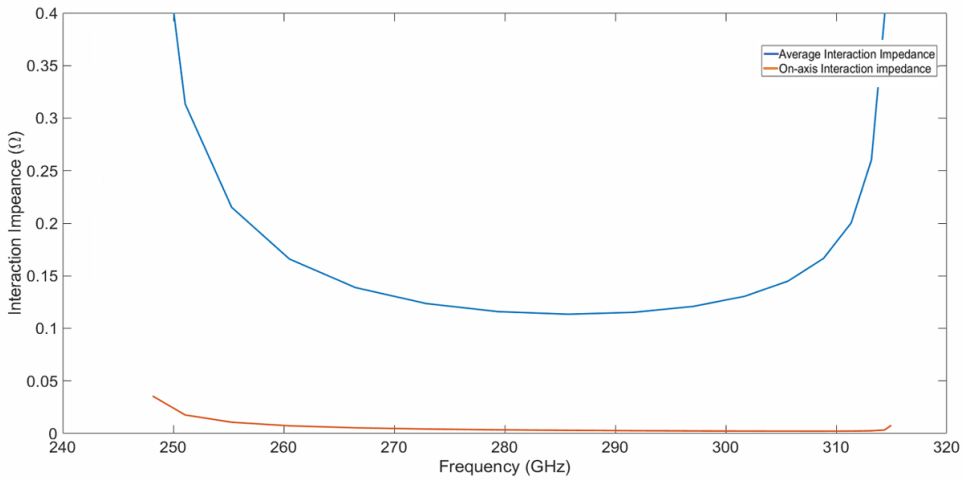

Figure *69* Average and on-axis interaction impedance of the 270 GHz DCW TWT

Table 9 Parameters of the 270 GHz DCW TWT

Parameter	Value/μm
A	520
B	320
T	300
W	70
S	70
H	190
P	300

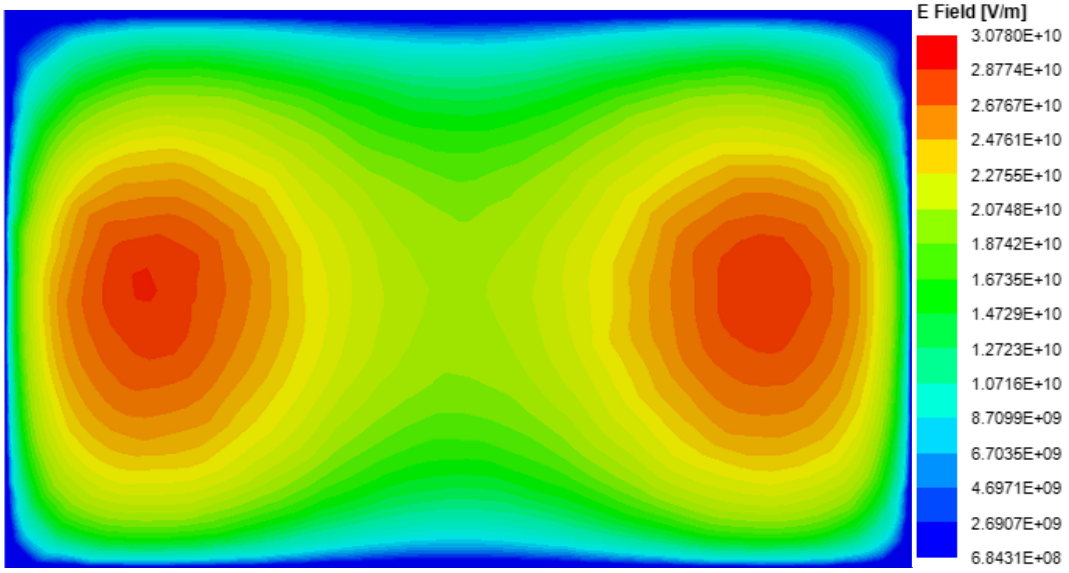

Figure *70* z-component of the electric field distribution of the 270 GHz DCW TWT

Table 10 Parameters of the pillar tapering in the lateral tapering configuration for 270 GHz TWT

Parameter	Value/$\boldsymbol{\mu m}$
dT_w	5
W_m	77

For the 270 GHz TWT, the lateral tapering configuration for the pillars was utilised. The configuration is show in Figure 71. Table 10 shows the parameters of the tapering. There are 18 pillars in the tapering section. 6 of these pillars are attached to the wall of the waveguide. Figure 72 shows the y-component of the RF wave at 270 GHz as it changes from TE_{10} to the hybrid TE_{10} of the DCW. The y-component is shown as it best shows the conversion of the mode.

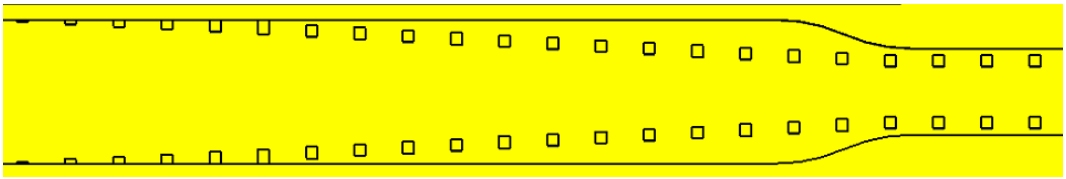

Figure *71* Configuration of the coupler

Figure 73 shows the simulated S_{21} for the 270 GHz TWT from 240 GHz to 310

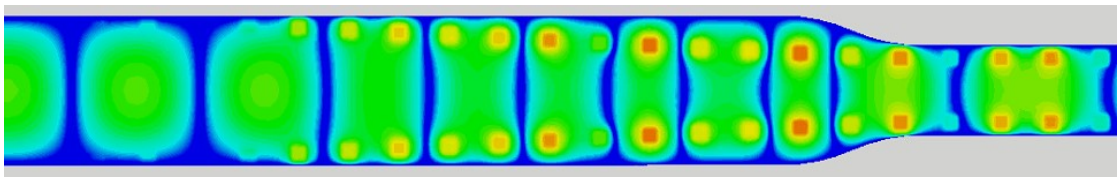

Figure *72* Top view of tapering of the pillars; and the field distribution around the tapering for the 270 GHz DCW TWT

GHz. Figure 74 shows the simulated S_{11} for the same frequency range. The S_{11}

is better than -15 dB from 267 GHz to 277 GHz, and the S_{21} is better than -5 dB over the same range.

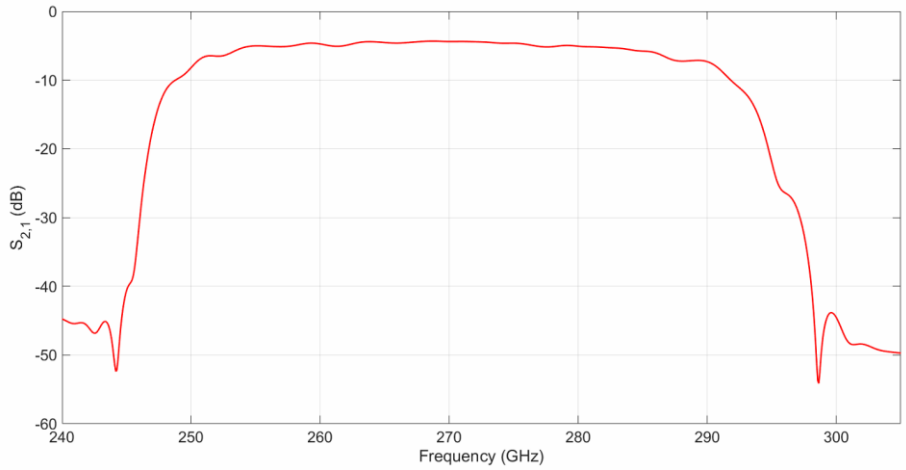

Figure *73* Simulated $S_{2,1}$ parameters for the 270 GHz DCW TWT

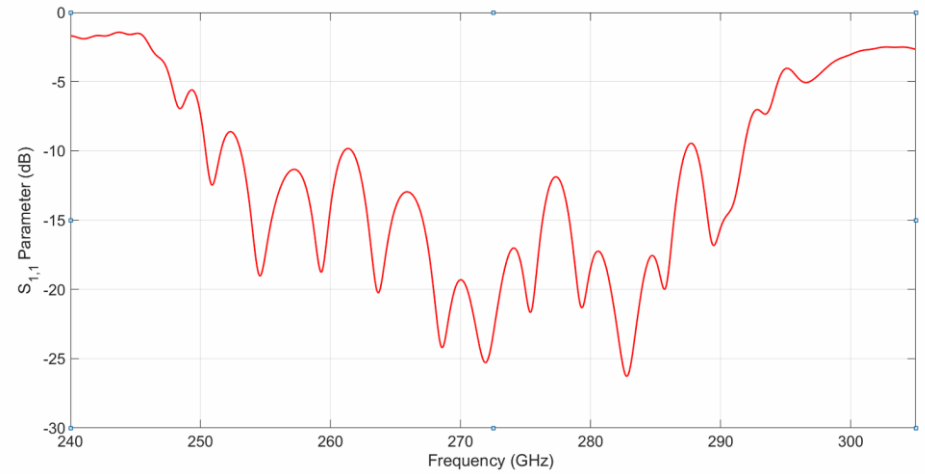

Figure *74* Simulated $S_{1,1}$ paramters for the 270GHz DCW TWT

3.7 W-Band TWT for TWEETHER Project

A W-band TWT is described for application in wireless communications in the TWEETHER project [69].

Two configurations of the pillars are investigated; square pillars and triangular pillars. The bandwidth required was at least 3 GHz, 92-95 GHz.

The straight taper and the bend taper are compared. The pillar tapering will be height tapering in both cases. The beam radius was 100 μm. This limits the pillar distance to 300 μm.

Table 11 Parameter list of the 90 GHz DCW period with square pillars

Parameter	Value/μm
A	1156
B	689
T	300
W	150
S	150
H	511
P	800

3.7.1 DCW Design for 92-95 GHz – Square Pillars

Described is W-band DCW with square pillars. The constraints were a beam radius of 100 microns. This means the gap between the pillars must be at least 300 microns. The beam voltage is fixed at 10.1 kV. Table 11 shows the parameters of the DCW.

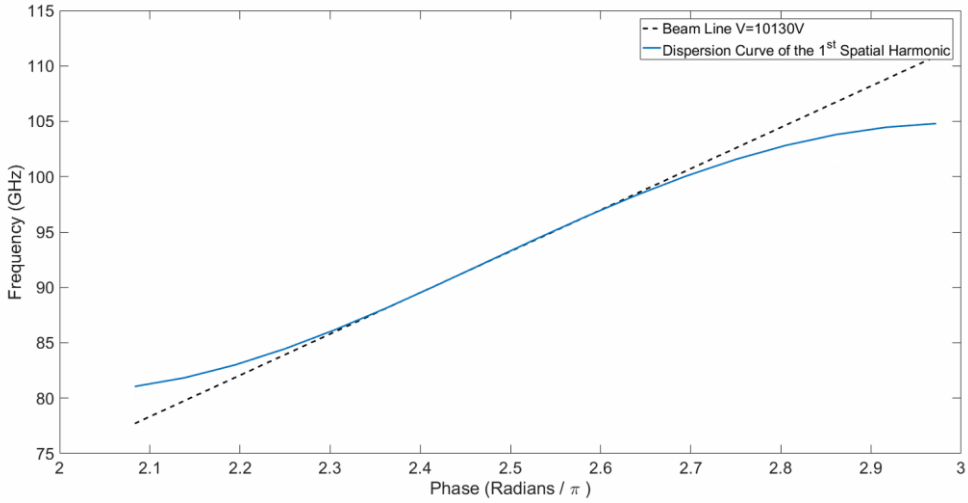

Figure *75* Dispersion curve over the bandwidth shown in terms of phase difference. The beam line is shown, with a voltage of 10.3 kV

Shown in Figure 76 is an interaction impedance of 1 Ohm on average. Figure 75 shows the dispersion curve of the DCW. The beam line corresponds to 10.3 kV and shows a synchronous bandwidth of greater than 9 GHz.

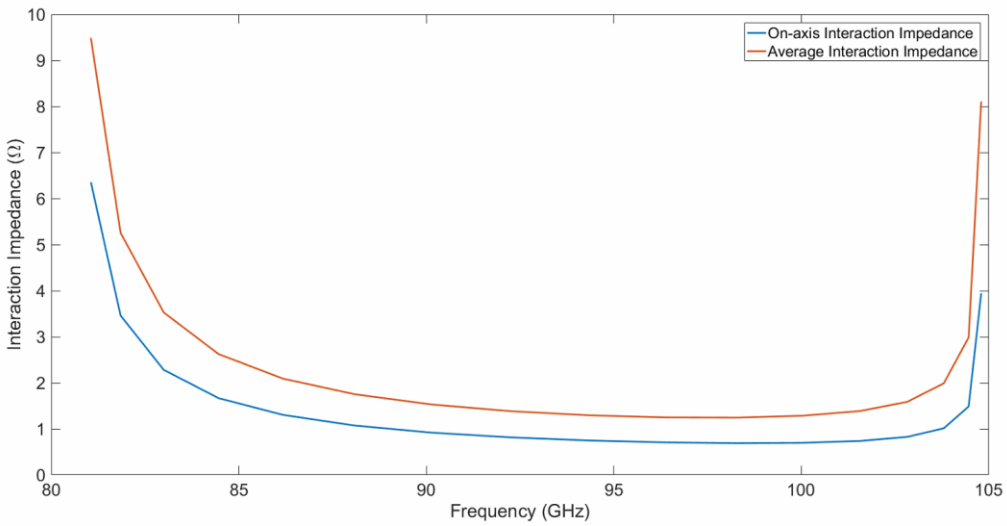

Figure *76* Average and on-axis interaction impedance over the bandwidth as a function of frequency for the square pillar DCW period

3.7.2 DCW Design for 92-95 GHz – Triangular Pillars

Shown in Figure 77 and Figure 78 is the geometry of the DCW with triangular pillars. The triangular cross section pillars are triangular prisms. They are positioned in the waveguide in the same way as the square pillars in terms of distance from the waveguide wall and distance from each other, both in the axial direction and width-wise. Each triangular cross section is an isosceles triangle. The base of the isosceles triangles face each other. The distance between them is the beam tunnel width. The parameters are the same as in Table 11.

This configuration has been shown to result in a higher interaction impedance, in this case of around 50% [70]. This could be because of the triangular pillars

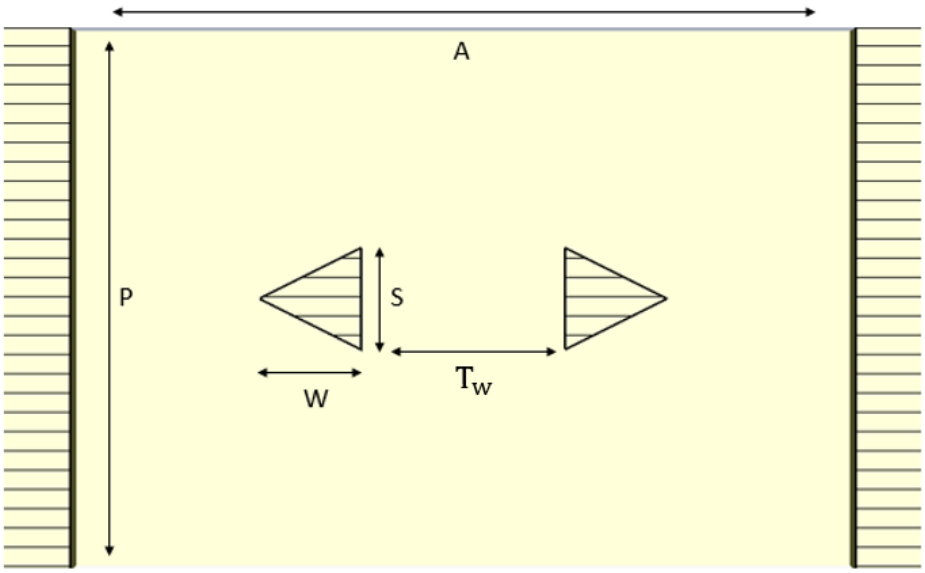

Figure 77 Top view of the triangle pillared DCW period

allowing a higher energy field to exist in between the periods of the structure. Figure 80 shows the interaction impedance. An average of about 2 Ohms was achieved on average.

The synchronous beam voltage is about 10.6 kV. This is similar to the DCW with square pillars, described in the previous section.

Figure 79 shows the dispersion curve of the DCW.

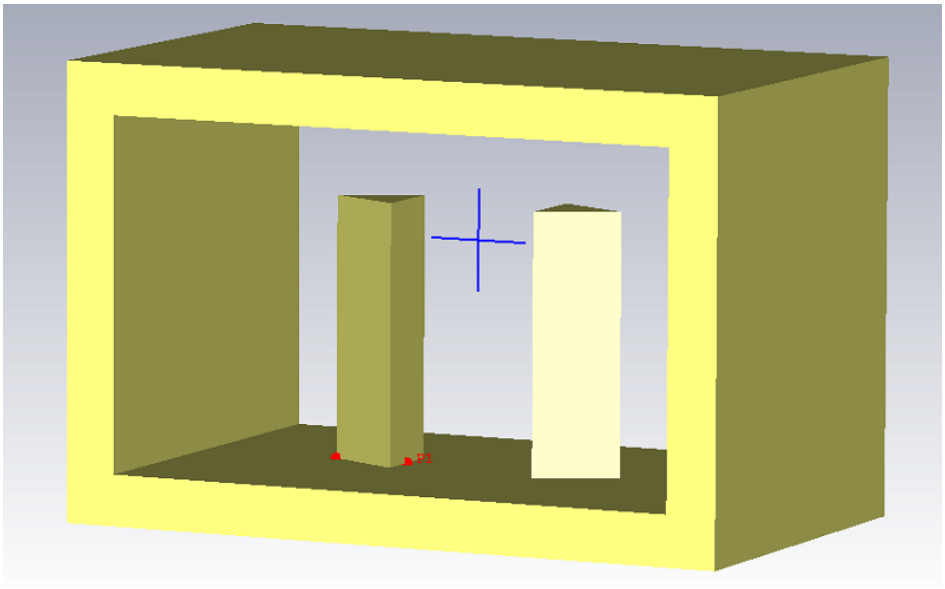

Figure *78* Period of the 90 GHz DCW period with triangular pillars

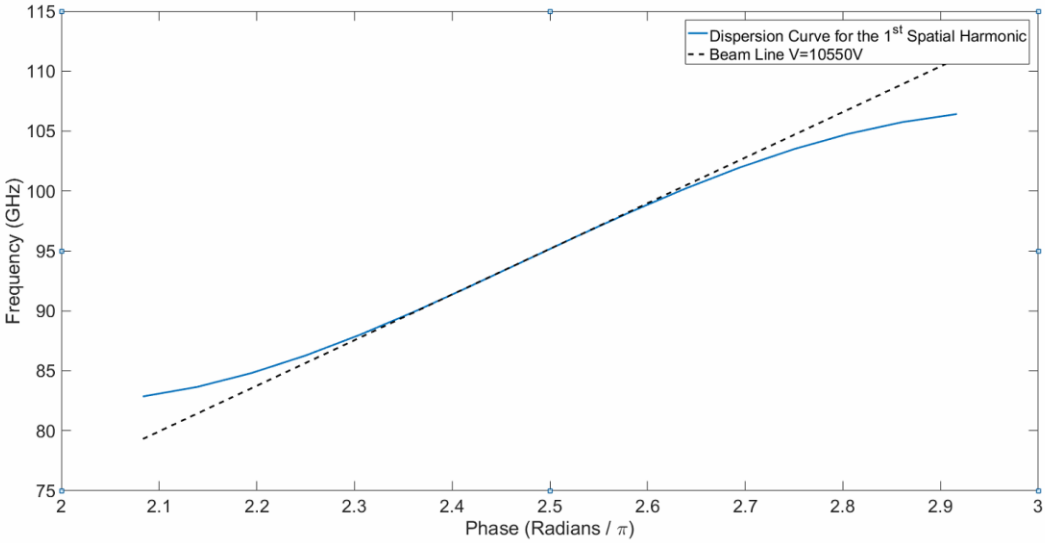

Figure *79* Dispersion curve over the bandwidth shown in terms of phase difference. The beam line is shown, with a voltage of 10.55 kV

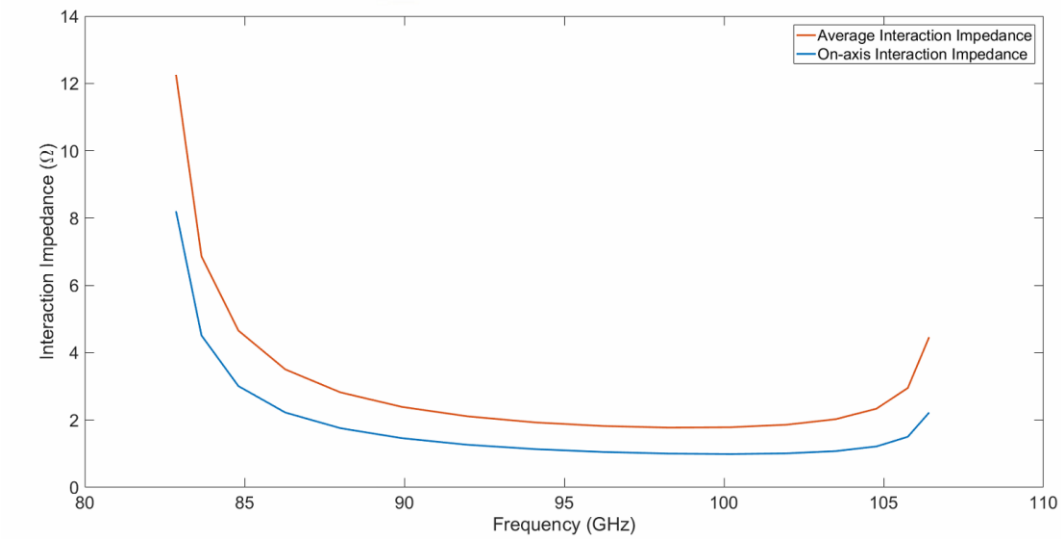

Figure *80* Average and on-axis interaction impedance over the bandwidth as a function of frequency for the triangular pillared DCW

3.7.3 Couplers

Below are presented the taper configurations investigated. The height tapering of the pillars is utilised in both approaches. In the case of the bend tapering, the difference between the shaped and non-shaped pillar is also discussed. The parameters of the tapering are shown in Table 12.

3.7.4 Straight Taper Square Pillars

The straight tapering configuration uses the height tapering of the pillars and

Table 12 Parameters of the pillar tapering in the linear height tapering configuration for W-band DCW

Parameter	Value/$\boldsymbol{\mu m}$
dH	34

width tapering of the waveguide simultaneously. 15 pillars are used in the

tapering section. Figure 81 a) shows the side view of the tapering configuration and Figure 81 b) shows the top view. The value of $\mathrm{dH} = \sim 34\ \mu\mathrm{m}$.

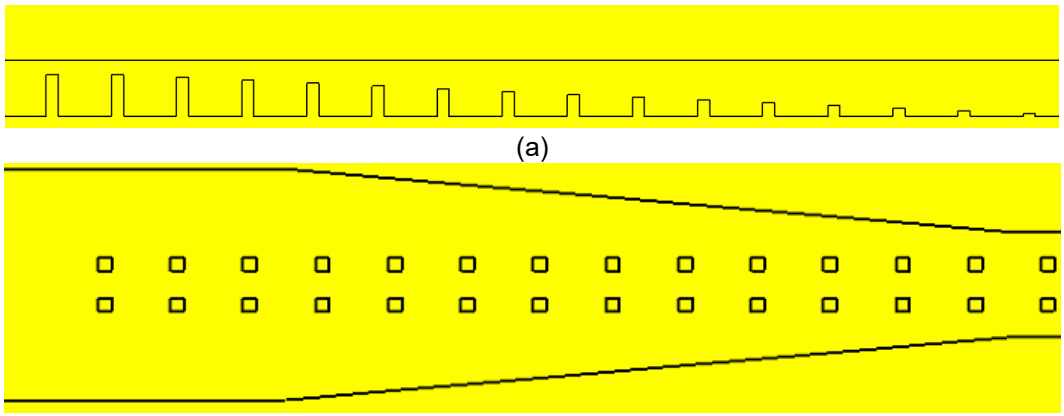

(a)

(b)

Figure *81* The side view and top view of the straight tapering for the W-band DCW TWT

Figure 82 shows the simulated S_{11} for the W-band TWT from 80 GHz to 110 GHz. Figure 83 show the simulated S_{21} for the same frequency range. The S_{11} is better than -15 dB, and the S_{21} is better than -3 dB over the whole range of the device 92-95 GHz.

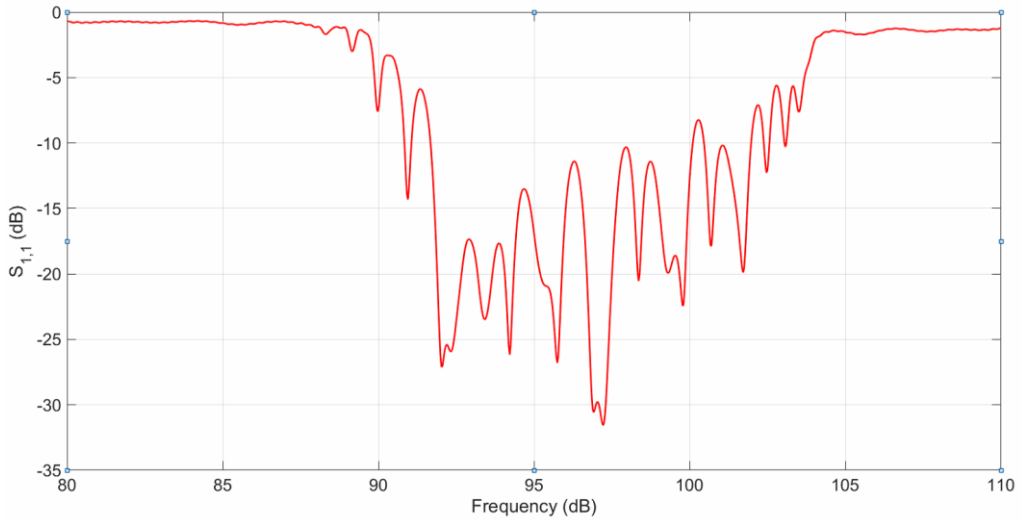

Figure *82* Simulated $S_{1,1}$ paramters for the W-band DCW with square pillars in the 'straight' configuration

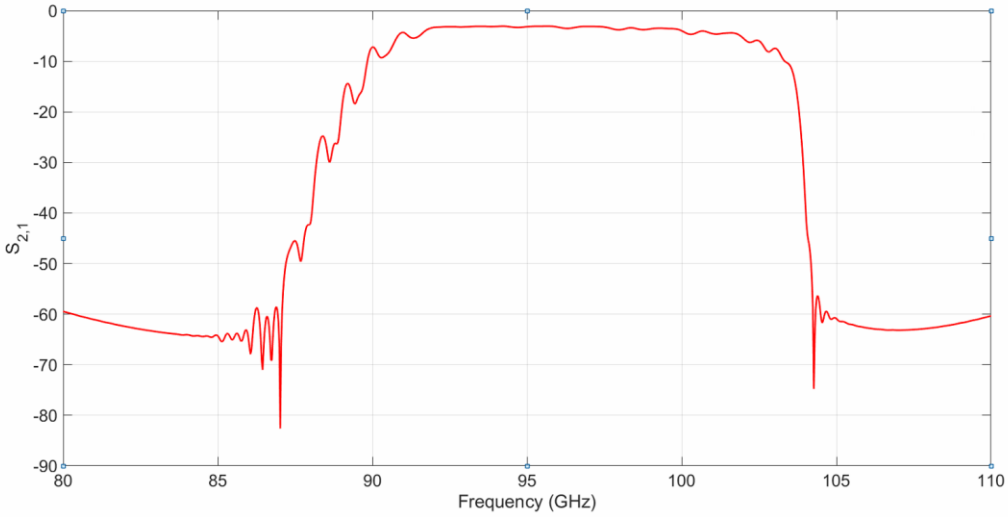

Figure *83* Simulated $S_{2,1}$ paramters for the W-band DCW with square pillars in the 'straight' configuration

Figure 84 shows the y-component of the field in the taper. It can be seen how the field converts from the TE_{10} mode to the hybrid mode supported by the DCW.

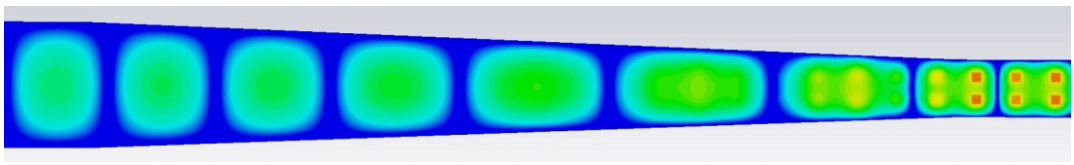

Figure 84 The y-component of the propagating field in the taper

3.7.5 Bend Tapering Square Pillars

The bend tapering configuration is shown inset in Figures 85 and 86. The pillars at the bend that cross into the region in which the beam will exist must be shaped to avoid potential collisions of the beam and pillars. As shown in in Figure 85 and Figure 86 the $S_{1,1}$ and $S_{2,1}$ parameters were affected only slightly. This is because the cut was only very small. The $S_{1,1}$ is better than -15 dB over 10 GHz between 90 and 100 GHz, and the $S_{2,1}$ is better than -3 dB from 85 GHz to 98 GHz. Figure 87 shows the field around the bend.

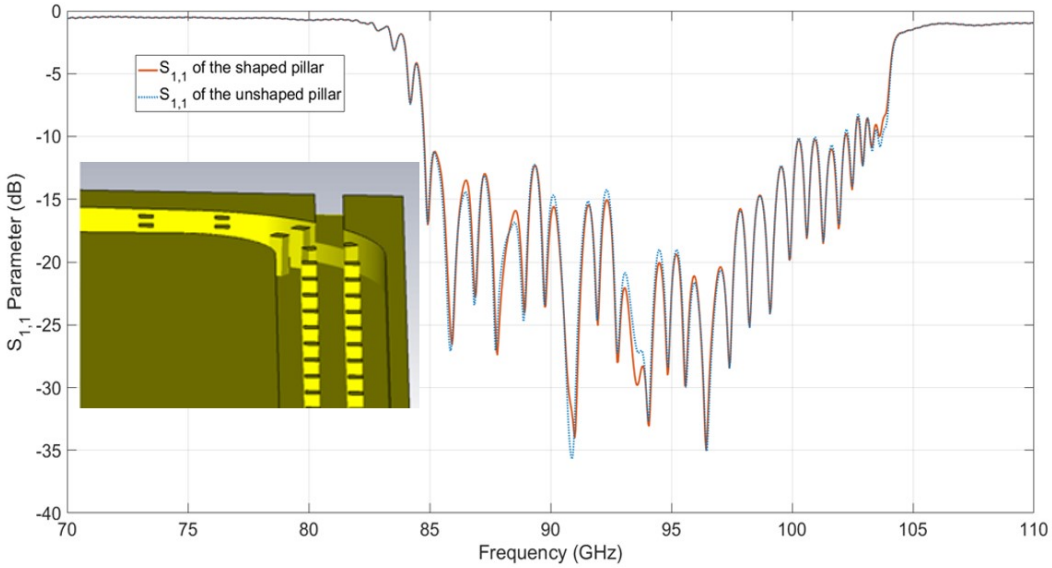

Figure 85 S_{11} of the tapering with the pillars in the bend of the tube showing the shaped and unshaped pillars. The configuration is inset.

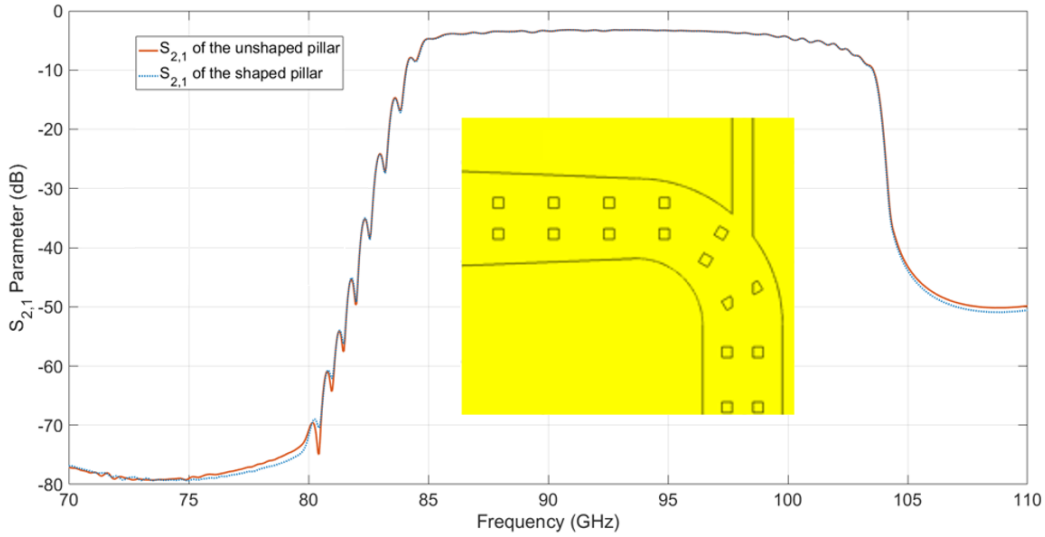

Figure 86 S_{21} of the tapering with the pillars in the bend of the tube, showing the shaped and unshaped pillars.

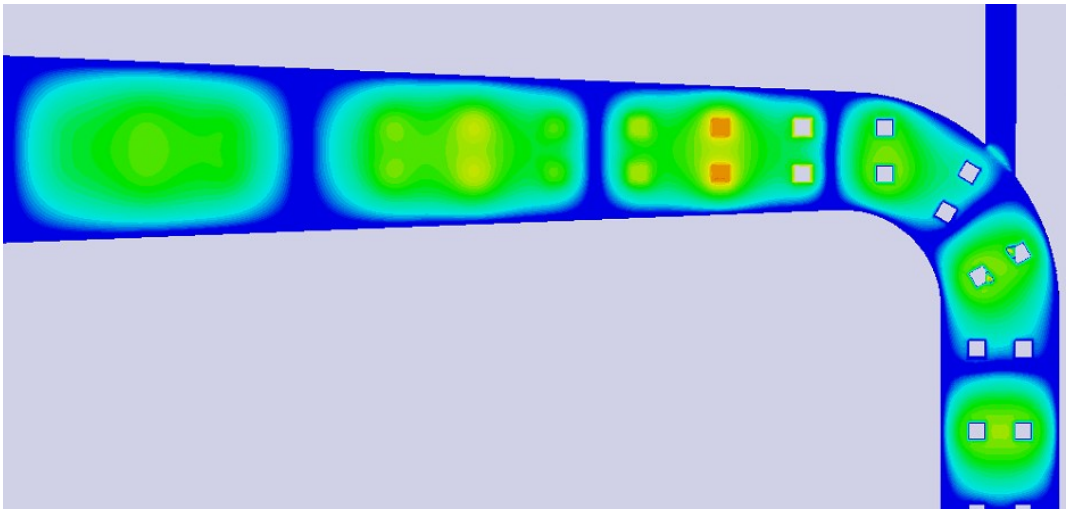

Figure 87 Field establishing around the bend

3.8 Conclusions

In this chapter, a comparison of two coupler configurations has been performed, and several SWSs and couplers using the DCW have been designed.

Two coupler configurations have been investigated for the DCW using a BWO designed for 346 GHz central frequency. Height tapering and lateral tapering of pillars of the DCW have been shown to be capable of producing the S-

parameters required for successful operation of DCW. The height tapering configuration performed with S_{11} better than -15 dB across a bandwidth of greater than 30 GHz. The lateral tapering performed similarly, with S_{11} better than -15 dB over the same range. The S_{21} is better than -5 dB over the range.

A BWO at 100 GHz was designed utilising the DCW with adequate interaction impedance of about 0.4 Ω and a low synchronous beam voltage of 10.85 kV. The tapering configuration considered was lateral tapering and achieved S_{11} better than -15 dB over a bandwidth of 100 GHz to 107 GHz, and S_{21} better than -3 dB over the same range.

A TWT at 270 GHz was also designed employing the DCW. Due to the requirement of a large tunnel width, the interaction impedance calculated was low, at about 0.15 Ω. The synchronous beam voltage is about 13.7 kV. The tapering configuration again was lateral tapering and achieved S_{11} better than -15 dB over a bandwidth of 267 GHz to 277 GHz, and S_{21} better than -5 dB over the same range.

A W-band TWT at 95 GHz was also designed. The minimum bandwidth required was 3 GHz from 92 GHz to 95 GHz. Two DCW configurations were considered for the period. The square pillar design and the triangular pillar design. The square pillar DCW achieved an interaction impedance of over 1 Ω. The synchronous beam voltage was 10.1 kV. The triangular pillars achieved an average interaction impedance of over 2 Ω and a synchronous beam voltage of about 10.5 kV. The design period enabled a bandwidth ~10 GHz.

The square pillars were moved on into the tapering stage. The straight tapering achieved S_{11} better than -15 dB over almost all the band, and S_{21} better than -3 dB over all the band. The bend taper with no pillar shaping and with pillar

shaping were almost identical, with the shaped pillar configuration having slightly better S-parameters. The $S_{1,1}$ is better than -15 dB over 10 GHz bandwidth, and the $S_{2,1}$ is better than -3 dB over the entire band.

The DCW is also capable of maintaining good S-Parameters whilst the corrugations bend around a curve, which includes several of the pillars being 'shaped' so that the pillars do no impede the passing of the electron beam. The mode of the DCW is only minorly disrupted as it propagates through the bend. It was shown that with correct shaping there is no significant difference in S-parameters between shaped pillar and no shaped pillar in the W-band case, and just as good S-parameters as with the case in W-band with no bended taper.

It should be noted that as well as having a lower cut off frequency, the DCW also has an upper cut off frequency. This is seen in the S_{11} parameters, where consistently, there almost total reflection of the received signal below and certain frequency, and above a certain frequency. The same is observed in the S_{21} parameters, where there is close to zero transmission of the received signal above and below certain frequencies, depending on the waveguide. This suggests that the coupler and the SWS act as a band pass filter.

Chapter 4 Conclusions and Future Work

The motivation for this work came from advances in microfabrication technology, which has made the fabrication of structures small enough for operation in the mm-wave and THz frequency regimes feasible. Since the helical waveguide, the premier SWS in terms of bandwidth, is too difficult to fabricate at such small dimensions (~100 μm radius), new structures must be investigated. Many of these SWSs, such as the DCW, are asymmetric in topology.

4.1 Thesis Purpose

A novel Lagrangian method for quickly simulating the beam wave interaction in TWTs with asymmetric SWSs has been presented. It included a novel method for calculating weighting factors to model the differences in electric field strength in the TWT, affecting the coupling of the wave to the beam, and novel method for the computation the space charge forces experienced by the electron beam, using a variable plasma frequency reduction factor. The space charge method calculated a different plasma frequency reduction factor for each charge group, dependent on the angular position of the charge group about the beam axis.

DCW tubes were also designed, using the commercial software CST-MWS. A comparison was performed, comparing lateral pillar tapering and height pillar tapering. This was performed using a simulated 346 GHz BWO. DCW TWTS were designed at frequencies of 270 GHz and 92-95 GHz, and BWO was designed at 100 GHz. The dispersion characteristic and interaction impedance were calculated, as well as the S-parameters of the coupler designed for each

structure. A comparison was also investigated in the design process of the 92-95 GHz DCW TWT. Triangular pillars were compared with the square pillars, and a bend taper was designed, exploring difference in performance when a shaped pillar is utilised to allow for the passage of the electron beam.

Future work to continue the research described in the thesis would be extend the Lagrangian model to a 3D model, and to perform PIC simulations for the TWTs and BWOs designed.

4.2 Summary of Findings

In the following, the main findings of the studies will be restated.

4.2.1 Modified Lagrangian Model

The modified Lagrangian model was validated using a full 3D PIC simulation performed by CST-PS. The tube used is a simulated Ka-band DCW TWT, with central frequency 34 GHz. The output power and saturation point were compared across the bandwidth of interest. A workstation with 3.50 GHz processor speed and 16.0 GB of RAM was used. The simulation used 31 charge groups, each with 100 sub charge groups.

The saturation point was accurately modelled for the middle and upper part of the bandwidth, at between 20-25 cm. The maximum power output is modelled to be 15-25 Watts, which is consistent with the full 3D PIC simulator CST-PS. However, in the lower part and the very upper part of the bandwidth, the code does not very accurately describe the interaction when compared to the PIC simulator. However, the lower frequencies and very edge of the upper

frequencies show little interaction until 30 cm of interaction length, where the output power becomes very large. This is not consistent with the PIC code.

The simulation time for a single frequency using the modified code is about 1800s. This is much faster than the fully 3D simulator. On the same machine a full PIC simulation would take 5-10 hours.

4.2.2 DCW for millimetre wave TWTs

Two coupler configurations for a 346 GHz DCW BWO were compared. Height tapering and lateral tapering configurations were considered, and it has been shown that both are capable of performing well in terms of S_{11} and S_{21} S-parameters. Both achieved S_{11} better than -15 dB over a 30 GHz range of frequencies, and S_{21} better than -5 dB over the same range.

The BWO operating at 100 GHz described has an adequate interaction impedance, at 0.4 Ω, and the synchronous beam voltage was 10.85 kV, which is low. The lateral tapering configuration considered in the design of the coupler achieved S_{11} better than -15 dB over a bandwidth of 7 GHz, from 100 GHz to 107 GHz, and S_{21} better than -3 dB over the same range.

The TWT operating at central frequency 270 GHz described has an interaction impedance which was low, at 0.15 Ω, and a synchronous beam voltage of 13.7 kV, which is low. The lateral tapering configuration was considered achieved S_{11} better than -15 dB over a bandwidth of 10 GHz, from 267 GHz to 277 GHz, and S_{21} better than -5 dB over the same range.

The W-band TWT with the square pillars achieved a good interaction impedance of over 1 Ω. The synchronous beam voltage was 10.1 kV. The triangular pillars achieved a very good interaction impedance of 2 Ω. The

synchronous beam voltage was 10.5 GHz. The bandwidth achieved for both designs was about 10 GHz.

The square pillar design was used in the design of the tapering. Height tapering was used for the purpose, and straight tapering and bend tapering was compared. In the bend tapering design, a pillar must be shaped to allow space for the electron beam. The bend tapers with and without a shaped pillar were compared. The straight tapering achieved S_{11} better than -15 dB over almost all the band. The S_{21} is better than -3 dB over all the band. The bend taper with no pillar shaping and with pillar shaping were almost identical, with the shaped pillar configuration having slightly better S-parameters. The S_{11} is better than -15 dB over 10 GHz bandwidth, and the S_{21} is better than -3 dB over the entire band.

4.3 Successes and Limitations

The following outlines the success and limitations of the research, and attempts to explain the limitations of the work.

4.3.1 Modified Lagrangian Code

The modified Lagrangian code accurately modelled the power output and saturation point of the Ka-band DCW in the middle and upper part of the frequency band. However, it somewhat failed in the lower part of the band, and at the very edge of the upper part of the band. The difficulty to accurately describe the lower band is attributed to the difference in wave phase velocity and electron velocity. The difference between the two in the lower half of the band becomes too great.

The extreme upper band also had little interaction in the first 30 cm of interaction length, and then a very large amount of power, of about 10^4 Watts, was transferred from electron beam to wave. This may be due to the large interaction impedance at the edge of the band, and the beam being much faster than the signal in this range.

To overcome this, it may be necessary to rederive the equations in a higher dimension, to capture some of the gain which may be missing due to limitations in this model. This could include angular motion and radial motion of the sub charge groups. In terms of the gain being too much, this will capture earlier interactions, limiting the gain to more realistic levels.

Further, after the saturation points, the energy of the signal decreases. However, after a short distance of a few centimetres, the energy of the wave grows again. This may be attributed to secondary bunching, where, after energy has transferred back to the electron beam, energy is then transferred again to the wave.

4.3.2 DCW for millimetre wave TWTs

Much of the design constraints on the DCW are derived from the beam properties and the method of fabrication. In the eigenmode simulations for the SWS, the interaction impedance is greatly influenced by the gap between the pillars. However, the gap size is constrained by the electron beam width. Better interaction impedance could be achieved with a narrower beam, but may come at the cost of lower beam current, affecting gain.

For the coupler designs, the main constraints were, along with attempting to make the coupler as short as possible to limit the volume of the device, the gap between the wall and the pillar, and the minimum height of a pillar.

In terms of the approach to machining the design, the main concern is the diameter of the tooling used. If it is too wide, a small gap will not be realisable as the tapering pillars approach the wall. This results in needing a modified pillar extended in to the wall of the pillar.

When considering the LIGA process, it would be only possible to create pillars of equal height. This means for the W-band TWT, fabrication is limited to machining.

4.4 Future Work

Following are suggestions for future research opportunities using the presented work and results.

4.4.1 Lagrangian Model Extension

Extending the Lagrangian model to three dimensions would involve including radial space charge oscillations of the electron beam. This would mean the electronic charge groups would also by allowed to change their radial position. Also, the charge groups would be allowed to rotate around the beam axis. This would also mean that the weighting functions for each charge group would be dynamic. Further, models could be derived for the coupler and the beam wave interaction before the SWS is fully introduced. This would capture losses before the interaction, and any amount of beam modulation before the main interaction occurs.

4.4.2 Coupler design and PIC Simulations

Future work involving the DCW design would include the PIC simulations of the designed DCW TWT and BWOs, to find the potential gain and bandwidth of the devices and the optimum device length. Fabrication and practical tests and comparison with simulation should also be performed.

In terms of design, more investigation into the effects of shaping pillars should be performed. This includes shaping the pillar in the bend taper to allow space for the electron beam, and extending pillars in to the wall of the structure during lateral tapering.

Furthermore, as fabrication techniques become more sophisticated, the DCW SWSs performance as in an TWT or BWO could be analysed in the THz regime.

Chapter 5 Bibliography

[1] P. H. Seigel, “Terahertz Technology,” *IEEE TRans. Microw. Theory Techn.,* vol. 50, no. 3, pp. 910-928, March 2002.

[2] M. Tonouchi, “Cutting Edge Terahertz Technology,” *Nature Photon,* vol. 1, no. 1, pp. 97-105, December 2007.

[3] J. Copeland and A. A. Haeff, “The True History of the Traveling Wave Tube,” *IEEE Spectrum,* pp. 38-43, September 205.

[4] cisco, “https://www.cisco.com/c/en/us/solutions/collateral/service-provider/visual-networking-index-vni/complete-white-paperc11-481360.html,” 2017. [Online]. Available: https://www.cisco.com/c/en/us/solutions/collateral/service-provider/visual-networking-index-vni/complete-white-paperc11-481360.html.

[5] J. Wells, “Faster than fiber: The future of multi-G/s wireless,” *Microwave Magazine,* vol. 10, no. 3, pp. 104-112, 2006.

[6] J. Takeuchi, A. Hirata, H. Takahashi and N. Kukutsu, “10-Gbit/s Bi-directional wireless data transmission system using 120-GHz-band orthomode transducers,” in *2012 IEEE Radio and Wireless Symposium*, 2012.

[7] C. Paoloni, F. André, S. Kohler, V. Krozer, Q. T. Le, R. Letizia, A. Sabaawi, G. Ulisse and R. Zimmerman, “A Traveling Wave Tube for 92 – 95 GHz band wireless applications,” in *IRMMW-THZ*, Copenhagen, 2016.

[8] F. Magne, A. Ramirez and C. Paoloni, “Millimeter wave point to multipoint for affordable high capacity backhaul of dense cell networks,” in *IEEE Wireless Communications and Networking Conference*, Barcelona, Spain, 2018.

[9] C. Paoloni, F. Magne, F. André, X. Begaud, V. Krozer, M. Marilier, A. Ramírez, J. R. Ruiz, R. Vilar and R. Zimmerman, “TWEETHER Futrue Generations W-band BAckhaul and Access Network Technology,” in *EuCNC*, Oulu, Finland, 2017.

[10] C. Paoloni, “Novel high capacity millimeter wave wireless networks enabled by traveling wave tubes,” *SIMULIA Community News,* May 2018.

[11] C. Paoloni, “Novel High Capacity Millimetre Wave Wireless Networks Enabled by Traveling Wave Tubes,” in *CST European User Conference* , Unterschleissheim, Germany, 2018.

[12] D. S. Komm, R. T. Benton, H. C. Limburg, W. L. Menninger and X. Zhai, “Advances in Space TWT Efficiencies,” *IEEE Transactions on Electron Devices,* vol. 48, no. 1, pp. 174-176, January 2001.

[13] A. Jebril, M. Lucente, Ruggieri and T. Rossi, “WAVE—A new satellite mission in W-band,” in *Proc. IEEE Aerop. Conf.* , 2005.

[14] E. De Sanctis, T. Cianca, T. Rossi, C. Sacchi, L. Mucchi and R. Prasad, “Waveform design solutions for EHF broadband satellite communications,” *IEEE Commun. Mag.,* vol. 53, no. 3, pp. 18-23, March 2015.

[15] P. A. N. Ayllon, M. Ludwig and R. Dionisio, “An overview of European spaceborne vacuum tube amplifiers and system needs,” in *Proc. Ieee 18th Int. Vac. Elctron. Conf.*, 2017.

[16] G. Zhao, M. Morse, T. Wenckebach and P. Planken, “Terahertz dielectric properties of polystyrene,” *J. OPt. Soc. Am,* vol. 19, no. 6, pp. 1476-1479, 2002.

[17] T. S. Hartwick, D. T. Hodges, D. H. Barker and F. B. Foote, “Far infrared imagery,” *Applied Optics,* vol. 15, no. 8, pp. 1919-192, 1976.

[18] F. Ospald et al, “Aeronautics composite material inspection with a terahertz time-domain spectroscopy system,” *Optical Engineering,* 16 December 2013.

[19] A. Dobroiu, M. Yamashita, Y. N. Ohshima, Y. Morita, C. Otani and K. Kawase, “Terahertz Imaging system based on a bacward-wave oscillator,” *Applied Optics,* vol. 43, no. 30, pp. 5637-5646, 2004.

[20] C. Paoloni, D. Gamzina, L. Himes, B. Popovic, R. Barchfeld, L. Yue, Y. Zheng, X. . Tang, Y. Tang, P. Pan, H. Li, R. Letizia, M. Mineo, J. Feng and N. C Luhmann Jr, “THz Backward-Wave Oscillators for Plasma Diagnostics in Nuclear Fusion,” *IEEE Transactions on Plama Science,* vol. 44, no. 4, pp. 369-376, April 2016.

[21] S. E. Tsimring, Electron Beams and Microwave Vacuum Electronics, John Wiley and Sons, Inc, 2006.

[22] D. Lioubtchenko, S. Tretyakov and S. Dudorov, Millimeter wave Waveguides, London: Kluwer Academic Publishers, 2003.

[23] C. Paoloni and M. Mineo, “Double corrugated waveguide for G-band traveling wave tubes,” *IEEE Transactions on Electron Devices,* vol. 61, no. 12, pp. 4259-4263, 2014.

[24] R. N. Simons and E. G. Wintucky, “Traveling-Wave Tube Amplifi er Second Harmonic,” in *International Symposium on Antennas and Propagation and USNC/URSI National Radio Science Meeting*, Memphis, Tennessee, 2014.

[25] J. R. Pierce, “Equation for traveling-wave tubes,” *The Bell System Technical Journal,* vol. 29, no. 3, pp. 390 - 460, 1950.

[26] C. Paoloni, A. Di Carlo, F. Brunetti, M. Mineo, G. Ulisse, A. Durand, V. Krozer, K. M, A. M. Fiorella, M. Dispenza, S. A, V. Zhurbenko, F. Bouamrane, T. Bouvet, S. Megtert, E. Tamburri, C. Cojacaru and H. Gohier, “Design and Fabrication of a 1 THz Backward Wave Amplifier,” *Terahertz Science and Technology,* vol. 4, no. 4, pp. 149-162, 2011.

[27] H. R. Johnson, “Backward-Wave Oscillators,” *Proceedings of the IRE,* vol. 43, no. 6, pp. 684-697, 1955.

[28] G. Kent, “Generalized brillouin flow,” *Transactions of the American Institute of Electrical Engineers, Part I: Communication and Electronics,* vol. 79, no. 2, pp. 144-148, 1960.

[29] E. Britannica, “Encyclopædia Britannica,” Encyclopædia Britannica, 2010. [Online]. Available: https://www.britannica.com/technology/traveling-wave-tube/media/1/603591/138. [Accessed 28 July 2019].

[30] A. S. Gilmour, Klystrons, Traveling Wave Tubes, Magnetrons, Crossed-Field Amplifiers and Gyrotrons, Artech HOuse, 2011.

[31] C. K. BIrdsall and A. B. Langdon, Plasma physics via computer simulation, Newyork, London: Taylor and Francis Group, 1985.

[32] D. Gamzina et al, “Nano-CNC machining of sub-THz vacuum electron devices,” *IEEE Trans. Electron Devices,* vol. 63, no. 10, pp. 4067-4073, October 2016.

[33] D. Gamzina et al, “Nanoscale surface roughness effects on THz vacuum electron device performance.,” *IEEE Trans. Nanotechnology,* vol. 15, no. 1, pp. 85-93, 2016.

[34] S. A. M. Abadi and C. Paoloni, “UV-LIGA microfabrication process for sub-terahertz waveguides utilizing multiple layered SU-8 photoresist,” *Journal of Micromechanics and Microengineering,* vol. 26, no. 9, p. 8, 2016.

[35] S. Ahmed, V. Doychinov, S. Mathisen, D. P. Steenson, R. Letizia and C. Paoloni, “UV-LIGA microfabrication of 0.3 THz double corrugated waveguide,” *Journel of Micromechanics and Microengineering,* vol. 26, no. 9.

[36] J. H. Brooske et al, “Vacuum electronic high power terahertz sources,” *IEEE Trans. THz Sci. Technol.,* vol. 1, no. 1, pp. 54-75, September 2011.

[37] Y. H. Na, S. W. Chung and J. J. Choi, “Analysis of a broadband Q band folded waveguide traveling-wave tube,” *IEEE Transcations on Plasma Science,* vol. 30, no. 3, pp. 1017-1023, 2002.

[38] J. H. Booske et al, “Accurate parametric modeling of folded waveguide circuits for millimeter-wave traveling wave tubes,” *IEEE Electron Devices,* vol. 52, no. 5, pp. 685-694, 2005.

[39] S. Bhattacharjee et al, “Folded waveguide traveling-wave tube sources for terahertz radiation,” *IEEE Transactions on Plasma Science,* vol. 32, no. 3, pp. 1002-1014, 2004.

[40] M. Liao et al, “A Rectangular Groove-Loaded Folded Waveguide for Millimeter-Wave Traveling-Wave Tubes,” *IEEE Transactions on Plasma Science,* vol. 38, no. 7, pp. 1574-1578, 2010.

[41] M.-L. Liao and e. al, “Design of a Novel Folded Waveguide for 60 GHz Traveling Wave Tubes,” *Chin. Phys. Lett.,* vol. 33, no. 4, 2016.

[42] “TWEETHER.eu/technology,” TWEETHER, 2015. [Online]. Available: https://tweether.eu/sites/default/files/images/technology/Longitudinal-Section-%28one%20half%29-of-folded-waveguide.png. [Accessed 2019].

[43] www.flann.com, “flann.com,” Flann, [Online]. Available: https://flann.com/wp-content/uploads/2015/09/Waveguide-and-Flange-Information.pdf. [Accessed 2017].

[44] M. Mineo and C. Paoloni, “Double-Corrugated Rectangular Waveguide Slow-Wave Structure for Terahertz Vacuum Devices,” *IEEE Transactions on Electron Devices,* vol. 57, no. 11, pp. 3169-3175, 2010.

[45] C. Paoloni et al, “Design and realization aspects of 1-THz cascade backward wave amplifier based on double corrugated waveguide,” *IEEE Transactions on Electron Devices,* vol. 60, no. 3, pp. 1236-1243, 2013.

[46] C. Paoloni and M. Mineo, “0.22 THz TWT based on the doule corrugated waveguide,” in *IEEE International Transactions on Electron Devices*, Piscataway, 2014.

[47] J. F. David, A. Durand, M. Mineo and C. Paoloni, “Design of a terahertz cascade backward wave oscillator,” *IEEE ITransactions on Electron Devices,* vol. 61, no. 6, pp. 1715-1720, 2014.

[48] J. E. Rowe, “A Large Signal Analysis of the Traveling Wave Amplifier: Theory and General Results,” *IRE Transactions on Electron Devices,* vol. 3, no. 1, pp. 39-56, 1955.

[49] H. D. Arnett and L. M. WInslow, “Computer Aided TWT design,” in *1973 International Electron Devices Meeting*, Washington, D.C., 1973.

[50] J. E. Rowe, Nonlinear Electron-wave Interaction Phenomena, New York: Academic Press, 1965.

[51] D. Chernin et al, “Validation Studies for CHRISTINE-CC Using a Ka-Band Coupled-Cavity TWT,” in *: 2006 IEEE InternationVacuum Electronics Conference held Jointly with 2006 IEEE International Vacuum Electron Sources*, Monterey, 2006.

[52] A. N. Vlasov et al, “Modeling of coupled cavity TWT with TESLA,” in *2009 IEEE International Vacuum Electronics Conference*, Rome, 2009.

[53] A. N. Vlasov, T. M. Antonsen, I. A. Chernyavskiy, D. Chernin and B. Levush, "A Computationally efficient Two-Dimensional Model for the Beam-Wave Interaction in a coupled-cavity TWT," *IEEE Transactions on Plasma Science,* vol. 40, pp. 1575-1589, 2012.

[54] M. Sumathy, K. J. VInoy and S. K. Datta, "A simple equivalent circuit analysis of rectangular folded-waveguide slow-wave structure," *International Journel of Electron Communications,* 2009.

[55] C. C. Motta, "A Large Signal Analysis of a Ring Bar TWT," in *2007 IEEE 34th International Conference on Plasma Science (ICOPS)*, Albuquerque, 2007.

[56] C. Paoloni, J. David, A. Durand and M. Mineo, "Fast design method for THz backward wave amplifiers.," in *European/UK-China Workshop on Millimeter Waves and Terahertz Technologies*, Chengdu, 2014.

[57] G. M. Branch and T. G. Mihran, "Plasma Frequency Reduction Factor in Electron Beams," *IRE Transactions - Electron Devices,* vol. 2, no. 2, pp. 3-11, 1955.

[58] S. K. Datta and L. Kumar, "Plasma Frequency Reduction Factor," *Defense Science Journel,* vol. 58, no. 6, pp. 768-770, 2008.

[59] CST, *CST STUDIO SUITE,* Darmstadt, Germany [ONLINE]. Available: https://www.cst.com.

[60] N. Marcuvitz, "On Field Represenations in Terms of Leaky Modes or Eigenmodes," *IRE Transactions on Antennas and Propagation ,* vol. 4, no. 3, pp. 192-194, 1956.

[61] CST, "https://www.cst.com/solutions/solvers#," CST, 01 02 2019. [Online]. Available: https://www.cst.com/solutions/solvers#. [Accessed 2014-2019].

[62] E. Ferretti, The Cell Method: A Purely Algebraic Computational Method in Physics and Engineering, New York: Momentum Press, 2014.

[63] D. Davidson, Computational Electromagnetics for RF and Microwave Engineering, Cambridge: University Press, 2010.

[64] D. Chernin, T. Antonsen, B. Levush and D. Whaley, "CHRISTINE 3D: A 3D Multi-Frequency Large Signal Simulation Code for Helix Travelng Wave Tubes," in *Internation Vacuum LEectronics Conference 2000*, Monterey, 2000.

[65] C. Paoloni, M. Mineo, M. Henry and P. G. Huggard, "Double Corrugated Waveguide for Ka-Band Traveling Wave Tube," *IEEE TRANSACTIONS ON ELECTRON DEVICES,* vol. 62, no. 11, pp. 3851-3856, 2015.

[66] Mathworks, *MATLAB,* [Online] Available:https://uk.mathworks.com/products/matlab.

[67] K. E. Atkinson, An Introduction to Numerical Analysis, Joh Wiley & Sons, 1989.

[68] C. Paoloni and M. Mineo, "0.22 THz TWT based on the double corrugated waveguide," in *15th IEEE International Vacuum Electronic Conference*, Piscataway, N.J., 2014.

[69] C. Paoloni, F. Magne, F. Andre, X. Begaud, V. Krozer, Marilier, A. Ramirez, J. R. Ruiz, R. Vilar and R. Zimmerman, "TWEETHER Future Generation W-band Backhaul and Access Network Technology," in *26th European Conference on Networks and Communications (EuCNC 2017)*, Oulu, 2017.

[70] M. Mineo and C. Paoloni, "Improvement of cold parameters of the double corrugated waveguide by geometrical shaping of the corrugations," in *14th IEEE International Vacuum Electronics Conference*, Paris, 2013.

[71] C. K. Chong and W. L. Menniger, "Latest Advancements in high power millimeter wave helic TWTs," *IEEE Trans. Plasma Sci.,* vol. 138, no. 6, pp. 1227-1238, 2010.

[72] T. Hartwick, "Far infrared imaging techniques for law enforcement applications," *SPIE Opt. Secur. Law Enforcement,* 1977.

[73] R. Waring and C. Paoloni, “Lagrangian simulator for Millimetre Wave TWT Based on Non-rotationally Symmetric Slow-Wave Structure,” *Journal of Electromagnetic Waves and Applications,* vol. 31, no. 17, pp. 1902-1923, 2017.

[74] R. Waring and C. Paoloni, “Lagrangian Large Signal Model for Double,” in *UK/Europe-China Workshop on Millimetre-Waves and Terahertz Technologies*, Liverpool, UK, 2017.

[75] C. Paoloni, D. Gamzina, B. Popovic, L. Himes, R. Barchfield, R. Letizia, Y. Tang, H. Li, R. Waring, J. Zhang, P. Pan, J. Feng and Luhmann, “Double corrugated wavguide 0.346 THz BWO with wide beam channel,” in *UK-Europe-China Workshop on mm-waves and THz Technologies*, Qingdao, China, 2016.

Chapter 6 APPENDIX A: Code

Main

```
function [power] = main(~)
profile on;
global  uy phi dz  u0 C njt  d  j omega  V0 I0 Z0  L  omegap bprime
global eta c period F_axial_w beta
global A dthy thy dA  nrt F F2 FSP I  b1
global numnstep nat  CZ

 format long

c=2.997925*10^8;                %speed of light
njt =31;                        %total number of charge groups
nrt=10;                         %total number of concentric rings
nat=10;                         %total number of segments
eta = 1.758820024*10^11;                %charge mass ratio of electron
epsilon = 8.85418782*10^(-12);
eg= eta/(c^2);

%Input parameters
Numberofsteps=1000;
V0=108800;                      %Voltage
I0=0.2;                         %Beam current
```

```
Z0=0.9;                    %Interaction Impedance
fr = 34e9;
power=20;                  %Power in dBm
L=0.25;                    %LEngth of tube in meters
dz=L/Numberofsteps;        %integration Step
bprime=250e-6;             %Beam radius
period=2.21e-3;            %periodicity of the DCW
beta=3452.5706141711;      %propagtion constant
a=1500e-6;                 %average radius
alpha=0.017927;            %attenuation
 ldbperm = alpha/period;
 ldbl=ldbperm*lambda
 bessj0 = inline('besselj(0,x)');
q=20;
for q1 = 1:q
    mul(q1) = fzero(bessj0,[(q1-1) q1]*pi);
    %Calculates first n roots of the bessel function J
end


uy(1:njt,1:nrt,1:nat)    =     0;


phi(1:njt,1:nrt,1:nat)   =     0;


gamma = eta/(c^2)*V0+1
```

```
u0=sqrt((2*eta*V0))

omega          =       fr*2*pi



pfrf(1:nrt,1)=0.652;

pfrf(1:nrt,2)=0.492;

pfrf(1:nrt,3)=0.471;

pfrf(1:nrt,4)=0.471;

pfrf(1:nrt,5)=0.492;        %effective radii

pfrf(1:nrt,6)=0.652;

pfrf(1:nrt,7)=0.472;

pfrf(1:nrt,8)=0.472;

pfrf(1:nrt,9)=0.472;

pfrf(1:nrt,10)=0.472;



for nn=1:nrt

   for nnn=1:nat

omegap(nn,nnn)   =  pfrf(nn,nnn)*sqrt(eta*I0/(pi*epsilon*bprime*bprime*u0));

   end  %plasma frequency

end

v0phase            =     omega/beta; %phase velocity
```

```
C               =       (I0*Z0/(4*V0))^(1/3); %Gain parameter

b1 =  (u0-v0phase)/(C*v0phase)  %synchronicity parameter


pw              =   10^(power/10)/1000; %power in watts

for n11=1:nat
for n1=1:nrt
for i2          =   1:njt

   j          =   i2-1;

   phi(i2,n1,n11) = (2*pi*(i2-1))/(njt); %initial phase for charge groups

   uy(i2,n1,n11)  =   0; %initial velocities

end
end
end
%Ring Weighting function%
rprop=1/sqrt(2);
r1=bprime/2;
```

```
% for n10 = 1:nrt
% rprime = sqrt(n10)*r1
fileID = fopen('34GHz.txt','r');
formatSpec = '%f %f';
sizeF = [10 10];
F = fscanf(fileID,formatSpec,sizeF)
fclose(fileID);

fileID = fopen('on_axis_wf.txt','r');
formatSpec1 = '%g';
sizeF2 = [72 1];
F2 = fscanf(fileID,formatSpec1,sizeF2)
fclose(fileID);

fileID = fopen('34_axial_impedances_cut.txt','r');
formatSpec2 = '%g';
sizeF3 = [7 1];
F3 = fscanf(fileID,formatSpec2,sizeF3)
fclose(fileID);

fileID=fopen('weight_axial_34.2.txt','r');
formatSpec='%g';
sizeFW=[2208,1];
F_axial_w = (fscanf(fileID,formatSpec, sizeFW));
fclose(fileID);
```

```
 for pos=1:sizeF3
    CZ(pos)=(I0*F3(pos)/(4*V0))^(1/3) ;
 end


numnstep=1;
for nat1=1:nat
end
disp(mul(1))
FSP(1:njt,1:nrt,1:njt)=0;
FSP2(1:njt,1:nrt)=0;
% Space Charge Weighting Function%

for nn = 1:nrt

    for j1 = 1:njt
        O=1;
        SIGN1(j1)=0;
        ABS1(j1)=0;
        for f1 = 1:njt
%
                 FSPa(1:q)=0;
                Phi_diff= phi(f1,nn,nn)-phi(j1,nn,nn);
                SIGN(f1,j1)=sign(Phi_diff);
```

```
            ABS(f1,j1)=abs(Phi_diff);
          for l=1:q

   LL(l)=(((besselj(1,mul(l)*(bprime/a)))/(mul(l)*besselj(1,mul(l))))^2);

   FSPa(l)=1*exp(((-
1*mul(l)*u0)/(a*omega))*ABS(f1,j1))*LL(l)*SIGN(f1,j1)*u0/(omega*bprime);

   FSP(j1,nn,O) = FSP2(j1,nn)+FSPa(l);

          end
          O=O+1;
          SIGN1(j1)=SIGN1(j1)+SIGN(f1,j1);
          ABS1(j1)=ABS1(j1)+ABS(f1,j1)*SIGN(j1);

       end

        nhytebheb=1;
   end
   nhytebheb=1;
end

d=ldbl*0.01836/C ;

for k        =   1
```

```
   A(k)       =   sqrt(pw/(2*I0*V0*C)) %normalised rf power/voltage
 dthy(k)      =  -b1;                  %initial rate of change of phase
  dA(k)       =  -d*A(k)*(1+C*b1); %initial rate of change of rf wave amplitude


  thy(k)      =   0; %phase between rf and cold rf
end


 rungekuttause1();


end


end
profile viewer;
end
```

Initialisation

```
function [zpos]=rungekuttause1(~)


global  njt   nrt  u0 omega   Power nat
global  omegap  c1 c2
global b1 C phi uy F d
global  X1  I0 V0
global     nstep dy
global A dthy thy dA
iii=1;


pq=1;
b=b1;
number=1;
n222=0;
for n22 = 1:nat
   for n2 = 1:nrt
         for i2  =   1:njt
         phi1(i2+njt*(n2+n22+n222)-2*njt)    =   phi(i2,n2,n22);
         uy1(i2+njt*(n2+n22+n222)-2*njt)     =   uy(i2,n2,n22);
      end
   end
   n222=n222+nat-1;;
end
phi1    =   transpose(phi1);
```

```
uy1     =   transpose(uy1);
 thyhfuierhfu=1;

X0      =   [dA;A;dthy;thy;uy1;phi1];
circuit=1;
[Y,X1]  =   rk4(@f,0,dy*nstep,X0,nstep);

for     i5          =   1:nstep

        X1(i5,2);

        Power(i5)   =   2*C*I0*V0*(X1(i5,2)*X1(i5,2))*(1-C*X1(i5,3))/(1+C*b) ;

        powerL(i5)  =   10*log10(Power(i5)*1000);

        gain(i5)    =   20*log10(X1(i5,2)/X1(1,2));

end


 = 299792458;

for i=1:1001
zpostion(i)=Y(i)*u0/omega/C;
end
```

```
gh=1;
function dXdY = f(Y,X)
zpos(number)=Y*u0/omega/C;

        dXdY = zeros(1,4+2*njt*nrt*nat);       %creates array for dX/dY

        [c1,c2]=circuiteqn(1); %outputs circuit equation integral calculation

        n444=0;
         for n44=1:nat;
            for n4=1:nrt;
               for     i7=1:njt

                  uy(i7,n4,n44)=X(4+i7+n444*njt);

                  phi(i7,n4,n44)=X(4+i7+nrt*nat*njt+n444*njt);

               end
               n444=n444+1;
            end

         end
          n444=0;
         for n4 = 1:nrt
            for n44=1:nat
```

```
                    for    i9=1:njt

                dXdY(4+i9+njt*nrt*nat+(n444)*njt)=-X(3)+(1/C)*(1-
1/(1+2*C*uy(i9,n4,n44)));
                %dphi/dy, solves for phi of each charge group

                    end
                    n444=n444+1;
               end
%                n444=n444+1;
            end
            n555=0;
           for n5=1:nrt;
              for n55=1:nat
                 for     m11=1:njt
                 se=se1(m11,n5,n55);%space charge acting on charge group
                 phi0= phi(m11,n5,n55);
                 sin1=-X(2)*(1-X(3)*C)*sin(phi0)+C*X(1)*cos(phi0);

                 asin1 = F(n5,n55)*sin1;

SPC=(1/(1+C*b))*((omegap(n5,n55)/(omega*C))^2)*se/(1+2*C*uy(m11,n5,n5
5));

dXdY(4+m11+njt*n555)=1*((asin1)/(1+2*C*uy(m11,n5,n55)))+SPC;
```

```
            %solves for du/dy for u for each charge group


            end
            n555=n555+1;
          end

        end
        hmmm=12;
        dXdY(1)=-(1+C*b/(pi*C))*c2+X(2)*(((1/C-X(3))^2)-((1+C*b)/C)^2);
        %d2A/dy2, solving for da/dy

        dXdY(2)=X(1);
        %dA(y)/dy solving for A(y)

        dXdY(3)=(-(1+C*b)/(pi*C)*c1-(2*X(1)*(X(3)-
1/C))/X(2))+(2*d/C)*((1+C*b))^2 ;
        %d2theta(y)/dy2

        dXdY(4)=X(3);
        %dtheta(Y)/dy

        dXdY=transpose(dXdY);

end
    number=number+1
```

```
end
```

Circuit Equation solver

```
function [d2tdy2, d2Ady2] = circuiteqn(k)
  global C uy d phi njt nrt F numnstep nat  F2  dz  second_phase
  global period weight_test F_axial_w J2 MJ beta



  n33=1;
     h   =   2*pi/(njt-1);


J2(:,:)=0;
for n31 = 1:nrt
    for n32 =1:nat
        cos1=0;cos2=0;cos3=0;cos4=0;
        sin1=0;sin2=0;sin3=0;sin4=0;


        J2=1;


        phi1    =   phi(1,n31,n32);



            CZ2=(((phi(1,5,5)/(2*pi))*(2*pi/(beta*period)*period) +(numnstep-
1)*dz/4));


                second_phase(numnstep,1)=mod(CZ2,period);
```

```
weight_test(numnstep,1)=round((second_phase(numnstep,1)/period)*2207)+
1;

                    pos=weight_test(numnstep,1);

                      J3(1)=F_axial_w(pos);

                        uy1    =   uy(1,n31,n32);
                        cos1   =   J2*cos(phi1)/(1+2*C*uy1);
                        sin1   =   J2*sin(phi1)/(1+2*C*uy1);

for    k2     =   2:2:njt-1

      J2(k2)=1;

      phi2   =   phi(k2,n31,n32);


         CZ2=(((phi(k2,5,5)/(2*pi))*(2*pi/(beta*period)*period)+(numnstep-
1)*dz/4));

            second_phase(numnstep,k2)=mod(CZ2,period);
```

```
weight_test(numnstep,k2)=round((second_phase(numnstep,k2)/period)*2207)
+1;

                pos=weight_test(numnstep,k2);

                  J3(k2)=F_axial_w(pos);

                       uy2    =   uy(k2,n31,n32);
                       cos2   =   J2(k2)*cos2+cos(phi2)/(1+2*C*uy2);
                       sin2   =   J2(k2)*sin2+sin(phi2)/(1+2*C*uy2);

end

for    k2     =   3:2:njt-2

      J2(k2)=1;

      phi3   =   phi(k2,n31,n32);


        CZ2=(((phi(k2,5,5)/(2*pi))*(2*pi/(beta*period)*period)+(numnstep-
1)*dz/4));

           second_phase(numnstep,k2)=mod(CZ2,period);
```

```
weight_test(numnstep,k2)=round((second_phase(numnstep,k2)/period)*2207)
+1 ;

                pos=weight_test(numnstep,k2);

                  J3(k2)=F_axial_w(pos);

                    uy3    =   uy(k2,n31,n32);
                    cos3   =   J2(k2)*cos3+cos(phi3)/(1+2*C*uy3);
                    sin3   =   J2(k2)*sin3+sin(phi3)/(1+2*C*uy3);
end



    J2(njt)=1;

    phi4   =   phi(njt,n31,n32);

       CZ2=(((phi(njt,5,5)/(2*pi))*(2*pi/(beta*period)*period)+(numnstep-
1)*dz/4));

          second_phase(numnstep,njt)=mod(CZ2,period);
```

```
weight_test(numnstep,njt)=round((second_phase(numnstep,njt)/period)*2207)
+1;

                pos=weight_test(numnstep,njt);

                  J3(njt)=F_axial_w(pos);

                  uy4    =   uy(njt,n31,n32);
                  cos4    =   J2(njt)*cos(phi4)/(1+2*C*uy4);
                  sin4    =   J2(njt)*sin(phi4)/(1+2*C*uy4);




                    sumcostot   =   (cos1+4*cos2+2*cos3+cos4);
                    sumsintot   =  (sin1+4*sin2+2*sin3+sin4);



                      J=F(n31,n32);
                      MJ(numnstep)=mean(J3);

     d1(n33)        =  J*mean(J3)*(h/3)*(sumsintot + 2*C*d*1)/(0.9*0.9*nrt*nat)
;
```

```
        d2(n33)       =  J*mean(J3)*(h/3)*(sumcostot - 2*C*d*1)/(0.9*0.9*nrt*nat);


                                        n33=n33+1;
    end
                                        n33=nat*n31+1;
end
                d2tdy2=sum(d1);
                d2Ady2=sum(d2);



numnstep=numnstep+1;
```

Space charge solver

```
function sc = spacecharge2(m,n,p)

global C omega nrt omegap  njt uy phi u0 bprime FSP b1
phicharge group = phi(m,n,p);       %equals the reference number of the
charge group for which space charge force is being evaluated

f = 1/(1+C*b1)*(omegap(n,p)/omega/C)^2;
phicharge group = phi(m,n,p);
K=(-1*u0/omega/bprime);

si=2*pi/(njt-1)/3;

sumuy1=0;sumuy2=0;sumuy3=0;sumuy4=0;
sumphi1=0;sumphi2=0;sumphi3=0;sumphi4=0;

   uy1=uy(1,n,p);

   sumuy1=1/(1+2*C(1)*uy1);
   sumphi1=FSP(m,n,1)*exp(K*abs(phicharge group-
phi(1,n,p)))*sign(phicharge group-phi(1,n,p));

for  k2=2:2:njt-2;

   uy1=uy(k2,n,p);
```

```
    sumuy2=sumuy2+1/(1+2*C(1)*uy1);
    sumphi2=sumphi2+FSP(m,n,k2)*exp(K*abs(phicharge group-
phi(k2,n,p)))*sign(phicharge group-phi(k2,n,p));
end
for k2=3:2:njt-1;

    uy1=uy(k2,n,p);

    sumuy3=sumuy3+1/(1+2*C(1)*uy1);
    sumphi3=sumphi3+FSP(m,n,k2)*exp(K*abs(phicharge group-
phi(k2,n)))*sign(phicharge group-phi(k2,n,p));
end

    uy1=uy(njt,n,p);



sumuy4=1/(1+2*C(1)*uy1);

sumphi4=FSP(m,n,njt)*exp(K*abs(phicharge group-phi(njt,n)))*sign(phicharge
group-phi(njt,n,p));

sumuytot=(sumuy1+4*sumuy2+2*sumuy3+sumuy4);
sumphitot=(sumphi1 + 4*sumphi2+2*sumphi3+sumphi4);
sc = si*f*sumuytot*sumphitot;
```

Differential equation solver

```
function [Y,X] = rk4(fun,Y0,Yf,X0,n)
% global c1 c2
dY=(Yf-Y0)/n;
Y(1) = Y0;
X(1,:)=X0;

for k=1:n
Y(k+1) = Y0+k*dY;
Y(k)=Y0+k*dY;
k1 = feval(fun,Y(k),X(k,:));
k2 = feval(fun,Y(k)+dY/2,X(k,:) + dY/2*k1');
k3 = feval(fun,Y(k)+dY/2,X(k,:) + dY/2*k2');
k4 = feval(fun,Y(k)+dY,X(k,:) + dY*k3');
X(k+1,:)=X(k,:)+dY/6*(k1'+2*k2'+2*k3' +k4');

end
end
```

Chapter 7 APPENDIX B: S-Parameters

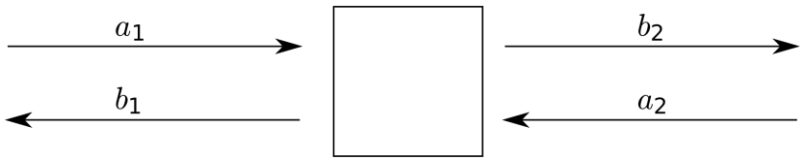

Figure B 1 Incident and reflected signals

For a 2-port system with an input port and an output port, there are 4 S-parameters. These are shown in equation B.1, scattering matrix. Consider a waveguide with two ports, 1 and 2. The schematic is shown in Figure B. 1. If a signal is stimulated at port 1, then S_{11} is the ratio of the signal reflected to port 1 and the input signal at port 1. S_{21} is the ratio of signal input at port 1 and incident on port 2. The variable a_1 is the wave incident on port 1, and a_2 is the wave incident on port 2. The variable b_1 represents the wave reflected from port 1, and similarly b_2 represents the signal reflected from port 2. The difference of these two parameters is what is lost as attenuation and electrical losses due to finite conductivity of the structure, and surface roughness increasing the distance the signal propagates through the structure. The parameters of interest are S_{11} and S_{21}, as the full TWT or BWO is symmetrical. The relationship between the **S,** and the a and b variables is shown below.

$$\mathbf{S} = \begin{pmatrix} \mathrm{S}_{11} & \mathrm{S}_{12} \\ \mathrm{S}_{21} & \mathrm{S}_{22} \end{pmatrix} \qquad \text{B.1}$$

$$\begin{pmatrix} \mathrm{b}_1 \\ \mathrm{b}_2 \end{pmatrix} = \mathbf{B} = \mathbf{S} \times \mathbf{A} = \begin{pmatrix} \mathrm{S}_{11} & \mathrm{S}_{12} \\ \mathrm{S}_{21} & \mathrm{S}_{22} \end{pmatrix} \times \begin{pmatrix} \mathrm{a}_1 \\ \mathrm{a}_2 \end{pmatrix} \qquad \text{B.2}$$

Chapter 8 List of Published Papers

1. Waring, R & Paoloni, C 2018, 'Lagrangian Large Signal Model for Double Corrugated Waveguide' Paper presented at IVEC 2018, Monterey, United States, 24/04/18 - 27/04/18,

2. Waring, R & Paoloni, C 2017, 'Lagrangian Large Signal Model for Double Corrugated Waveguides'.

3. Waring, R & Paoloni, C 2017, 'Lagrangian simulator for Millimetre Wave TWT Based on Non-rotationally Symmetric Slow-Wave Structure' Journal of Electromagnetic Waves and Applications, vol. 31, no. 17, pp. 1902-1913

4. Paoloni, C, Gamzina, D, Popovic, B, Himes, L, Barchfeld, R, Letizia, R, Tang, Y, Li, H, Waring, R, Zhang, J, Pan, P, Feng, J & Luhmann Jr., NC 2016, 'Double corrugated waveguide 0.346 THz BWO with wide beam channel' Paper presented at 41st International Conference on Infrafred, Millimeter and Terahertz Waves, Copenhagen, Denmark, 25/09/16 - 30/09/16

5. Waring, R & Paoloni, C 2015, A Fast Model of a 1-D Nonlinear Beam-Wave Interaction for a 225GHz TWT. in 8th UK-Europe-China Workshop on mm-waves and THz Technologies. IEEE, 8th European/UK-China

Workshop on Millimeter Waves and Terahertz Technologies (UCMMT 2014) , Cardiff, United Kingdom, 14/09/15